Master of Science in Space Science Technologies and Applications

National Observatory of Athens
Department of Informatics and Telecommunications-University of the Peloponnese

The impact of transient interplanetary structures on Solar Energetic Particles

Master Thesis

Myrto Koletti

Advisory Committee:

Dr. Anastasios Anastasiadis, *Research Director*

Institute for Astronomy, Astrophysics, Space Applications & Remote Sensing National Observatory of Athens

Dr. Athanasios Papaioannou, *Associate Researcher*

Institute for Astronomy, Astrophysics, Space Applications & Remote Sensing National Observatory of Athens

Dr. George Balasis, *Research Director*

Institute for Astronomy, Astrophysics, Space Applications & Remote Sensing National Observatory of Athens

Athens, September 2020

ABSTRACT

Solar energetic particles (SEP) are a significant component of space weather, due to their strong impact on terrestrial and space human activity. They constitute an important field of research and the better understanding of the physical processes that dominate them is key to the advancement of space weather forecasting tools.

The goal of this thesis is to investigate the impact of transient interplanetary structures on SEP intensities. Specifically, we focus on the effect of the specific interplanetary magnetic field (IMF) configuration determined by the position of one or more interplanetary coronal mass ejections (ICMEs) at the time of the maximum proton intensity, based on in-situ measurements. For this purpose, a catalogue of 98 western SEP events is compiled. The SEP events are classified to 6 classes, based on the location of one or more ICMEs with respect to the observer at the time of the maximum proton intensity.

Firstly, we confirm that, SEP events associated with more intense solar conditions, statistically reach higher proton intensities. Moreover, events that occur during periods that multiple ICMEs are present in the interplanetary space, are expected to reach higher intensities, as well. Generally, SEP events are most likely to be associated with one or more ICMEs. Specifically, the most common events are those that occur when the Earth is immersed within an ICME.

We also conclude that, the location of one or more ICMEs at the time of the maximum proton intensity is a significant factor affecting the observed proton intensity. More specifically, events that occur when Earth is immersed within an ICME or after an ICME has passed Earth, are statistically associated with the highest proton intensities. Specifically for events observed after a preceding ICME has passed Earth, the observed proton intensity statistically increases with the speed of the ICME. Events that occur within the standard solar wind, in the sheath region of an ICME or shortly before an ICME passes Earth, reach lower intensities.

Lastly, the magnetic configuration within an ICME is also an important factor. For given solar conditions, the proton intensity of a SEP event immersed within an ICME with a magnetic cloud (MC) configuration is expected to reach lower intensities, compared to events immersed within ICMEs without an MC configuration.

i

ΠΡΟΛΟΓΟΣ

Τα ηλιακά ενεργειακά σωματίδια (ΗΕΣ, SEPs) είναι μία σημαντική συνιστώσα του διαστημικού καιρού, λόγω της ισχυρής επίδρασης πού έχουν στην ανθρώπινη δραστηριότητα στη Γη και το διάστημα. Αποτελούν ένα σημαντικό πεδίο έρευνας και η καλύτερη κατανόηση των φυσικών διεργασιών που κυριαρχούν σε αυτά είναι βασικός παράγοντας για την ανάπτυξη εργαλείων πρόβλεψης του διαστημικού καιρού.

Ο στόχος της παρούσας διπλωματικής είναι η έρευνα της επίδρασης διαδιδόμενων σχηματισμών του διαπλανητικού μαγνητικού πεδίου στην ένταση των ΗΕΣ. Πιο συγκεκριμένα, εστιάζουμε στην επίδραση της διαμόρφωσης του διαπλανητικού μαγνητικού πεδίου, όπως καθορίζεται από την θέση ενός ή περισσότερων διαπλανητικών στεμματικών εκτινάξεων μάζας (ΔΣΕΜ, ICMEs) όταν καταγράφεται η μέγιστη ροή πρωτονίων, βασιζόμενοι σε επιτόπιες μετρήσεις. Για αυτό το σκοπό, δημιουργείται μια βάση δεδομένων αποτελούμενη από 98 γεγονότα ΗΕΣ, τα οποία προέρχονται από δυτικά ηλιογραφικά πλάτη. Τα γεγονότα ΗΕΣ ταξινομούνται σε 6 κατηγορίες, ανάλογα με την θέση ενός ή περισσότερων ΔΣΕΜ όταν καταγράφεται η μέγιστη ροή πρωτονίων.

Καταρχάς, επιβεβαιώνουμε ότι, γεγονότα ΗΕΣ τα οποία συνδέονται με ισχυρότερα φαινόμενα στον Ήλιο, στατιστικά φτάνουν υψηλότερες ροές πρωτονίων. Επιπρόσθετα, γεγονότα τα οποία συμβαίνουν σε περιόδους κατά τις οποίες πολλαπλά ΔΣΕΜ βρίσκονται στον διαπλανητικό χώρο, αναμένουμε ότι θα φτάσουν επίσης υψηλότερες ροές. Γενικά, γεγονότα ΗΕΣ είναι πιο πιθανόν να συνδέονται με ένα ή περισσότερα ΔΣΕΜ. Συγκεκριμένα, τα συνηθέστερα ΗΕΣ γεγονότα είναι εκείνα τα οποία συμβαίνουν όταν η Γη βρίσκεται εντός ενός ΔΣΕΜ.

Επίσης, καταλήγουμε ότι, η θέση ενός ή περισσότερων ΔΣΕΜ όταν καταγράφεται η μέγιστη ροή πρωτονίων είναι ένας σημαντικός παράγοντας που επηρεάζει την παρατηρούμενη ροή πρωτονίων. Πιο συγκεκριμένα, γεγονότα τα οποία συμβαίνουν ενώ η Γη βρίσκεται εντός ενός ΔΣΕΜ ή αφού ένα ΔΣΕΜ έχει περάσει από την Γη, στατιστικά συνδέονται με τις υψηλότερες ροές πρωτονίων. Πιο συγκεκριμένα για τα γεγονότα τα οποία παρατηρούνται αφού ένα προηγούμενο ΔΣΕΜ περνά από τη Γη, η παρατηρούμενη ροή πρωτονίων αυξάνεται στατιστικά με την ταχύτητα του ΔΣΕΜ. Γεγονότα τα οποία συμβαίνουν στον αδιατάρακτο ηλιακό άνεμο, στην περιοχή ανάμεσα στο προπορευόμενο κρουστικό κύμα και το ΔΣΕΜ ή λίγο πριν ένα ΔΣΕΜ περάσει τη Γη, φτάνουν χαμηλότερες ροές.

Τέλος, η διαμόρφωση του μαγνητικού πεδίου εντός του ΔΣΕΜ είναι επίσης ένας σημαντικός παράγοντας. Για δοσμένες συνθήκες στον Ήλιο, η μέγιστη ροή πρωτονίων ενός γεγονότος ΗΕΣ που συμβαίνει εντός ενός ΔΣΕΜ με διαμόρφωση μαγνητικού νέφους, αναμένεται να φτάσει χαμηλότερες ροές σε σχέση με γεγονός εντός ΔΣΕΜ χωρίς διαμόρφωση μαγνητικού νέφους.

Contents

LIST OF ABBREVIATIONS   76

LIST OF FIGURES   77

LIST OF TABLES   79

REFERENCES   80

FOREWORD

Solar Energetic Particles (SEPs) are flux enhancements of high-energy charged particles originating from the Sun. Their energies vary from 10 keV to several GeV reaching speeds up to 90% the speed of light. SEPs are dominated by electrons and protons, however other elements, from He to Pb, have also been measured [1].

SEPs are a significant component of space weather, as they can pose a significant danger to spacecrafts and aircraft, as well as a health hazard for astronauts and flight crews[2],[3]. They are an important research topic, that has received growing attention in the last decades. The study of the physical processes that dominate them can contribute to the development space weather forecasting tools and can help answer theoretical aspects of various eruptive solar phenomena.

It is widely accepted that SEPs originate at the most intense solar phenomena, as they are associated with solar flares and coronal mass ejections (CMEs). Observations indicate that these phenomena are not independent, rather parts of the same dynamic process on the Sun [4]. The overall mechanism that leads to these eruptions is not yet fully understood, however it is accepted that there is a general statistical correlation between them: the most intense flares are most likely to be associated with the fastest CMEs[5]. The most intensified SEPs are also statistically associated with the most intense solar phenomena. SEPs are also expected to propagate along the nominal Parker spiral, however transient interplanetary structures can potentially have a strong impact on the SEP profiles observed at the Earth.

This thesis is a statistical study of the impact of transient interplanetary structures on SEP intensity profiles. For this purpose, a database consisting of 98 western SEP events, associated with a solar flare and/or a CME is compiled and the events are classified to 6 main classes, depending on the position of one or more interplanetary CMEs (ICMEs) with respect to the observer, at the time of the maximum proton intensity. A secondary classification of class 3 events is also performed, concerning the magnetic topology of the associated ICME.

The introduction provides the theoretical basis of solar phenomena that drive SEPs, concerning the basic properties of the Sun (subsection 1.1) and the solar eruptions that drive particles (subsection 1.2). The characteristics of SEPs are presented in subsection 1.3. In section 2 the construction of the SEP database and the classification scheme are explained, followed by section 3, where the data are statistically analysed. In subsection 3.1 the behavior of the parameters of the coronal activity related to the origin of the SEP event is examined, namely the speed of the CME and the peak SXR flux and fluence of the associated flare. In subsection 3.2, the effect of the aforementioned solar parameters on the proton intensities is investigated, as well as of the specific IMF configuration. Lastly, the spectral profiles of the SEP events are analysed and the effect of the IMF configuration is considered, revealing its importance (subsection 3.3). The main conclusions are presented and explained in sections 4 and 5.

ACKNOWLEDGMENTS

1   INTRODUCTION

SEPs are an important component of space weather, originating at the most intense solar phenomena. These phenomena are driven by the Sun's magnetic field and are the interplay of various processes that originate at its interior. Thus, an overview of the basic characteristics of the Sun (subsection 1.1) and solar eruptions (subsection 1.2) is needed, before presenting the main characteristics of SEPs (subsection 1.3).

1.1   The Sun

Our Sun is a typical star of radius $7 \cdot 10^5$ km, mass $2 \cdot 10^{30}$ kg and an effective temperature of 5780K. It is found on the Main Sequence of the Hertzsprung–Russell diagram, its spectral type is G2V and its absolute stellar magnitude equals to 4.8. The Sun-Earth distance is referred to as the *astronomical unit* (AU): 1 AU=149597870 $\pm$2 km [6].

As every other star, the Sun is held by its own gravitational attraction and radiates energy, which is produced via the nuclear fusion of hydrogen nuclei into helium in its core. The energy produced deep inside our Star results in a total luminosity equal to $3.86 \cdot 10^{26}$ W [4]. The fusion rate is used in order to estimate the age of the Sun to approximately 4.6 billion years [4]. The Sun's age can also be estimated by radioactive dating of the oldest meteorites of the solar system [6] and in comparison with the age of the Earth and other planets.

On average, the Sun rotates on its axis once every 27 days [7]. The angle between the rotational axis and the elliptical plane is $\sim 7^o$ and the solar equatorial velocity is $\sim$2 km/s. However, the Sun does not rotate as a rigid body and its angular velocity depends on the solar latitude. The period of rotation at the equator is approximately 25 days and is increasing at higher latitudes. At solar latitudes close to the poles the rotation period is up to 35 days [1]. This phenomenon is called *differential rotation*.

The mass of the Sun determines its evolution. In about five billion years, the available hydrogen at the core will be exhausted and the nuclear fusion will continue in shells outside the core. The Sun will expand into a red giant for 250 million years. At some point helium will start to be fused into carbon and the remaining mass of the Sun will shrink and cool into a white-dwarf star of the size of Earth[4].

1.1.1   The Solar Interior

Conditions in the solar interior can be estimated mainly by determining a set of equations of physical principles combined with measurements at the solar atmosphere. The generally accepted model for the solar interior consists of the following regions:

-The **core** is the central region where nuclear reactions take place. It contains $\sim 10\%$ of the total solar mass and it extends to $\sim 25\%$ of the solar radius. The temperature at the very center of the Sun is about 15 million K and the density is about $150 g/cm^3$. The high temperature enables the energy production via nuclear fusion. In general, there are two main reaction chains for stellar fusion: the

---

[1]https://sohowww.nascom.nasa.gov/explore/lessons/diffrot9_12.html

proton-proton (p-p) cycle and the Carbon–Nitrogen–Oxygen (CNO) cycle. For the Sun, 99% of the total energy comes from the p-p chain and about 1% from the CNO [6]. The final result is:

$$4\,^1H \longrightarrow\ ^4He + 2e^+ 2\nu + 26.7MeV \tag{1.1.1}$$

According to the above equation, every second $5 \cdot 10^9$ kg H are fused into He nuclei, while a small percent, $\sim 0.7\%$, is converted into energy in the form of γ-rays (26.2 MeV) and two neutrinos ν (0.5 MeV).

-The energy produced in the core is leaked outwards across the ***radiative zone***, where it is transferred mainly by radiative diffusion. High energy photons are scattered and re-absorbed continuously, taking thousands of years to escape. This region extends from 0.25 to 0.70 of the solar radius. The temperature falls from 7 million to 2 million K and the density from 20 g/cm^3 to 0.2 g/cm^3 [4].

-The ***convection zone*** is the outer region of the solar interior, reaching the visible surface of the Sun. In this region energy transport through convection is dominant, due to the increasing outward opacity. Convention is a much faster energy transfer process than radiation, as the heated gas takes almost 10 days to climb through the solar atmosphere [6]. The temperature falls rapidly from $\sim 2 \cdot 10^6$ K to only 5700 K and the density at the top of the convection zone, just below the solar surface, is only 0.0000002 g/cm^3 [2].

-The radiative and convection zones are divided by a shear layer, called the ***interface layer*** or ***tachocline***, where it is assumed that the large scale magnetic field is produced via the dynamo process. Moreover, at this layer the rotation of the Sun abruptly changes from uniform to differential [4].

Doppler imaging shows oscillatory motions on the solar surface. The primary oscillations occur with a period of five minutes (*5-minute oscillations*) and are due to radial inward and outward spreading stationary sound waves. These waves, called p-modes, are generated due to pressure fluctuations in the convection zone. reflected between the deeper and hotter layers of the convection zone and the base of the photosphere. Therefore, these oscillations have been used to determine the properties and physical conditions in the solar condition. Other types of waves generated are gravity waves (g-modes), which are limited below the convection zone and surface gravity waves (f-modes), which spread above the convection zone [6].

1.1.2   The Solar Atmosphere

The solar atmosphere is the part where photons can escape, thus the part of the Sun that can be directly observed. It consists of three main layers: the photosphere, the chromosphere and the corona.

-The ***photosphere*** is the lowest region of the atmosphere and the part of the Sun that is seen in white light. It is only a few hundred kilometers thick and lies on top of the convection region. The photospheric temperature decreases with height, creating the *Limb Darkening* phenomenon: the intensity falls of significantly towards the limb, where the higher, cooler, thus darker, upper layers of the photosphere are observed, in contrast to the higher intensities at the center of the disk, originating from deeper and
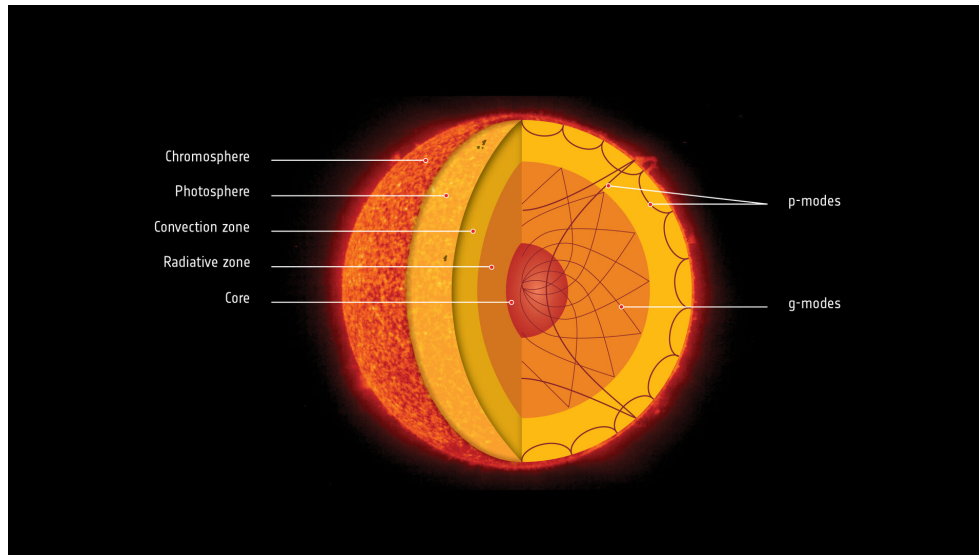
---

[2]https://solarscience.msfc.nasa.gov/interior.shtml

Figure 1.1: The solar structure. The wavelengths of p- and g-modes are also illustrated.
Credit: SOHO (ESA $\&$ NASA)

hotter photospheric levels [8].

The plasma motions originating from the convection region are visible on the surface of the pho-tosphere as *granules* and *supergranules*. The *granules* are bright areas, formed as hot plasma is rising with speed $\sim 0.5 - 1.5 km/s$ from the convection zone to the surface of the photosphere, where it flows horizontally. As the plasma cools down, it sinks again, forming 0.3 Mm wide, boundary zones, the *intergranular lanes*, which appear darker (see figure 1.2). The size of a granule typically varies from 0.3Mm to 2Mm. The granulation is, in fact, the observational proof of the existence of convention cells. Granules are not a stationary phenomenon, as they appear to grow, decay and split in irregular manner, lasting approximately 15 minutes[4].

Larger cells form the *supergranulation* system, with typical size 30Mm and lifetime $\sim 1 day$. Super-granules originate from deeper and hotter layers, thus appear brighter than granules. An intermediate phenomenon may also be present, the *mesogranulation*[6].

-The **_chromosphere_** is a relatively thin layer on top of the photosphere. It starts from an altitude of 500km, where temperature is minimum (4300 K) up to 2000 km above the photosphere. At this altitude, temperature rises to $\sim 2 \cdot 10^4$ K, which favors emission from hydrogen ($H\alpha$). The $H\alpha$ emission produces a reddish color, naturally visible only during the first and last seconds of a solar eclipse. It is less dense and more transparent that the photosphere. The most prominent chromospheric feature are spicules, 10Mm high plasma jets observed at the limb in $H\alpha$ emissions. When projected on the disk, these structures are called dark mottles. It is assumed that spicules play an important role in heating the corona and accelerating the solar wind [4]. Other important chromospheric structures are filaments/prominences, gas clouds suspended thousands of km above the chromosphere (see section 1.2.1).

-The chromosphere is separated by the corona by a thin irregular layer, only $\sim 100 km$ thick, called **_transition layer_**, observed in Extreme Ultra-Violet (EUV) emission lines, due to the high abundance in ionized atoms, such as Ca IV, Ne VII, O IV ans Si IV. Energy flows downwards from the hotter corona to the

chromosphere through this layer, where the temperature changes rapidly from 10^6 K to only $2 \cdot 10^4$ K [3].

-The **corona** is the outer region of the solar atmosphere, where the temperature rises again from 10^4 K to over 10^6 K. The corona is traditionally observed during total eclipses, during which the photospheric light is scattered by the coronal gas and produces a pearly white crown surrounding the Sun [6].

Due to high temperatures at the corona, H, He as well as other atoms, such as O, C, N, are ionized to bare nuclei. Only heavier atoms, such as Fe or Ca, can retain some electrons. These highly ionized elements produce bright spectral lines at the visible and ultraviolet wavelengths, which can be achieved in these very high temperatures [4]. The heating of the solar corona has been one of the greatest challenges of modern physics. The energy needed can be found in the magnetic fields, and magnetic reconnection and MHD waves are the two most prominent mechanisms that transform the magnetic energy to heat [4].

Helmet streamers are one of the most characteristic structures of the corona. They are bright structures that extend above the limb, lying above prominences or active regions. They consists of both open and closed field lines. The density is increased by a factor of 3-10, due to trapped plasma in the closed field lines. The solar wind stretches the open field lines, creating a peak-like structure extending away from the Sun, in the shape of a helmet[4] (figure 1.4). Another significant structure observed at the corona are *coronal holes*. They are cooler and rarer regions of the corona, where magnetic field lines are open. Near solar maximum, they are mostly found at the solar poles, while at maximum can be found all over the disk. They emit highly in X-ray and last 7-8 years [4].

Figure 1.2: Granules on the photosphere. Image credit: Hinode JAXA/NASA/PPARC
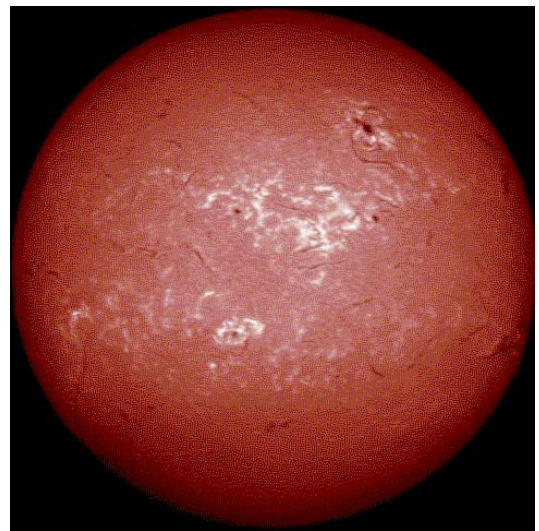
Figure 1.3: Hα image of the chromosphere. Image credit: NASA

1.1.3   The Solar Wind

The outer corona is not in hydrostatic equilibrium, but it expands outwards as the so-called **solar wind** and fills the interplanetary medium, forming the *heliosphere*. At a certain distance, the pressure of the solar wind is balanced by the interstellar flow, defining a natural boundary called the *heliopause*.

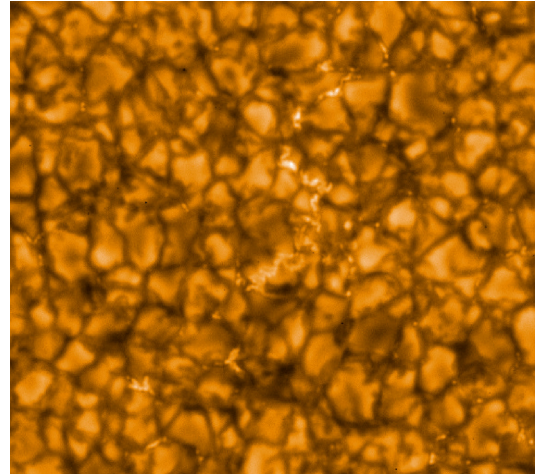[3]https://solarscience.msfc.nasa.gov/t_region.shtml
[4]https://solarscience.msfc.nasa.gov/corona.shtml

Figure 1.4: HDR image of the solar corona during the total eclipse of 21 August 2017. Characteristic structures, such as helmet streamers and coronal holes are clearly visible.
Image Credit & Copyright: Nicolas Lefaudeux

1.1.3.1   Physical Properties

The solar wind plasma originates from thin flux tubes found in supergranule and granule boundaries [4]. It mainly consists of protons and electrons, but a small fraction of about 5% are ionized helium nuclei [8]. It is noteworthy that the solar wind velocity is not radial, but forms a 1.5^o angle with the equatorial plane. Hence, angular momentum is transferred to the solar wind, slowing the Sun down noticeably throughout its lifetime[4]. [9] calculated that the average loss of angular momentum is 2.2×10^{30} erg during the last nine millennia, equal to the average value during the last two decades.

The solar wind consists of two components. The *slow solar wind* and the *fast solar wind*. The slow component has an unclear origin and is remarkably variable. During solar minimum, it originates from the boundary regions between coronal holes and streamers in high latitudes, having an average speed of 400 km/s at 1 AU. At solar maximum, it streams from coronal holes as well as active regions at all latitudes, reaching a speed of 900 km/s. At solar minimum it has an average density $\sim 10^6\ m^{-3}$, magnetic field strength $\sim 1 - 10$ nT, proton and electron temperature $\sim 10^4$ and $\sim 10^5$ correspondingly, while at maximum all physical quantities can be enhanced by 1-2 orders of magnitude.

The *fast solar wind* originates in the coronal holes, flowing from polar regions at solar minimum and at all latitudes from narrow, slower streams. Elements with low first ionization potential (FIP) have a lower abundance than at the slow wind, hence indicating a photospheric origin. While the proton density is higher than the slow solar wind, the electron density, and the mass flux $(10^{12}m^{-2}s^{-1})$ are the same [4]. At 1AU, the fast solar wind has a speed ~ 750 km/s and is rarer, with a density $2.5 \cdot 10^6$ m^{-3} [4].

1.1.3.2 The Interplanetary Magnetic Field

The solar wind carries magnetic field from the Sun towards the interplanetary space, known as ***inter-planetary magnetic field*** (**IMF**). Due to the Sun's rotation the IMF forms a spiral structure, called the *Parker spiral*. The angle ψ between the the radial direction and the magnetic field is given by:

$$tan\psi = \frac{\Omega}{V}(r - r_\odot) \tag{1.1.2}$$

where Ω is the solar angular speed, V the solar wind speed and $r_\odot$ the solar radius. While r increases, the Parker spiral approaches the Archimedean spiral. The length of a Parker spiral connecting the Sun to the Earth is $\approx$1.15AU and $\psi \approx 45^o$, provided V=400km/s. On the equatorial plane ($\theta = \pi/2$) the magnetic field and solar wind speed are $\vec{B} = B_r\hat{r} + B_\phi\hat{\phi}$ and $\vec{v} = v_r\hat{r} + v_\phi\hat{\phi}$ correspondingly.

The radial component is $B_r \propto r^{-2}$ and at large distances $B_\phi \propto r^{-1}$, meaning that it decreases more slowly than the radial component B_r, explaining the spiral structure. Out of the equatorial plane, the picture is more complicated. The magnetic field structure has a helical structure between the equatorial plane and the poles. For the undisturbed solar wind, the field lines are sufficiently close to the Parker spirals.

Of course, the above description is a simplification. Coronal holes are not static, but change location and shape constantly. At solar minimum, the magnetic field is approximately poloidal and the coronal holes are mostly found at the poles, with opposite polarities. The frozen-in magnetic field is dragged within the solar wind, hence a current is formed, called *heliospheric current sheet*, (figure 1.5), which separates solar wind regions with opposite magnetic polarity. At solar maximum, the IMF structure is much more variable and complicated, due to the fact that polar coronal holes are smaller in size but more smaller-scale opening and closing structures are found at lower latitudes. The joint ESA-NASA mission Ulysses, which operated from 1990 to 2009 and was the first spacecraft to fly above the ecliptical plane, made several very important observations. It revealed that the polar magnetic field is much weaker than expected, but also that the solar wind weakens over time.

1.1.3.3 Shocks in the Solar Wind

Various types of shock waves are found in the solar wind. One important class of shock waves are those formed ahead of fast CMEs, when the speed of the latter exceed the local Alfvén speed (see subsubsection 1.2.4). Other types of shocks are formed when the solar wind meets the magnetospheres of planets as well as the interstellar plasma flow (heliopause).

Another important type of shocks are those formed due to the difference in the speed of solar wind flows. The curvature of a spiral connected with the slow solar wind is more curved than one connected with the fast solar wind. In case a slow flow is succeeded by a faster flow, an interaction region will be formed, assuming that they are nearly ideal magneto-hydrodynamic (MHD) flows and field lines can not cross. If the difference of the speeds is bigger than the local Alfvén speed, a steep boundary is formed. This structure is called **Co-Rotating Interaction Regions (CIR)**. A fully developed CIR exhibits a forward shock (FS) ahead of it, which is an abrupt increase in magnetic field strength, solar wind plasma
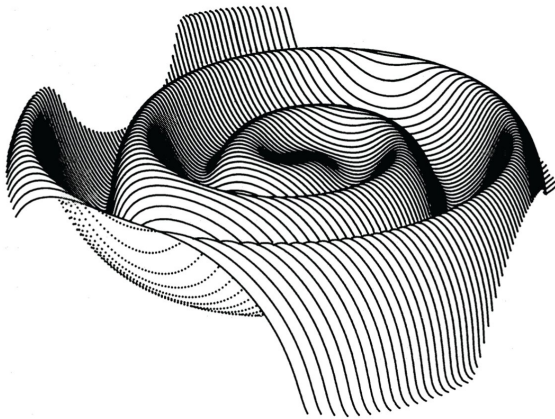
Figure 1.5: The heliospheric currect sheet, resembling a *ballerina skirt*
CREDIT: J. R. Jokipii, University of Arizona
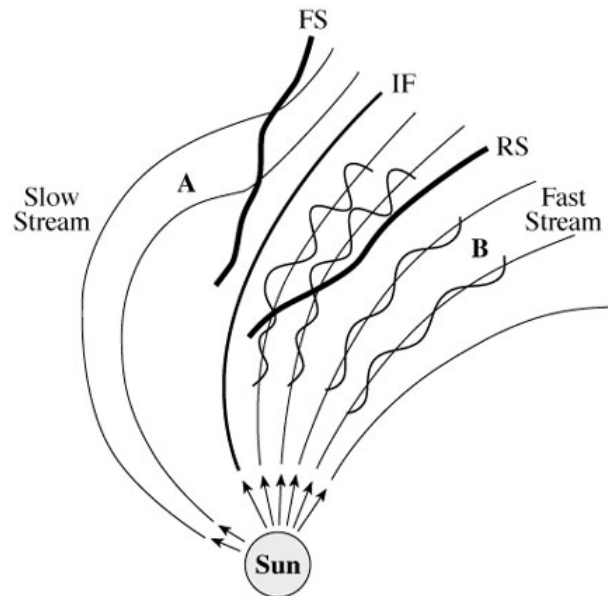
Figure 1.6: A CIR formed due to the interaction of a slow stream (A) and a fast stream (B)
Copyright 2010, Professor Kenneth R. Lang, Tufts University

density, solar wind speed and temperature. A reverse shock (RS) is also formed behind it, which is, in a similar manner, a sudden decrease in magnetic field and density but an increase in solar wind speed and temperature. The interface (IF) region between those two shocks exhibits strong magnetic fields. (figure 1.6).

CIRs are prominent structures during the minimum of the solar cycle, but also present throughout the whole cycle and have been to cause decreases in the intensity of cosmic rays. Moreover, CIRs can serve as accelerators. Particles can be accelerated when trapped between the forward and reverse shocks of a CIR and also due to scattering from waves and fluctuations in the solar wind magnetic field [10], [11]. It has also been proposed, that particles can also be accelerated up to 10 MeV at the compression regions between the shocks of the CIRs, where the efficiency of the acceleration is dependant on the compression levels [12].

1.1.4   The Sun's Magnetic Field

Most solar phenomena owe their existence to the the dynamic nature of the solar magnetic field. These processes are directly related or result from the solar activity, which follows a periodic pattern. The most important indicator of the solar activity is the behavior and evolution of active regions[6].

1.1.4.1   Active Regions, Sunspots and the 11-year Cycle

Active regions (ARs) are bright spots of emission, found within $\pm 30^o$ of the equator and represent moderate concentrations of magnetic flux with mean fields of 100 G. They can be observed in a wide range of the electromagnetic spectrum, from radio-waves to X-rays. Their spectral profile can provide useful information for their three-dimensional structure from the photosphere to the corona[4].

ARs are formed, when magnetic flux tubes are created due to motions inside the convection zone. These tubes emerge to the photosphere due to magnetic buoyancy (figure 1.8). In the photosphere, active regions appear as groups of **sunspots**, dark regions of more intense magnetic field, surrounded by faculae.

The size of sunspots range from 3 to 60Mm wide. They exhibit strong magnetic fields and as a result, low temperatures, thus appearing as dark spots on the hotter photosphere. The center of a sunspot is called *umbra*, with a temperature of about 4100 K and a strong magnetic field $\sim 3000G$, which dominates the plasma. Around the umbra, there may be a *penumbra*, a less dark region, consisting of bright and dark filaments (figure 1.7).

Fully developed sunspots appear in pairs, or in larger groups, as the magnetic field emerging from one sunspot must return to another. A sunspot pair exhibits opposite polarity, consisting of the *preceding* and the *following*. Generally, the preceding sunspot has the same polarity of the hemisphere the group is in, while the following has the opposite[4].

The behavior of sunspots exhibit a periodical pattern of 11 years, during which the number, position and behavior of sunspots changes. This is called the *sunspot cycle*, during which the solar activity changes significantly. At the beginning of a new cycle, the sunspot number is lowest, even zero and the solar activity is at its lowest. New sunspots start to appear at mid latitudes (30°-40°) at both hemispheres, which later on begin to emerge at lower latitudes, closer to the equator. Individual sunspots have a relatively short lifetime, but the overall number increases. At solar maximum, the sunspot number is highest and they are closest to the equator. At the end of each cycle the polarity of the solar magnetic field is reversed and a new ones begins. It takes approximately 22 years for the magnetic field to return to the same polarity, which is often called the *Hale cycle*[6]. The solar cycle changes in period and intensity. Each cycle may differ in duration and its maximum can be less intense [6].
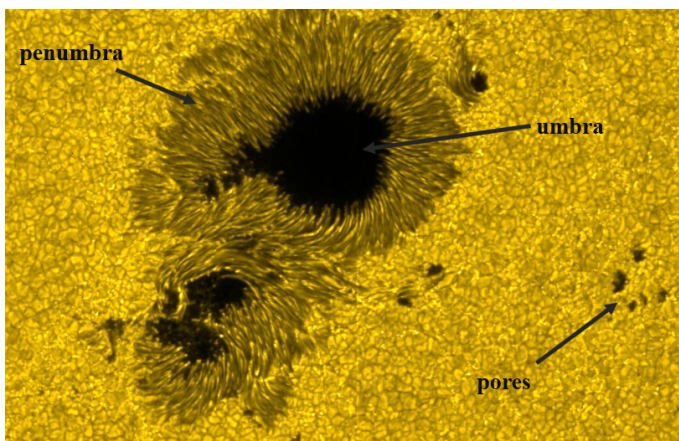

Figure 1.7: Two sunspots on the photosphere, The dark umbra and the penumbra are clearly visible, as well as the pores and the granular surface of the Sun.
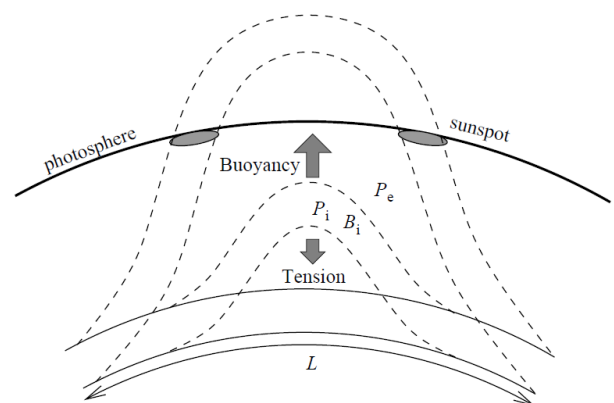Edited, Original Image Credit: Hinode JAXA/NASA

Figure 1.8: The emergence of a flux rope from the convection zone, due to magnetic buoyancy. Image Credit: [6]

1.1.4.2   Generation of the Solar Magnetic Field

The solar magnetic field as known today is thought to be the remnant of the magnetic field of the interstellar cloud, which collapsed and formed the Sun. The first complete model of the solar magnetic field, that explained basic features of the periodical solar activity and sunspot cycle, was the *Babcock model* (1961). It was later preceded by a number of newer models, but the exact mechanism that generates the solar magnetic field is still unknown.

The Babcock model [13] is based on the idea that the magnetic field is generated by a dynamo and assumes that the solar cycle is divided into five stages. At first (*stage 1*) the solar magnetic field is nearly dipolar with a magnitude ~ 1 Gauss. All magnetic lines emerge from high heliographic latitudes and lie in the meridional planes, while in the solar interior are found at a region 0.1 $R_\odot$ below the photosphere. At *stage 2*, the field lines are distorted and stretched due to differential rotation. After a few rotations, a field line can be wrapped several times around the Sun. The increase in the density of the field lines results in the production of a magnetic field component parallel to the equator and the increase of the magnitude of the field to a few hundred Gauss. Physically, the energy of the differential rotation is transformed to magnetic energy. The convection motions distort the field lines and twist them into flux ropes. At *stage 3*, the magnetic flux ropes immerse to the photospheric surface due to the high magnetic buoyancy, forming the active regions at $\pm 30^o$ latitude. The active regions from both hemispheres travel towards the equator, as the magnetic field magnitude increases in lower latitudes. During *stage 4*, the active regions are divided, presumably due to meridional flows. The following sunspots migrate towards to poles, while the preceding towards the equator. The following sunspots and the initial dipolar field are equally neutralized, while the preceding sunspots with each other. The final result is the annulment of the overall dipolar magnetic field. The total amount of magnetic flux of the active regions is greater than the flux of the initial fiend, leading to the reversal of the magnetic field at *stage 5*.

1.1.5   The Sun's Chemical Composition

The chemical composition of the Sun can be estimated by analysis of the atmospheric spectra and theoretical models for the solar interior. The most abundant element is H, followed by He, with photospheric abundances 90.965% and 8.889 % (of total number of atoms) correspondingly [5].

Light atoms, like Lithium (Li), Beryllium (Be) and Boron (B) are also found in very small abundances in the solar spectrum. Li reaches extremelly low values, even in comparison with meteorites and varius stellar spectrum. It is thought to be depleted in the solar convection zone[14]. Moreover, the solar spectrum contains Carbon (C), Nitrogen (N) and Oxygen (O), and other non-metals. Metallic elements are also found, such as Fe, Mg etc as well as various nobel gases [14]. Molecules have also been found in the photospheric as well as in sunspot spectra[8].

The composition of the solar atmosphere is not the same in each layer. The photosphere is a well mixed region, due to its position above the convection zone, and consists of a large number of elements. On the other hand, the upper atmospheric layers are inhomogeneous and highly variable.

---

[5]https://nssdc.gsfc.nasa.gov/planetary/factsheet/sunfact.html

The coronal abundances are different than those in the photosphere. Studies have shown that in the corona elements with FIP (< 10 eV), such as Mg, Si, and Fe are enhanced relative to those with high FIP (>11 eV). Low FIP atoms are ionised in the photosphere and chromosphere and can be easily swept up in the corona, relative to neutral atoms. Abundances in the solar wind are similar to those in the corona, due to its origin. However, differences between the slow and fast solar wind are found. The fast solar wind stems from the cooler coronal holes, thus has lower charge states and is thought to be the closest in situ measurement of photospheric abundances [15].

1.2   Solar Eruptions

The Sun is not a quiet place, but it is dominated by violent, eruptive phenomena, which disrupt the interplanetary space. Solar energetic particles (SEPs) are a direct effect of these phenomena and, in order to understand them, a description of these eruptions is necessary. Solar eruptions can be associated with solar prominences, although they are usually quiet, long-lasting structures with a peaceful evolution. In many cases prominences can erupt, leading to flares and coronal mass ejections (CMEs), but the overall mechanism that trigger them is not yet fully understood [4].

Flares and CMEs should not be interpreted as two unrelated events or two phenomena that the one is the result of the other, but rather as parts of the same dynamic process on the Sun. Solar energetic particle events are in most cases associated with both flares and CMEs, conforming with the above image. CMEs related with SEP events, but not associated with a flare are very rare. Similarly, strong flares leading to SEP events not associated with CMEs are also infrequent [16]. In fact, the most energetic solar phenomena are related to intense flares, regardless of the detailed physics. This empirical correlation between solar parameters is termed the *Big Flare Syndrome* (BFS), first introduced by [5]).

1.2.1   Prominences

Solar prominences are gigantic gas clouds suspending thousands of kilometers over the solar surface. When observed at the limb during eclipses, they appear bright, in comparison with the much rarer corona (figure 1.9). However, when captured in $H\alpha$ images of the disk, they appear as dark ribbons of the hotter chromosphere, called *filaments* (figure 1.10). The spectral analysis yields the abundance of Hydrogen, Helium and several metals, such as Aluminium, Iron, Calsium, Magnesium and other[8]. The reddish color observed with spectroscopes is due to the dominant $H\alpha$ line of Hydrogen.

Prominences can reach up to 600 Mm above the limb. The plasma is supported at such heights against gravity due to the Lorentz force $\vec{j} \times \vec{B}$. They have a density $\sim 10^{17} m^{-3}$ and a temperature 5000-10000K, while at the region connecting the prominence with the corona the temperature rises to 1MK and the density falls to 3 orders of magnitude. They have the form of vertical sheets and can survive for even a year. Due to the relatively high magnetic field ($\sim 1mT$) and the low temperature of order 10^4 K, beta is rather small, indicating that indeed the magnetic field is the factor determining their structure.

Prominences can decay peacefully but occasionally erupt in association with a flare or/and a CME. The disappearance of a filament, is in fact, a strong indicator of the location of a CME. Prior to the eruption, the prominence is activated, which is observed as darkening (on the disk) or brightening (at the limb), and plasma motion is increased. The plasma material may drains away or an eruption is triggered. Other types of activations are caused by nearby solar eruption, i.e. solar flares.

1.2.2   Radio Bursts

Radio bursts are emissions in the low-frequency spectrum originating from the Sun and categorized according to their observational properties in four groups: Types I-IV. All are produced by suprathermal
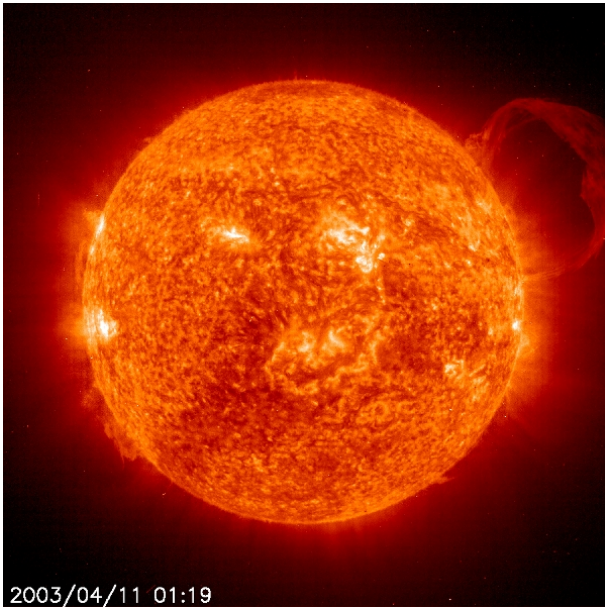
Figure 1.9: A solar prominence, extending over 30 times the size of Earth out from the Sun, taken by the Extreme ultraviolet Imaging Telescope (EIT) (top right). Image Credit: SOHO (ESA & NASA)
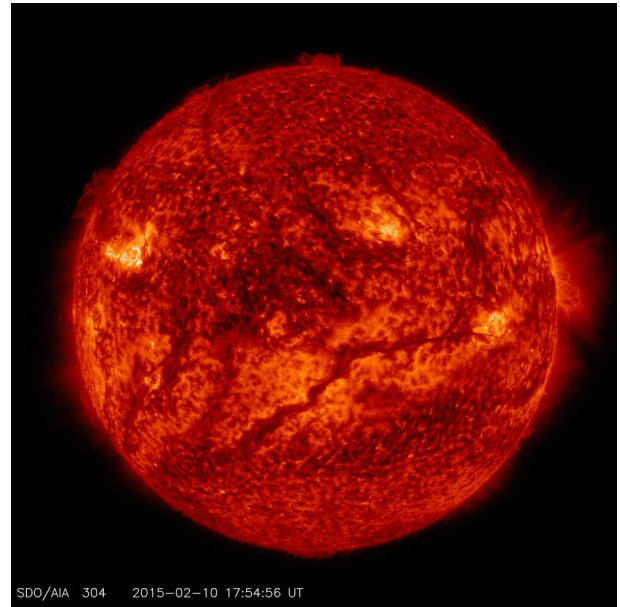
Figure 1.10: Image of filament on the solar surface, taken in multiple wavelengths (dark line across the disk).
Image Credit: NASA/SDO

electrons and are good indicators of the source as well as the medium properties, such as the ambient density, magnetic field strength, level of turbulence

Type I radio bursts, also called noise storms are radio emissions lasting from hours to days with brightness temperatures from 10^7-10^9 K, which refers to the temperature of a thermal source emitting the same amount of radiation. Type II bursts are observed at frequencies 0.1-100 MHz, lasting several minutes. Their slow drift to lower frequencies with a rate ~1MHz/s suggest an outward motion of approximately 1000km/s. They are attributed to propagating shock waves and the frequency f of the emitted radiation is related to the electron plasma density n_e according to the formula $f = 8.98 \cdot 10^{-3}\sqrt{n_e}$ [MHz] [17].

Type III bursts vary from 0.1MHz to 1GHz and present a fast drift to low frequencies with a rate 100 MHz/s. They are connected to flares and attributed to non-thermal emission of high energetic electrons. Type IV burst are broad-band, partly circularly polarized radiation. They are not directly connected with flares, but observed shortly after the flare onset. This type of radio burst originated from sychrotron emission from energetic particles of a few keV trapped within large-scale magnetic loops [6].

1.2.3   Solar Flares

A flare is a sudden release of energy of order $10^{19} - 10^{25}$ Joule on the Sun, lasting from a few minutes to a few hours and with a typical energy release rate $\sim 10^{19} J/s$[4]. Their emission extends over a wide range of radiation: radio, visible, extreme ultraviolet, X-rays, y-rays and particle emission[7]. Most flares are observed at the corona and the chromosphere, while the most powerful ones can also be seen in photospheric white light, as the very first one observed in 1859 by British astronomer Richard Carrington[8]. Flares are usually detected near active regions, where the photospheric magnetic field gradient is significant [4].

The energy needed for a flare can be found in non-linear magnetic fields in the solar atmosphere, usually accumulated in active region prominences and released via magnetic reconnection. The energy is transformed mainly to fast-particle energy, radiation, heat and plasma motions, which in turn results to radio bursts, MHD waves and shock waves [4].

According to [4], flares are categorized in many different ways, according to their characteristics. They can flares can be *impulsive* or *gradual*. The former type shows impulsive behavior while the latter has a longer duration and is often associated with energetic particles. Another categorization is between *confined/compact* flares, which are confined by a strong magnetic fields in such extent that do not lead to eruptions, and *two-ribbon/eruptive* flares, which are the largest and are associated with prominence eruptions leading to a CME.

Figure 1.11: A X1.1 flare captured by NASA's Solar Dynamics Observatory (SDO) on Oct. 19, 2014, in extreme ultraviolet light of 131 Å (typically colored in teal). The flare is the intense brightening on the left. Image Credit: NASA/SDO

A *two-ribbon* flare (see figure 1.12) is characterised by the formation of two Hα ribbons on each side of the prominence, hence the name. The magnetic arcade supports the prominence, above the neutral line in a active region, and stores magnetic energy. At some point, the structure erupts outwards. The exact mechanism that triggers the flare is not yet fully-understood.

Figure 1.12: A two ribbon flare. Image Credit: [6]

The flare ribbons are connected by an arcade of flare loops of temperatures from 10^4K to 10^7K, leading to different E/M emissions: Hα (10^4K), UV (10^5K) and X-ray (10^7K). UV, Hα emission and soft X-rays are produced by the thermal distribution of the plasma. Hard X-ray is due to bremsstrahlung radiation of highly accelerated energetic particles, while gamma rays are produced by highly energetic ions, which also result in heating of the photosphere and white light emission.

According to [6], flares are also associated with radio bursts of types II, III and IV. Type III radio bursts show the presence of beams of relativistic electrons in open field lines in the corona, while type II are associated with fast shock waves, produced by a CME. Also, long-lasting type IV radio bursts indicate the presence of a high-energetic plasma cloud above the flare location. In general, non-thermal radiation last for a shorter period than thermal radiation, considering that energetic particles lose their energy faster due to collisions in comparison to heated plasma, which loses energy in a slower rate.

Most flares develop in four basic stages, as described by [4]:

-The *preflare phase*, lasting several minutes, is characterized by an increase in soft X-ray radiation and the activation of the prominence. The onset of reconnection is thought to trigger the impulsive phase.

-During the *impulsive phase*, lasting just a few minutes, microwave and a hard X-ray radiation is produced, due to highly energetic electrons. Physically, at this stage the stored magnetic field is suddenly transformed into heating of plasma, radiation and kinetic energy (particle acceleration). Hard x-ray radiation is usually emitted from the footpoints of the loop.

-The *rise* or *flash* is a period from 5 minutes to 1 hour, during which both the intensity and area of soft X-ray and Hα emission increase, while the prominence rapidly erupts. During this phase, all highest-energy emissions reach their peak [8].

-The last phase, called *main* or *decay phase*, the intensity decreases slowly within 1 hour-1 day. This stage is dominated by thermal emissions (soft X-ray, UV and optical).

Flares are classified as A, B, C, M and X, depending on their 1-8 Å X-ray peak energy flux near Earth, where each class is ten times stronger than the proceeding. The peak X-ray flux of each flare is shown in table 1.1. Each class is also divided 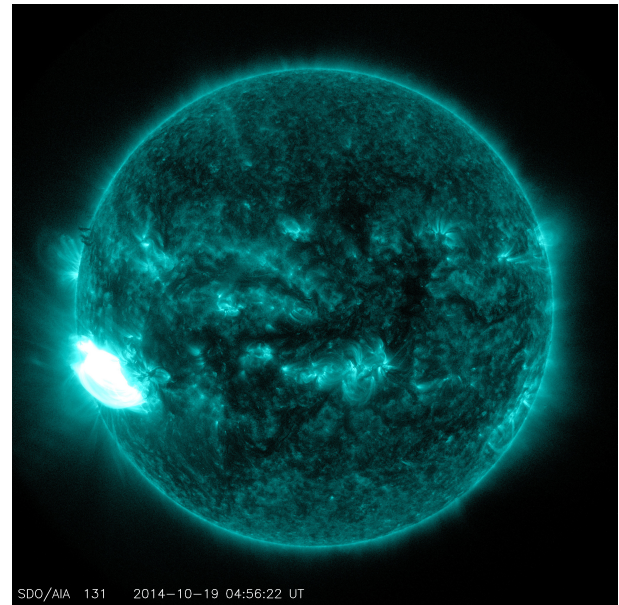in a logarithmic scale from 1 to 9, so that, for example, a M2 flare reaches an intensity of $2 \cdot 10^5 \ W/m^{-2}$ and is twice more powerful than a M1 flare ($10^5 \ W/m^{-2}$). X-class flares can go higher than X9.

Class	A	B	C	M	X
Peak Energy Flux ($W \cdot m^{-2}$)	$< 10^{-7}$	10^{-7} - 10^{-6}	10^{-6} - 10^{-5}	10^{-5} - 10^{-4}	$\geq 10^{-4}$

Table 1.1: Flare Classes

Class A and B flares are rather common and near background flux levels. C flares are bigger, but still unnoticeable from Earth. M flares can cause small blackouts and even endanger astronauts and spacecrafts. X flares are the most powerful of them all, having a strong impact on the interplanetary medium and planets. They can also cause geomagnetic storms, resulting in blackouts, disruption of power grids and radio communication[6]. The largest flare ever recorder was a X28 flare in 4/11/2003, associated with a CME of a speed 2300 km/s[7].

1.2.4 Coronal Mass Ejections

Coronal Mass Ejections (CMEs) are large-scale magnetically suspended solar plasma bubbles, originating from the Sun and travelling to the interplanetary medium with a typical mass of 10^{12}-10^{13} kg[6]. They can cause geomagnetic disturbances, are associated with interplanetary shocks and solar energetic particle events. In extreme cases, they can cause damage to spacecrafts and airplanes, endanger astronauts, cause power cuts and radio communication problems[4]. CMEs travel through the interplanetary medium, interacting with the ambient solar wind and magnetic field, or even with other CMEs, mak-

---

[6]https://www.nasa.gov/mission_pages/sunearth/news/classify-flares.html
[7]http://www.esa.int/Science_Exploration/Space_Science/Extreme_space/The_biggest_solar_X-ray_flare_ever_is_classified_as_X28

ing them a very complex phenomenon[18]. When detected on the interplanetary medium, are called *Interplanetary CMEs*[19].

1.2.4.1   CME characteristics and eruption

The name $coronal$ mass ejection is not indicative of the origin of the CME, but of the observational location. Although CMEs are observed at the corona, the eruption actually originates at the lower solar atmosphere [6]. CME eruptions can be observed at any region, but mostly occur at lower latitudes, especially near solar minimum[20]. The CME eruption is detected in coronal streamers, whose cores contain prominences. Such structures inside active regions usually trigger more energetic and violent CMEs. A CME eruption is usually accompanied by a flare, usually a two-ribbon flare, as these two phenomena are strongly connected to each other [4].

The exact mechanism that triggers a CME is not fully understood. However, it is generally accepted that, magnetic energy at the solar atmosphere is sufficient to provide the energy needed for the CME to escape the gravitational field of the Sun and reach the kinetic energies observed[8]. Some studies propose, that the force-free magnetic fields can not provide sufficient energy to accelerate a CME, in contrast to flux ropes, which can store large amounts of energy [21]. Generally, flux ropes are fields with lines winding about each other a full turn or more in the corona. CMEs serve as a mechanism for the removal of magnetic helicity and large quantities of mass from the solar corona[21].

CMEs are very common, as their rate of occurrence is $\sim$1/day at solar minimum and 3-4/day at solar maximum[6]. CMEs are observed in visible light by *coronographs*, instruments that block the photospheric light and reveal the much rarer corona. The white light is produced due to Thomson scattering of the photospheric light by free electrons within the CME[8]. The brightness can be used to estimate the density, mass and other characteristics of the structure [6].

Their speed can vary from 50 to more than 2000 km/s and CMEs facing the direction of Earth take approximately 2-5 days to reach it[4]. The CME speed is not constant, as CMEs slower than the ambient solar wind speed tend to accelerate, and vice versa. When their speed exceeds the local Alfvèn speed, a shock is formed. The faster CMEs are associated with radio II bursts, due to the propagating shock wave. Assuming synchrotron emission, radio emissions show that the magnetic field inside a CME $\sim 4 - 5G$ at at 3-5 R$_\odot$, also indicating a low beta value of only 0.1[4]. Furthermore, their angular widths vary significantly, as they can be narrow or even extend towards all directions, then called *halo CMEs*[4].

According to [21], the typical structure of a CME consists of three main components: a bright high-density outer loop, a rarer darker cavity and a higher density bright core inside the cavity. Inside the cavity, a flux rope of helical fields may be found. The front loop of the CME contains a bipolar or quadrapolar magnetic field, connected with the interplanetary medium. In many cases, the CME is anchored to the coronal base. However, deviations from the above picture are observer, for example some CMEs do not have bright cores. The structure of the CME originate from the corresponding coronal helmet streamer, prior to the eruption: a dense helmet dome and a quiescent prominence inside a dark cavity. Observations also show that slower CMEs preserve the three-part structure of the helmet streamer[4].
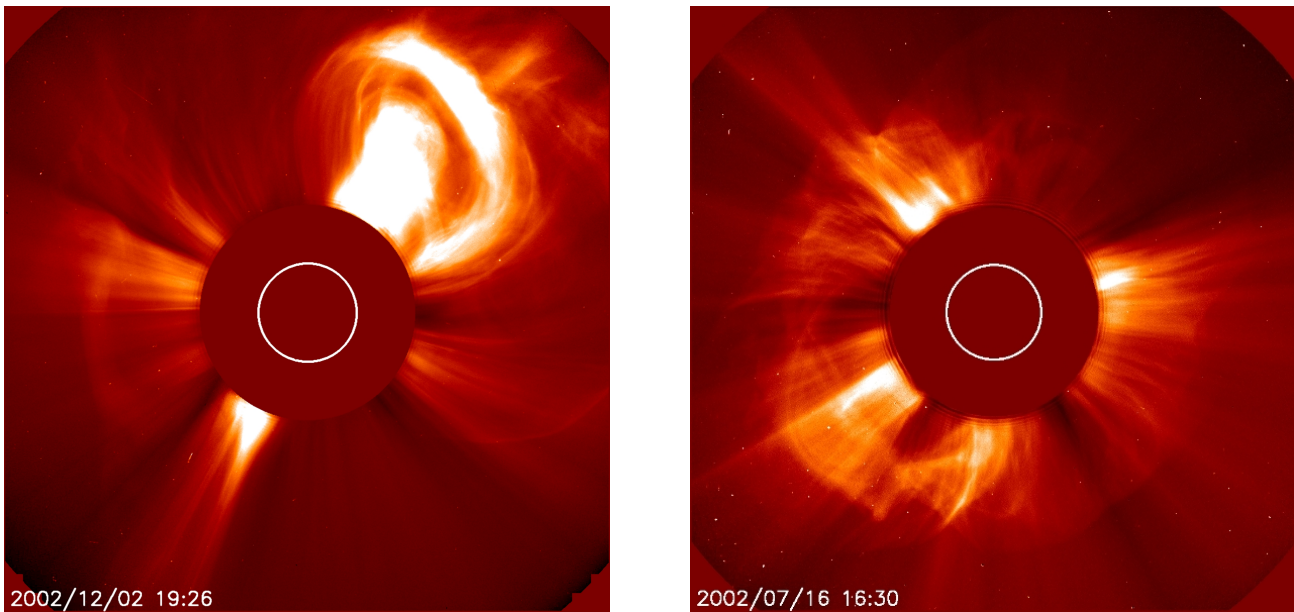
Figure 1.13: Two CMEs captured by the Large Angle and Spectrometric Coronagraph (LASCO). Left: The classic shape of a CME is found: a front loop, a dark cavity with a bright core. Right: a Halo CME. Energetic Particles are visible as bright dots, due to saturation of the corresponding pixels. CREDIT: SOHO (ESA & NASA)

1.2.4.2 ICMEs

Interplanetary Coronal Mass Ejections (*ICMEs*) are solar wind structures and the counterparts of CMEs at the Sun. Generally, an ICME drives a shock, separated with it by a sheath region containing compressed, heated and often turbulent solar plasma[22]. Observations of counter-streaming suprathermal particles indicate that an ICME can be magnetically connected at one or both ends with the Sun and only at large distances (>5 AU) is fully disconnected from the Sun [4]. A schematic represantation of an ICME is shown in figure 1.14, adopted by [23].

An ICME generally has the following characteristics, detected by in situ measurements:

- The magnetic field within the ICME is larger than the IMF
- The magnetic field inside the ejecta is relatively smooth, compared to the IMF. Between the ejecta and the shock waves lies a turbulent sheath region
- Plasma beta is decreased: $0.01 \leq \beta \leq 0.4$, while in solar wind $\beta \geq 0.4$
- The proton temperature T within an ICME is: $T \leq \frac{T_{exp}}{2}$, where T_{exp} is the expected proton temperature in the solar wind and is estimated by the following relation [24]

$$T_{exp} = 640 \cdot V_{sw} - 1.56 \cdot 10^5 \text{ [K]}$$

where V_{sw} [km/s] is the solar wind speed.

The density, mean magnetic field and temperature of the ICME decrease with heliocentric distance. The change in distance is due to the expansion of the ICME, as it moves away from the Sun. As mentioned above, CMEs tend to accelerate or decelerate during propagation, due their interaction with the interplanetary medium, thus the ICME speed differ from the speed of its CME counterpart. Studies have shown that the ICME speed shows little variation with respect to radial distance, however ICMEs tend to converge with the ambient solar wind speed[25].

Although it is not clear how the different structures of the CME evolve during the propagation of the structure in the interplanetary medium, it is accepted that the bright front corresponds to the sheath region of the ICME. Moreover, the flux rope of the magnetized ejecta is found in the dark cavity, where the low pressure is balanced by the high magnetic pressure. Within an ICME, the amplitude of magnetic field variations is lower in comparison with the solar wind. However, the sheath region contains large scale fluctuations, due to compression by the ejecta [25].

The majority of ICMEs have enhanced He/H abundance ratios, sometimes exceeding 25%, while in the solar wind He/H$\sim 3 - 5\%$. This ratio is often enhanced at magnetic clouds and it can be indicative of the ejected material at the Sun. Usually they are also associated with elevated ionic charge states, while magnetic clouds also show high oxygen charge states [19]. ICMEs with low ionic charges have also been reported, however.
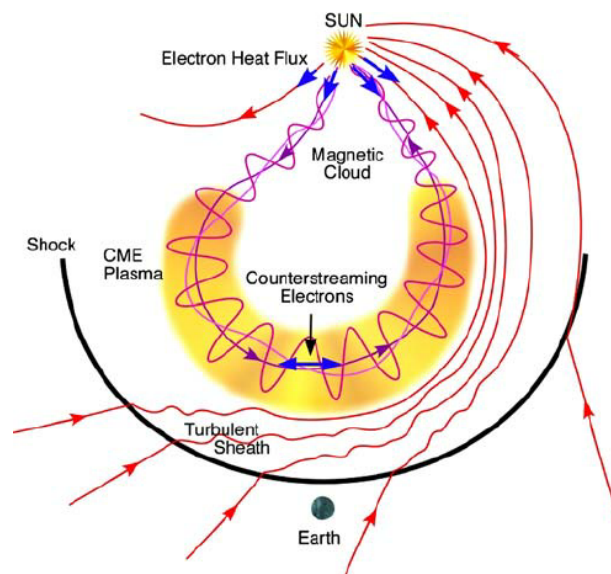
Figure 1.14: Schematic representation of an ICME with a magnetic cloud-like field structure [23]

1.2.4.3   Magnetic Clouds

A magnetic cloud (MC) is a subset of ICMEs, which fulfil the following criteria[26]:

(1) the magnetic field vector rotates smoothly through a large angle
(2) the magnetic field strength is higher than than average ($> 10nT$)
(3) the plasma temperature and β are lower than average

Although many large scale IP structures (for example CIRs) can exhibit some of the above characteristics, the combination of all three is unique for MCs. Most MCs can be modeled by a large-scale cylindrical magnetic force-free flux rope $\vec{\nabla} \times \vec{B} = \pm\vec{B}$, with a circular or elliptical cross-section spiralling within, however not all MCs fit this model [19]. ICMEs with non MC features may have more complex magnetic configuration [23]. A schematic representation of an ICME with MC structure is shown in figure 1.14.

MCs are only a subset of ICMEs, but the exact percentage is not clear and varies from study to study. There is also evidence that the number of MCs varies with the solar cycle, ranging from $\sim100\%$ at solar minimum and $\sim15\%$ at solar maximum [23]. During most of the solar cycle, the average fraction is

estimated $\sim$30% [22].

1.2.4.4   CME interactions

During the propagation of the CME through the interplanetary medium, it can undergo various interactions. In general these are more likely to occur during solar maximum, due to an overall higher solar activity. The main types of interaction are:

- CMEs are accelerated when they exceed the ambient solar wind speed, and vice verca.
- ICMEs interact with fast wind streams and CIRs, which often leads to the acceleration of ICMEs, enhanced solar wind pressure and intensification of the magnetic field [25]. In some cases, ICMEs and CIRs may form merged interaction regions (MIRs) [27].
- ICMEs can interact with each other. This type of interaction has been observed in many cases and can play an important role in enhanced energetic particle fluxes. The eruption of one CME can be triggered by a previous one (sympathetic) or can originate at the same active region (homologous), or the eruption of two CMEs can be unrelated [18]. In order for two CMEs to interact, the preceding one has to be slower than the next and the two CMEs should spatially overlap. The interaction between two successive CMEs leads to enhanced southward magnetic fields, modifications in the shock and ejecta propagation (speed, magnetic field strength lower plasma beta) [28]. Moreover, enhanced SEP fluxes are often an indicator of CME interaction, as explored by many [29]. Interacting CMEs can be observed in situ as two different well-organized structures or more complex ones, such as shocks propagating within the preceeding CME ejecta or structures that the charapteristics of the CME counterparts cannot be easily distinguised. The total coalescence of two CMEs is often called *CME-CME cannibalism* [30].

1.3 Solar Energetic Particles

Solar Energetic Particles (SEPs) are flux enhancements of high-energy charged particles originating at the Sun. Their energies vary from 10 keV up to several GeV reaching speeds up to 90% the speed of light. SEPs are dominated by electrons and protons, however other elements, from He to Pb, have also been measured [1]. Large SEP events, in which the intensity of high-energy solar protons is sufficient to rise above the galactic cosmic ray (GCR) background at Earth, are called ground-level events (GLEs). These events induce nuclear cascades in the atmosphere, leading to the production of secondary products measured by ground-based detectors, such as neutron monitors[31]. SEPs do not exactly follow the solar cycle, but they do have a periodical pattern [1].

SEPs pose a significant danger to spacecrafts and aircraft, as well as a health hazard for astronauts and flight crews[2],[3]. The first SEP event was reported by Scott Forbush in 1942, who was observing the secondary products of GCRs as well as the decrease of GCR intensities during magnetic storms, called *Forbush decreases*, which are now known to be caused by ICMEs acting as shields. Forbush detected increases from SEPs prior to the Forbush decreases and attributed them solely to the solar flares observed prior to the event [1]. However, we now know that processes both associated with flare and CME-driven shock waves can explain the particle acceleration[32]. However, the exact mechanism is still unknown, as SEPs are observed at 1AU and the processes that take place during their propagation from the Sun to the observer are still poorly understood[33]. This section summarizes the main characteristics of SEPs, the theoretical aspects of acceleration at the Sun and propagation of the particles through the interplanetary medium.

1.3.1 SEP Characteristics

In this section, a number of noteworthy SEP characteristics will be discussed, regarding their abundances, charge ratios and profiles.

1.3.1.1 Two-class Picture

Generally, SEP events are classified to two large classes: *impulsive* and *gradual*. The classification is based on differences related to physical properties of the events.

Impulsive events are generally shorter (≤ 1 day) and less intense. They are characterised by enhanced ^{3}He/^{4}He $\sim 10^3$-10^4 ratios, thus called electron-rich events. They are mainly accelerated in flares, that produce III radio bursts, impulsive microwave and hard Xray bursts. The are also associated with slow, narrow CMEs and solar jets.

Gradual (or large proton) events were originally related with large flares and later with CMEs as well. These events last longer (up to several days), exhibit larger fluences and reach higher peak intensities. They are proton rich, with ratios Fe/O ~ 0.1 and Fe ionisation states of ~ 14. They are associated with type II radio bursts, thus indicating shock- acceleration at the CME.

However, the picture is much more complicated. Events that exhibit characteristics of both categories have been observed numerous times. Indicatively, gradual events have been associated with

type III emissions and can exhibit high ^{3}He abundances. They often exhibit an impulsive part, indicating synergy between flare- and shock-acceleration. Similarly, intense electron events have been associated with CMEs as well [34] . A new category of the so-called *hybrid* events has been taken into consideration, including events that exhibit characteristics of both main categories[35]. It is evident that the particles are accelerated both at the flare and the shock front and that in reality, there is no sharp division between the two classes.

1.3.1.2   Timing

SEP events are also characterized by their onset time, which is the timestamp of the observed arrival times of the particles. The particles transit time is t=L/v, where L is the path length of the particles. Under the assumption that the first particles at each energy have travelled almost-scatter free, the path length of particles should be the Parker Spiral connecting Earth with the source of the event, with typically is $L = 1.11 \pm 0.02\ AU$, depending on the solar wind speed. For a typical value of 400km/s, L=1.2AU. A more detailed analysis uses the equation t=L/v to determine both the path length and the time the particles left the Sun, called *solar particle release (SPR)* time, by fitting the transit time measurements [1].

For most gradual and GLEs events the SPR times occur later in the event, after the radio type II onset, which indicates the formation of a shock wave. For the GLEs the SPR is often after the γ-rays are over. The SPR times of impulsive events temporally coincide with the peak of the flare hard-X rays [1], Electrons usually coincide with radio III bursts. Generally, proton release is thought to be more complicated that electrons. Proton releases are energy-dependant, as the most energetic protons are usually released simultaneously with electrons, whiler lower energy protons 1-2h after the electrons [36].

1.3.1.3   Abundances and Charge States

The abundances and charge states of elements and isotopes are one of the most significant indicators of the particles origin, transport and acceleration mechanism. The ratio ^{3}He/^{4}He is greatly enhanced in impulsive events, in comparison with its very low values (10^{-4}) in the solar wind and the corona. The ^{3}He in impulsive events can not be the product of nuclear reactions in flares, since other secondaries such as ^{2}H, ^{3}H, Li, Be, B etc are not found in SEPs. In reality, ^{3}He particles are accelerated by waves generated in electron acceleration regions of solar flares [37]. Tracing ^{3}He-rich events to their solar sources, indicate an association with narrow CMEs and solar jets [1]. Impulsive events are also iron-rich, with $Fe/O \sim 1$, almost 10 times larger than coronal values.

The average abundances of gradual events are comparable with those in the corona, conforming with the idea of a shock wave gathering coronal and solar wind plasma during its transit. An explanation for the enhanced ^{3}He in some gradual SEPs, is that a CME-driven shock could accelerate suprathermal ion remnants from previous events, which are called *seed population* [1].

Charge states of ions are also different between the two classes of events. Indicatively, in impulsive events $Q_{FE} \sim 20$, while in gradual $Q_{FE} \sim 12$. These numbers indicate different plasma temperatures of $\sim 10 MK$ and $\sim 2 MK$ for impulsive and gradual event sources, correspondingly. Another explanation,

however, is that impulsive sources are found deeper in the corona, in about 1.5 solar radius, and ions are stripped in transit, while gradual sources are higher, in 2-3 solar radii [1].

1.3.1.4   Intensity

The intensities of SEP events depend on many factors, the most important of which must be characteristics of their sources, i.e. the associated flare and CME properties. Generally, most SEP events are correlated with both CMEs and flares. Reports of CMEs associated with SEPs not accompanied by a flare eruption are very rare and also, strong flares not accompanied by CMEs are rarely associated with SEP events, because energetic particles are most likely to remain confined in the coronal magnetic field [16].

Since SEPs are accelerated at the shock driven by the CME, one would expect that the CME speed is strongly correlated with the peak intensity of particles. However, for a given CME speed, the intensity can vary up to 3-4 orders of magnitude. Errors due to geometry must be taken into account: the CME speeds are measured in projection on the plane of the sky, thus show a statistical increase as the distances of the CME source region from the central meridian increase as well. Moreover, the relative speed of the CME and the ambient solar wind determines the formation of the shock, rather than the CME speed it self [38]. The soft X-ray (SXR) peak flux, SXR fluence and duration have been found to correlate with the peak flux, duration, and emission measure of the SEP event. Generally, large flares are more likely to be associated with large SEP events [16]. The soft X-ray peak flux and SXR fluence are found to correlate with the peak flux and duration of the SEP event[39].

The condition of the interplanetary space also affect SEP intensities. First of all, the presence of a pre-existing seed population of suprathermal particles can lead to enhanced intensities. Moreover, the presence of transient structures in the interplanetary space, such as an ICME, can also affect the intensity of SEPs and alter their path. The position of the ICME relative to the Sun and the observer at the time of the SEP event detection can have different results. The effect of interplanetary conditions will be discussed in detail in Section 1.3.3.

1.3.1.5   Longitudinal Distribution

At first glance, particles are expected to follow the nominal Parker spiral originating from their source. The morphology of the interplanetary magnetic field structure, as presented in paragraph 1.1.3.2, dictates that SEP events originating from western sources on the Sun are more likely to be detected on Earth.

However, SEPs can originate from a broad range of latitudes (up to 80° [34]) and longitudes (even up to 360° [40]). This behavior was originally observed in gradual events, but impulsive ones originating at wide longitudinal ranges have also been detected [41]. Transport of particles across magnetic field lines, due to distrurbances created by passing CMEs and wandering of field lines play a crucial role. Extreme propagation cases may imply the existence of "quasi-circumsolar" shocks[40].

Furthermore, the profile of particle intensities and timing depends on the longitude of the source on the Sun, illustrated in figure 1.15. A spacecraft detecting a western event is magnetically well-connected to the Sun and sees a rapid rise in particle intensity, followed by a gradual decrease. The shock arrives later and it may be already weakened or dissipated. An eastern event, on the other hand, shows a slow

rise in intensity, reaching a maximum behind the shock. Lastly, for an event originating at a source near central meridian, the maximum intensity is detected when the shock is passing the spacecraft and may decline abruptly after the shock passage [1].
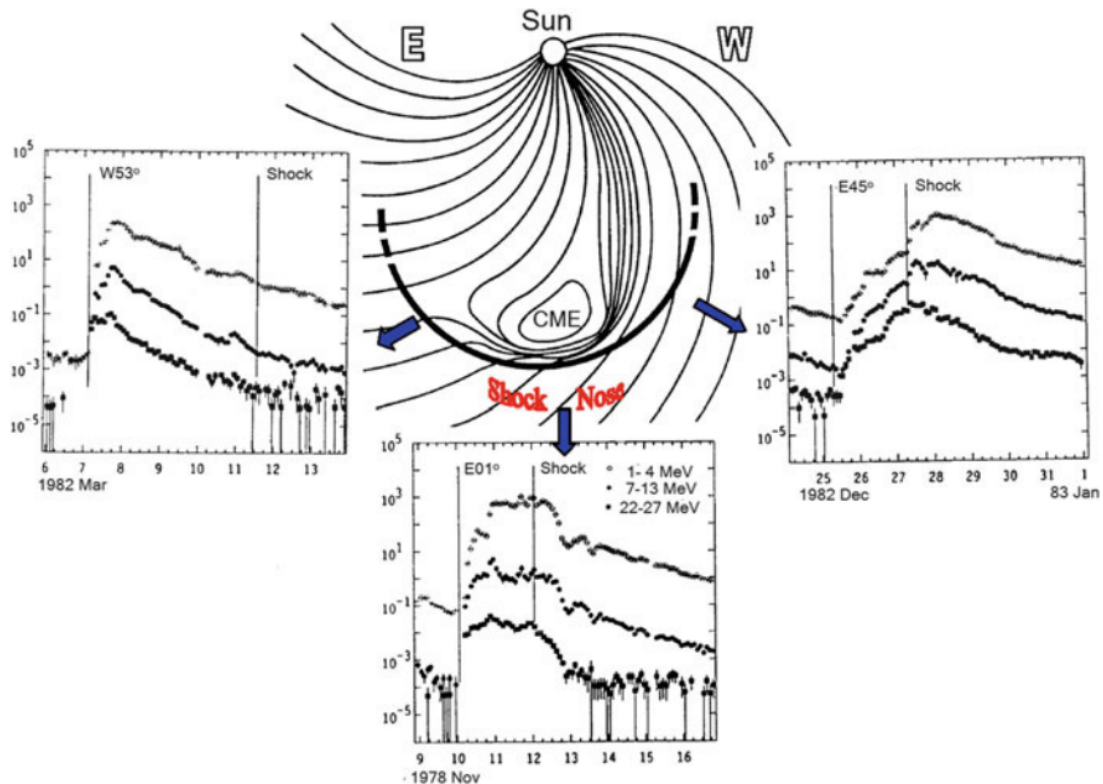
Figure 1.15: Variations of SEP profiles, depending on their source's solar longitude. Image Source: [1]

1.3.2   Acceleration

Acceleration of particles is a universal phenomenon, occurring in a variety of astrophysical objects such as neutron stars, black holes, supernova remnants, astrophysical jets etc and in our own solar system in planetary magnetospheres, interplanetary shocks and solar flares [42]. Cosmic rays and solar energetic particles are accelerated in high energies (cosmic rays can reach even 10^{20}eV) and produce power-low spectra. The only candidate that can provide this amount of energy and accelerate particles away from the source are electric fields[43].

In general, acceleration can be regular or stochastic[42]: Regular acceleration occurs when particles gain energy due to large scale electric fields. Very special conditions are needed to achieve this, due to the high conductive nature of plasma, but can be found in some instances, i.e. in flare reconnection sites. Stochastic acceleration is the process through which there is an average energy increase per particle, under the influence of electric fields induced by small scale magnetic field variations. An example is the second-order Fermi acceleration (see paragraph 1.3.2.1). A major issue arising for most mechanisms is that the particles have to be already accelerated in high energies, the so-called *injection problem*[44].

1.3.2.1 Basic Acceleration Mechanisms

In this chapter, some basic concepts of particle acceleration are presented. The acceleration models described, can be applied universally, from cosmic rays to SEPs. The basic principles were laid in 1949 by the landmark paper of E. Fermi [45], which aimed to explain the origin of the cosmic rays as well as the power-law spectra of cosmic rays equal to 2-3. It was proposed that the acceleration results from the interaction of particles with moving magnetic fields in the interstellar space. This acceleration mechanism is now called Second-Order Fermi acceleration and will be presented hereafter, along with more modern versions.

- **Second-Order Fermi acceleration**

  The Second-Order Fermi acceleration mechanism is a stochastic mean of acceleration of high energy particles in the interstellar space. Fermi [45] proposed a simple mechanism, based on the concept that relativistic particles stochastically gain energy by reflecting on wandering magnetic clouds, moving with an average non-relativistic speed V. The clouds are associated with irregularities in the interstellar magnetic field. Physically, the energy gain is due to the electric field induced by the moving magnetized clouds[46].

  The collisions can be following or head-on, however head-on collisions are statistically more likely to occur. Thus, the process results in energy gain per collision $\langle \Delta E \rangle$, which is proportional to to the square of the speed V, thus called second-order mechanism. Mathematically:

  $$\left\langle \frac{\Delta E}{E} \right\rangle = \frac{8}{3} \left(\frac{V}{c} \right)^2 \tag{1.3.1}$$

  where c is the speed of light and E the total energy of the particle.

  The resulting spectrum is:

  $$N(E) = constant \times E^{-x} \tag{1.3.2}$$

  The spectrum is a power-law distribution, which was a very significant result. However, there are certain problems with this picture [44]: The random velocity of interstellar clouds are very small $V/c \leq 10^{-4}$, resulting in a very slow gain of energy. Moreover x should be ≈ 2.5, however there is nothing in the theory indicating why that should be the case. In a more modern version, the particles gain energy stochastically by interacting with various types of shock waves[44].

- **First-order Fermi acceleration**

  The first-order Fermi acceleration mechanism was introduced in the 1970's, as a necessity for a more effective process[44]. In this version, the only available collisions are head-on. Particles are accelerated by reflecting elastically between two approaching, massive and ideal mirrors[42]. The average energy gain after one collision is:

$$\left\langle \frac{\Delta E}{E} \right\rangle = \frac{2}{3}\frac{V}{c} \tag{1.3.3}$$

Calculations lead to:

$$N(E)dE = constant \times E^{-2}dE \tag{1.3.4}$$

Even though the above model had a few shortcomings, it managed to explain why power-law spectra with a unique spectral index are found in diverse astrophysical environments[44],[42]. The only requirement is the presence of a strong shock wave[44], as it is discussed hereafter.

- **Shock Acceleration**

A shock is a discontinuity forming when the speed of a disturbance exceeds the speed of the local signal propagation speed[47]. For example, a blast wave forms when a disturbance moves with a speed greeter than the local speed of sound. In the same sense, a shock wave forms in front of a CME when the latter exceeds the local Alfvén speed $v_A = \frac{B}{\sqrt{4\pi\rho}}$, where B is the magnetic field and ρ the plasma density.

The shock can be interpreted as an infinitely thin surface, between regions in which the usual fluid equations are valid[43]. The undisturbed medium into which the shock propagates is called *upstream*, and the disturbed medium, from where the shock has passed is called *downstream*[47]. Shocks are characterized as collisionless, when the mean free path of the particles is larger than the "width" of the shock, so that the shock behaves as a discontinuity for the particles[43].

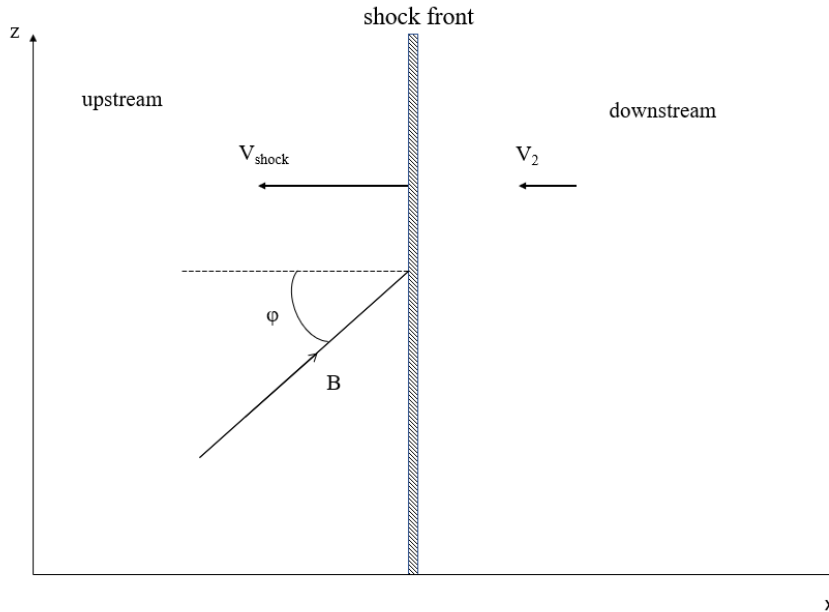**Figure 1.16:** The shock front, the reference frame where the upstream region is at rest. In general, the magnetic field $\vec{B}$ makes an angle ϕ with the shock normal.

Collisionless shocks are generally accepted as the main acceleration mechanism for energetic particles, via first-order Fermi mechanism[44]. The most prominent and also universal acceleration

mechanism is *Diffusive Shock Acceleration*: Particles are accelerated in strong collisionless shock waves and only head-on collisions can take place. The particles are reflected between the shocked and unshocked gas on both sides of the discontinuity, conforming with the original idea of the two approaching mirrors[42]. The particles are scattered by self-generated Alfv*én* or hydromagnetic waves, ensuring an isotropic particle distribution[44]. In case of quasi-perpendicular shocks, where the normal of the shock and the upstream magnetic field make a large angle and particles gain energy from the convective electric field $\vec{E} = \vec{v} \times \vec{B}$, where $\vec{v}$ is the inflow speed of the plasma and $\vec{B}$ the upstream magnetic field in the rest frame of the shock, a process often called *shock-drift acceleration*[42]. Depending on the energy and pitch angle, the energy gained from the drift along electric field can be such that the particle may escape[33].

1.3.2.2   Acceleration of SEPs

The standard scenarios proposed to explain SEP acceleration include shock acceleration and acceleration of particles in solar flares. Interplanetary shock waves driven by fast CMEs, or other IP other structures, such as CIRs, can accelerate particles via the mechanisms explained in the previous paragraph. On the other hand, particles are accelerated in solar flares, primarily during magnetic reconnection, confirmed by the hard X-ray, gamma-ray and microwave signatures during the impulsive flare phase[33]. More specifically, it is proposed that, after the triggering of the flare (see subsubsection 1.2.3), energy is released primarily in an X-geometry reconnection site above the flare loops. The DC electric fields generated at the reconnection region are responsible for the acceleration of energetic particles at the *acceleration region* below the reconnection site. These electric fields ($\sim 10^3$ V/m) can accelerate electrons up to 100KeV[8].

The above distinction however is a simplification, as in practice as the overall phenomenon is intrinsically complex[33]. Magnetic reconnection is not limited in solar flares, as it can also occur between the CME and ambient magnetic field or in the downstream region, where current sheets may form[33]. To make matters more complicated, shock acceleration can also occur at the reconnection regions[48]. Particles can be also accelerated stochastically by plasma waves and turbulence in magnetic reconnection regions[33].

1.3.2.3   Energy Spectrum

The study of the energy distribution of SEPs is crucial to the formulation of a complete acceleration model. In the low energy region the spectrum can be described adequately by a power law N(E)=$const \times$ E$^{-\gamma}$, or an exponential function N(E)=$const \times$ e$^{-\frac{E}{E_0}}$, where E$_0$ the characteristic energy of the spectrum. γ is the spectral index. However, the most energetic events, such as GLEs, exhibit a rapid steepening of the spectrum in the range of high energies, called spectral knee [1]. This behavior is usually modeled as a combination of various equations[49].

Ellison and Ramaty (E-R) [50] compared the simultaneous first-order Fermi shock acceleration of electrons, protons, and alpha particles to observations of SEP events. They found that first-order Fermi shock acceleration can adequately model many solar flare energetic particle events and a shock

with compression ratio $\sim$ 1.6–3.0 that simultaneously produces electron, proton, and alpha-particle spectra close to observations. Moreover, they suggested that the steepness of the spectrum is caused by shock-accelerated particles escaping the shock region. The resulting power-law-times-exponential spectrum is N(E)=$const \times$ E$^{-\gamma} \times$ e$^{-\frac{E}{E_c}}$, where E$_c$ is the cut-off energy.
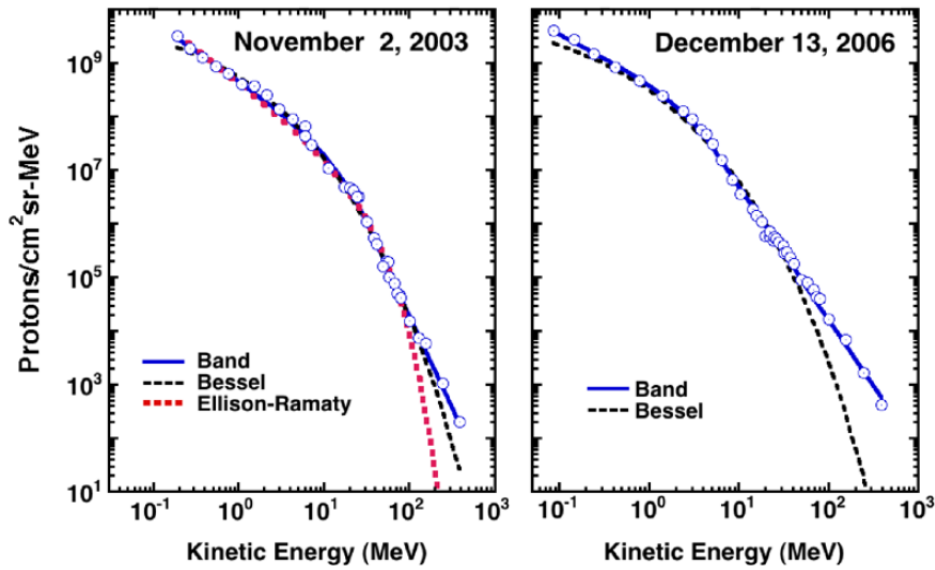
Figure 1.17: Examples of fluence spectra, adopted by Mewald et al. [31], with fitted spectral functions. The spectral knees are evident in both panels

The spectrum of protons in major SEP events may span 4-5 orders of magnitude in energy: from 1 MeV to several GeV. Only a small part of the spectrum can be usually studied, as the proton spectra are obtained from a single type of detector, that has a narrow energy range: spacecraft data (<500 MeV), stratospheric balloons (hundreds of MeV), or ground level observations (>500 MeV) [3]. Novel studies include data over a wide range of energies, such as [51], who found that the SEP spectra are well fitted by the above power-law modulated by an exponential cutoff attributed to particles escaping the shock region during diffusive shock acceleration. On the other hand, Mewald et al. [31], found that 16 GLEs were better fitted by the double power law of Band et al. [52]: the spectrum is described by a power-law continuum with an exponential cut-off at low energies N(E)= $const \times$ E$^{\alpha} \times e^{-\frac{E}{Ec}}$ and by a steeper power at high energies N(E)=$const \times$ E$^{\beta}$. A combined spectral fit of the E-R and Band functions was used by [53]. Other models include the fitting of Bessel functions, including the acceleration efficiency and escape time from the acceleration region, introduced by Ramaty [54].

It should be emphasized that, there is a significant distinction between the mathematical formulations, which describe the energy spectrum at the source, and the observed spectrum at the Earth. In several cases, the observed spectrum at the Earth is the combination of several theoretical formulas and the spectral parameters vary significantly from event to event. This complexity reflects the fact that, the interplanetary conditions have a significant effect on the particle energies and intensities, modifying the spectrum. In reality, the construction of the spectrum at the source is very difficult and only energies >500MeV may approximate the source spectrum [49]. The models used are not adequate to reconstruct the source spectrum based on observations, as they do not include the effect interplanetary

conditions[3]. These uncertainties can be minimized by considering events magnetically well-connected to the Earth and constructing the spectra at time of maximum intensity[55].

1.3.3   The effect of interplanetary conditions

The various conditions present in the interplanetary medium have an impact on the propagation of SEPs, altering their path, timing and intensities. Such conditions are the existence of suprathermal remnants of previous SEP events, as well as interplanetary structures such as shocks and ICMEs.

1.3.3.1   Transport

Energetic particles are guided by the IMF from the source region to the interplanetary space. However, particles can be observed at a very wide range of longitudes, deviating from the expected western-longitudes profile (see paragraph 1.3.1.5). The transport of particles in the interplanetary space, after their release from the Sun, has been thoroughly studied and is an important factor determining the profile of SEPs.

According to [33], the IMF can be described as a Parker spiral, superimposed by transient structures such as shocks, ICMEs, and turbulence, which leads to scattering of particles and meandering of the magnetic field lines. Particles also experience drifts due to inhomogeneity and induced electric fields in the IMF. One factor that lead to broad longitudinal distributions is the presence of open magnetic field lines originating from active regions. Although they can explain simple electron events detected even 50° away from the Parker spiral related to the parent solar activity, they fail to explain very broad longitudinal spreads. Moreover, interaction of particles with turbulence, due to the passage of an ICME, shock etc, can produce scattering and deceleration along the nominal Parker spiral, as well as propagation across the magnetic field, during which particles drift away from their nominal Parker spiral.

1.3.3.2   Effect on SEP intensities

As mentioned in 1.3.1.4, the dominant factors determining the SEP event intensities are the characteristics of the source flare and driver-CME. However, other factors can also affect the observed SEP intensity: the Alfvén speed distribution in the ambient solar wind[38], the presence of a preceding CME in space[56], the SEP intensity background from previous events[57]. It has also been reported that, SEP intensities tend to be diminished, when a coronal hole is present between the line connecting the Sun with the observer and the solar source of the SEP event. Generally, the presence of coronal holes near the eruption region, as they can deflect the CME and change the magnetic connectivity, having a positive or negative effect [38].

Many studies have shown that the presence of an ICME beyond the observer at the time of the SEP detection can lead to enhanced particles intensities[58]. The presence of a preceding ICME provide propitious conditions for the acceleration and enhanced particle intensities: the turbulence enhancement and the suprathermal seed population are two factors contributing to the observations of higher

SEP intensities [59]. Moreover, the magnetic configuration of the ICME can reflect particles back to the observer, contributing to the enhanced intensities [60].

In case the ICME is located between the observer and the Sun, the particles travel in the disturbed interplanetary medium caused by the ICME. The magnetic compression and turbulence created by the ICME The turbulence may act as a barrier, resulting in both the delay and intensity drop of the particles [60],[61]. If the ICME is rooted to the Sun, particles can be quasi-trapped and reflect back and forth between the magnetic mirrors[62]. This scenario can lead to enhanced particle intensities, if the observer intercepts such a structure [58].

Many studies have shown that, particle intensities can be affected by the magnetic cloud (MC) configuration of the ICME. [61] showed that, the converging magnetic field reflects part of the particles, altering the observed intensity. The MC acts as a barrier, that only a few particles can propagate through. As a result, the particle intensity is different between the upstream and downstream regions. An MC ahead of the particles can act as a barrier, leading to attenuated particle intensities.

2 DATA & CLASSIFICATION

2.1 Data selection

In this section, the compilation of the 98 SEP events catalogue and list of associated ICMEs is explained. The events are then classified, depending on the relative position of one or more ICMEs and the observer at the time of the peak proton intensity.

2.1.1 Original SEP database and event selection

The SEP events used are acquired from the *Advanced Solar Particle Event Casting System* database (ASPECS), which was developed on the methodology as outlined in [63] and consists of solar flare events from 1984 to 2013. These solar flare events are further associated with CMEs and SEP events. For this study, solar flares that *are associated with SEP events* are selected, limited to solar longitudes $\in[10^o,110^o]$, in order to ensure good magnetic connectivity. Lastly, all events that occur prior to 1996[8] are excluded, so that all events can be associated with the ICME database (see following section 2.1.3).

The above selection results to a list that contains **98 SEP events**, dating from 1997 to 2012. Each event is assigned with a unique key-number 1-98 and associated with a solar flare and/or a CME. The specific characteristics/information are shown in table 2.1. It should be noted that, the linear speed of the CME is originally derived by the LASCO catalog: https://cdaw.gsfc.nasa.gov/CME_list/, where is calculated via linear fit of height-time measurements, projected onto the plane of sky. All dates are given with 1 minute accuracy. For details, see [63].

Flare	CME
1. start date (UT)	1. date observed by LASCO (UT)
2. date of maximum flux (UT)	2. linear speed (km/s)
3. end date (UT)	3. width (degrees)
4. solar longitude (degrees)	
5. CMX class	
6. X-ray intensity (W/m^2)	
7. SXR fluence (J/m^2)	

Table 2.1: Flare and CME characteristics included in the SEP database

Figure 2.1 displays the distributions of the main characteristics concerning the sources of the SEP events. The CME speed follows a Gaussian like distribution with a mean value $\sim$ 1400 km/s (the black dashed line on figure 2.1a). Roughly $\sim$90% of all events have a speed from 500km/s up to 2500 km/s. Most CMEs are halo (figure 2.1b), with a smaller peak at 180 degrees. Moreover, 82 (84%) are associated with a CME and 16 (16%) not associated with a CME (figure 2.1c). It should be noted that, the lack of a

---

[8]the year that continuous CME observations were made possible via SOHO

CME-flare association does not necessarily indicate that the event is not related with a CME, but possibly that the associated CME can not be identified. Furthermore, 22 events (22%) are associated with C class flares, 46 (47%) with M class and 30 (31%) with X class (figure 2.1d). Lastly, the events are scattered in all longitudes in the selected interval, with no clear peak (figure 2.1e).
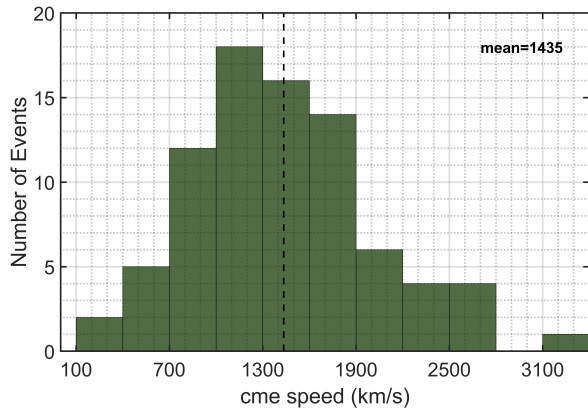
(a) CME speed distribution
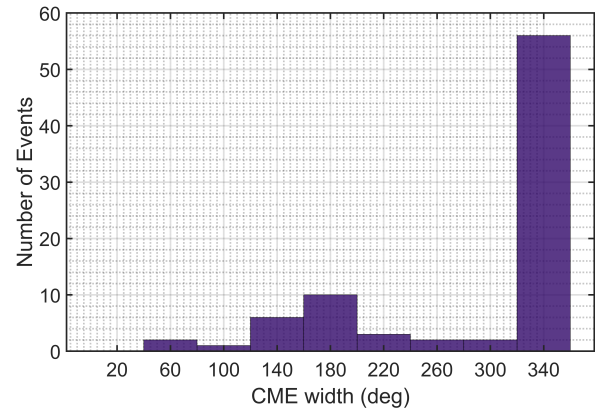
(b) CME width distribution
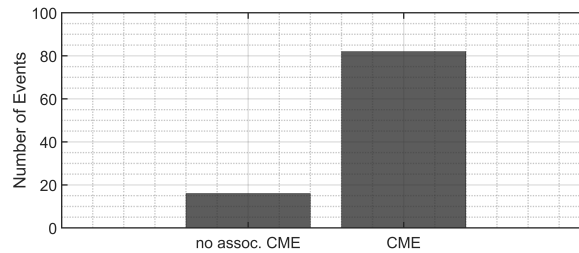
(c) Association with CME
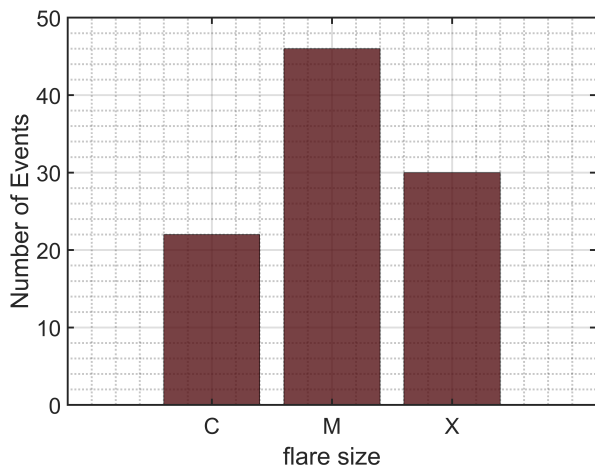
(d) Flare class distribution
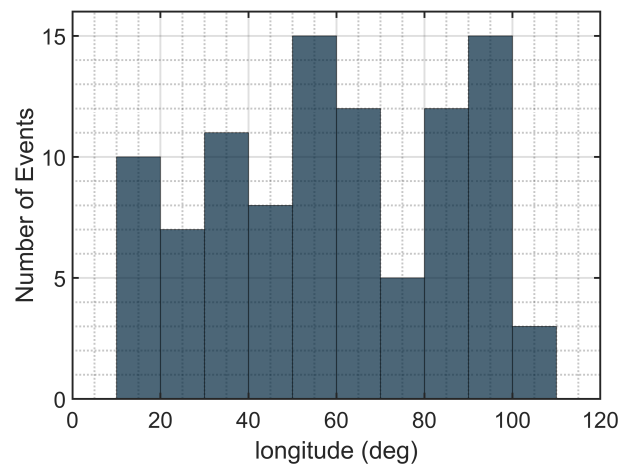
(e) Longitudinal distribution

Figure 2.1: Statistics of SEP events list

2.1.2   In-Situ Measurements

The in-situ measurements of the solar wind parameters and proton intensities employed in this study are the following:

In-Situ Measurements
1. IMF magnitude (nT)
2. IMF components B_x, B_y and B_z (nT, GSE coordinates)
3. Solar wind speed (km/s)
4. Integral proton intensities E>10 MeV, E>30 MeV, E>50 MeV, E>60 MeV and E>100MeV.

Table 2.2: List of the In-Situ Measurement Data

The IMF (table 2.2: 1,2) and solar wind measurements (table 2.2: 3), as well as the integral proton intensities (table 2.2: 4) in the energy channels E>10, E>30, E>60 MeV are obtained from https://omniweb.gsfc.nasa.gov/ow_min.html. The integral proton intensities for (table 2.2: 4) E>50 and E>100 MeV are taken from http://www.staff.oma.be. All data have a 5 minute resolution. The solar wind magnetic field and plasma data are measured by s/c ACE (Advanced Composition Explorer) [9] and Wind [10], both in halo orbits around L1. The proton intensities are obtained by the geosychronous s/c GOES[11]. The solar wind magnetic field and plasma data are time shifted to the bow shock nose of the magnetosphere and the ACE data are also shifted to the position of Wind. GOES data are not shifted [12].

For each event the peak proton intensity and its timestamp at each energy channel are calculated and added to the SEP database. In case we do not observe enhancement in an energy channel, the value of the corresponding peak proton intensity is '*9*' and its timestamp '*NaT*'.

2.1.3   ICME and IP Shock Lists

The second database constructed for this study consists of a total of 116 unique records of ICMEs. Each ICME is observed within a 72 hours interval before and after the peak proton intensity of one or more SEP events. The ICME data are acquired from the list compiled by I.Richardson and H.Cane (R/C) (http://www.srl.caltech.edu/ACE/ASC/DATA/level3/icmetable2.html#(l)), containing records since 1996.

The data obtained from the R/C list are shown in table 2.3. These are, from top to bottom: the date of the associated disturbance (table 2.3: 1), i.e. the shock driven by the ICME (typically coinciding with the associated geomagnetic storm), the start (table 2.3: 2) and end (table 2.3: 3) dates of the ICME, based on plasma and magnetic field observations. Moreover, the average ICME speed (table 2.3: 4), based on solar wind speed observations during the passage of the ICME (start-to-end) and the date that the probably associated CME was observed by LASCO (table 2.3: 5). Furthermore, each ICME is associated with an index (table 2.3: 6) 0,1 or 2, concerning whether it is associated with a magnetic cloud (MC):

---

[9] http://www.srl.caltech.edu/ACE/ace_mission.html
[10] https://wind.nasa.gov
[11] https://www.nasa.gov/content/goes-overview/index.html
[12] https://omniweb.gsfc.nasa.gov/html/HROdocum.html

'2' indicates that the ICME meets the criteria of an MC and '1' that, although there is a rotation in field direction, other characteristics of an MC are not observed. '0' means that the ICME lacks most important characteristics of an MC. Lastly, the start (table 2.3: 7) and end dates (table 2.3: 8) of the MC are given. All dates are approximated to the nearest hour.

Additionally, each ICME is assigned with a number 1-98, corresponding to the key-number of the associated SEP event. An ICME can be associated with more than one SEP events, since during its passage multiple events can occur. Moreover, An ICME that its LASCO CME coincides with the CME that drives a SEP event (*driver* or *primary* CME hereafter), is labeled as 'DRIVER'. All ICMEs that are not counterparts of the driver CME are labeled as 'INT'. The complete list can be found at the end of the section (table 2.5).

A list of interplanetary (IP) shocks, that are observed within the 72-hours interval, is also compiled. The original source is http://ipshocks.fi/database.

ICMEs
1. disturbance date (UT)
2. start date (UT)
3. end date (UT)
4. average ICME speed (km/s)
5. date of associated LASCO CME (UT)
6. MC index ('2','1' or '0' [2])
7. MC start date (UT)
8. MC end date (UT)

Table 2.3: ICME parameters obtained by the R/C list

2.2   Classification of Events and Final Database

The events are categorized to to 6 main classes, based on the position of one or more associated ICMEs at the time of the maximum proton intensity. An ICME that is the interplanetary counterpart of the CME that generates the SEP event (labeled as 'DRIVER' in the ICME database, see subsubsection 2.1.3, table 2.5) is excluded from the classification process. The classification scheme is adopted from Lario et al. [60] and schematically represented in figure 2.2. The 6 classes are the following:

- **Class 0** are the events that occur within the standard solar wind and ICMEs are not present within a 3 days interval (figure 2.4a).
- **Class 1** are the events that are followed by an ICME within the next 72 hours. At the time of the peak proton intensity, the ICME is located between the Sun and the observer (figure 2.4b).
- Events that their proton intensity reach its maximum at the time that the s/c is within the sheath region between the ICME and the proceeding shock are **Class 2** (figure 2.4c).
- Events that, at the time of the peak proton intensity, Earth is immersed within an ICME, are classified as **Class 3** (figure 2.4d).
- **Class 4** are these events that occur after the passage of an ICME up to 3 days prior. At the time of the maximum proton intensity, the ICME is located beyond the observer (figure 2.3e).
- Lastly, in case multiple ICMEs are detected before and after the peak intensity, the event is classified to **Class 5** (figure 2.3f). In case the event is immersed within an ICME or in the sheath region of an ICME, but other ICMEs are detected before and/or after the peak intensity, the event is classified

(a) Class 0   **(b)** Class 1   **(c)** Class 2   **(d)** Class 3   **(e)** Class 4
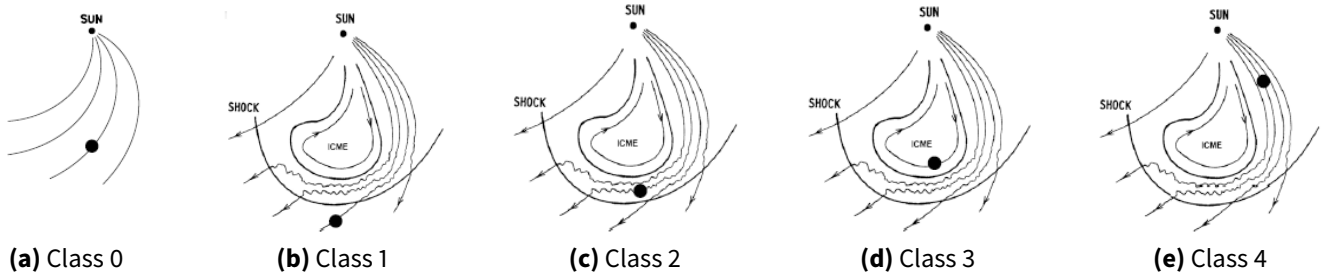
Figure 2.2: Schematic representation of the IP environment for classes 0-4 (class 5 is not shown). All figures are adapted from Lario et al. [60].

as class 3 or class 2 correspondingly.

The above classification is applied to each energy channel, thus each event is given 5 numbers, ranging from 0-5. If there is no flux enhancement in an energy channel, the corresponding class is labeled as '9'. An overall classification of each event is also applied, regardless of the energy channel. For most of the events (95%), the same class applies to all energy channels and the overall class is the same. The rest of the events occur near the passage of an ICME and protons of different energies peak at different sides of the ICME. For those events, the same class does not apply for all energy channels and the overall category is selected carefully. In conclusion, each event is labeled with 6 numbers: the class category concerning the event for all energy channels (overall) and the class of each energy channel.

$$\underbrace{\_\#\_}_{Overall} - - \underbrace{\_\#\_}_{>10MeV} , \underbrace{\_\#\_}_{>30MeV} , \underbrace{\_\#\_}_{>50MeV} , \underbrace{\_\#\_}_{>60MeV} , \underbrace{\_\#\_}_{>100MeV}$$

An secondary classification is applied for Class 3 events, in order to investigate the effect of MCs. We divide the events into two subcategories, based on the classification originally performed by Richardson-Cane (see subsubsection 2.1.3). Class 3 events that are observed within ICMEs with a definite MC structure ('2' on the R-C list), are labeled as *'MC'*. Events that are observed within ICMEs that do not have all MC characteristics ('1') or non ('0') are merged into one sub-category, named *'Possible/No MC'* (Pos/NoMC hereafter). This distinction is valid, as MCs are defined by all three characteristics (paragraph 1.2.4.3). Moreover, we avoid low statistical samples, as ICMEs without any MC characteristics ('0') are a very small fraction of the total number of class events (5/30). Of course, it should be expected that, Pos/NoMC subcategory is not homogeneous, as it contains a variety of possible magnetic structures.

The distribution of the classes for all events and per energy channel is shown in figure 2.3. The percentage distribution per event class (regardless of energy channel, top left panel of 2.3a) is: Class 0: 26%, Class 1: 8%, Class 2: 8%, Class 3: 31%, Class 4: 17%, Class 5: 10% out of all 98 events. For the Class 3 sub-categories: MC: 47%, Possible/no MC: 53% out of all Class 3 events. 4% of the 98 events exhibit flux enhancements only in the E>10MeV energy channel and 15 % in the E>10MeV and E>30MeV energy channels. 20% of all events do not exhibit flux enhancement in the E>60MeV and E>100 MeV energy channels, while 38% in all channels except E>100MeV. Most of the above cases are events classified as class 0 and class 2. Lastly, the percentage of Pos/NoMC events is smaller than the corresponding one of MC events for the E>60MeV and E>100MeV energy channels.

Figure 2.4 presents an example for each event class. From top to bottom, the following physical parameters are graphically illustrated:

- ▶ IMF strength (nT)
- ▶ solar wind speed (km/s)
- ▶ Integral proton intensities E>10 MeV, E>30 MeV, E>50 MeV, E>60 MeV and E>100 MeV (1p/cm^2/s/sr = 1 pfu, the peak at energy channel is shown as '$*$').
- ▶ azimuth angle $\phi = arctan(B_y/B_x)$ (GSE)
- ▶ elevation angle $\theta = arctan(B_z/\sqrt{B_x^2 + B_y^2})$ (GSE)

Each subplot contains the following information: The flare onset as a vertical yellow line. The associated CME onset is printed as a dashed line near the flare line. The exact dates are displayed on the title. The title also contains the flare class (C, M, X), the event classification per energy channel and overall, and the event unique number. The gray boxes and and the blue vertical lines indicate the passage of the ICME and the associated disturbance at the times they pass from the spacecraft (s/c), correspondingly. The dashed purple lines indicate the onset at the Sun (vertical) and propagation (horizontal) of the ICME. The pink boxes within the ICME-boxes in figure 2.4d are MCs. The white box in figure 2.4a shows the passage of the ICME counterpart of the driver CME from the s/c. The red vertical lines represent the passage of an IP shock. Lastly, on the right of each figure, the exact peak proton intensity per energy channel and the corresponding date are printed.
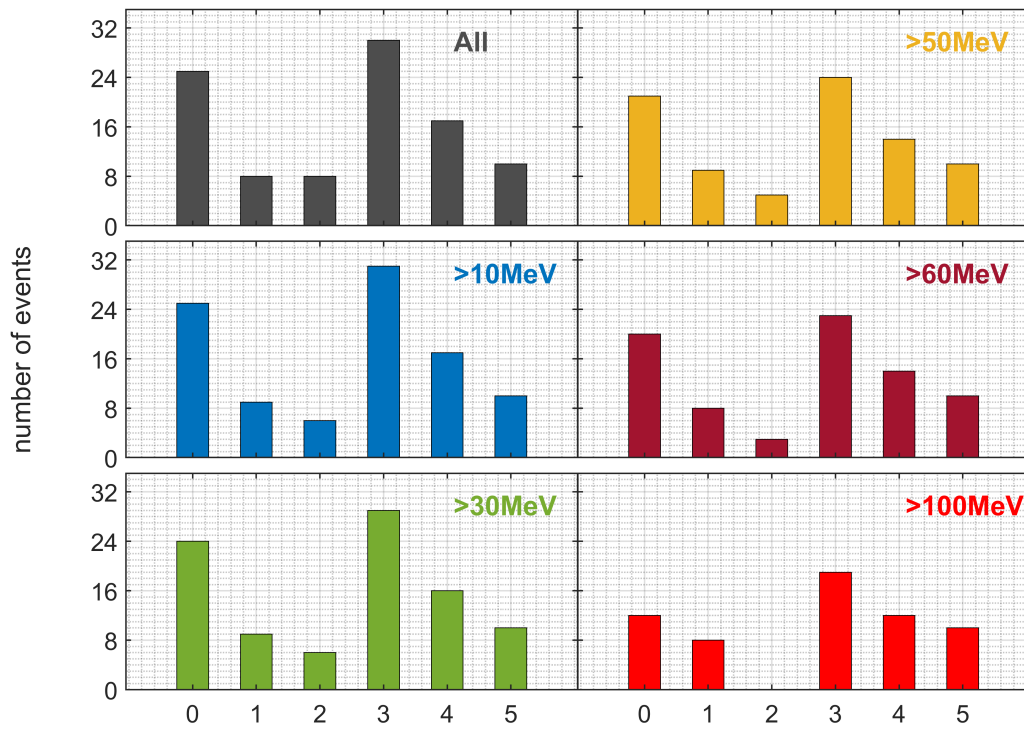
(a) Primary Classification
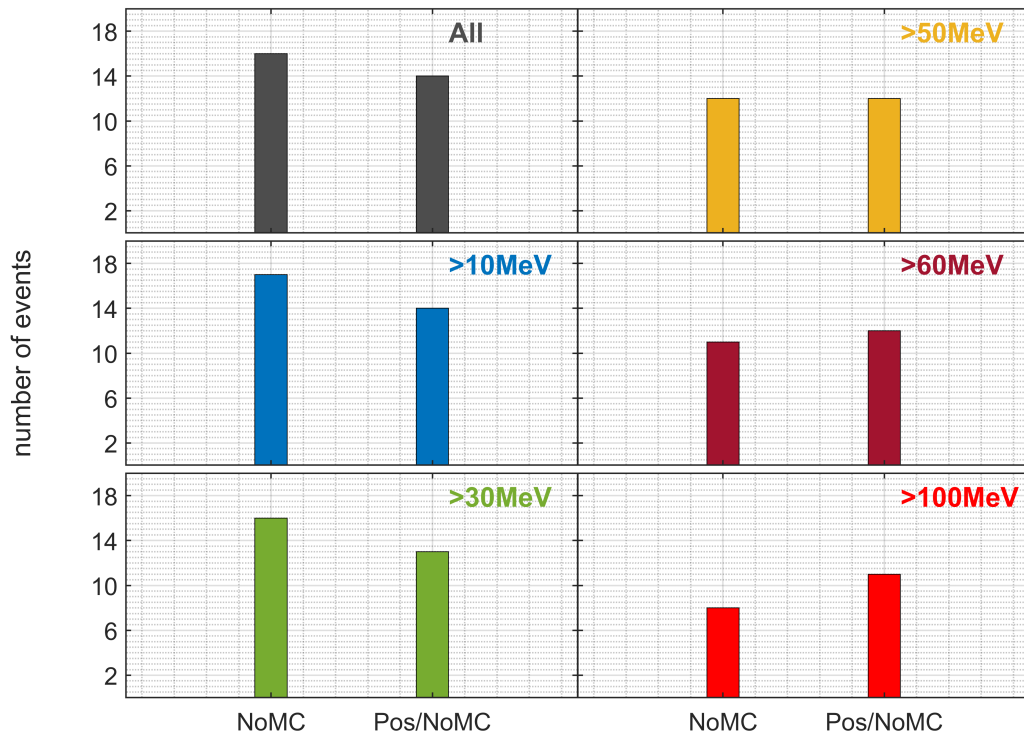
(b) Class 3 Sub-Categories

Figure 2.3: Distribution of Classes

Figure 2.4: Examples for each event category. See text for more details

(a) Class 0

flare: 04/11/1997 05:52 (X) - CME: 04/11/1997 06:10 - CAT: 0--0-0-0-0-0 - event 1

(b) Class 1

flare: 01/06/1999 16:27 (C) - CAT: 1--1-1-1-1-1 - event 11
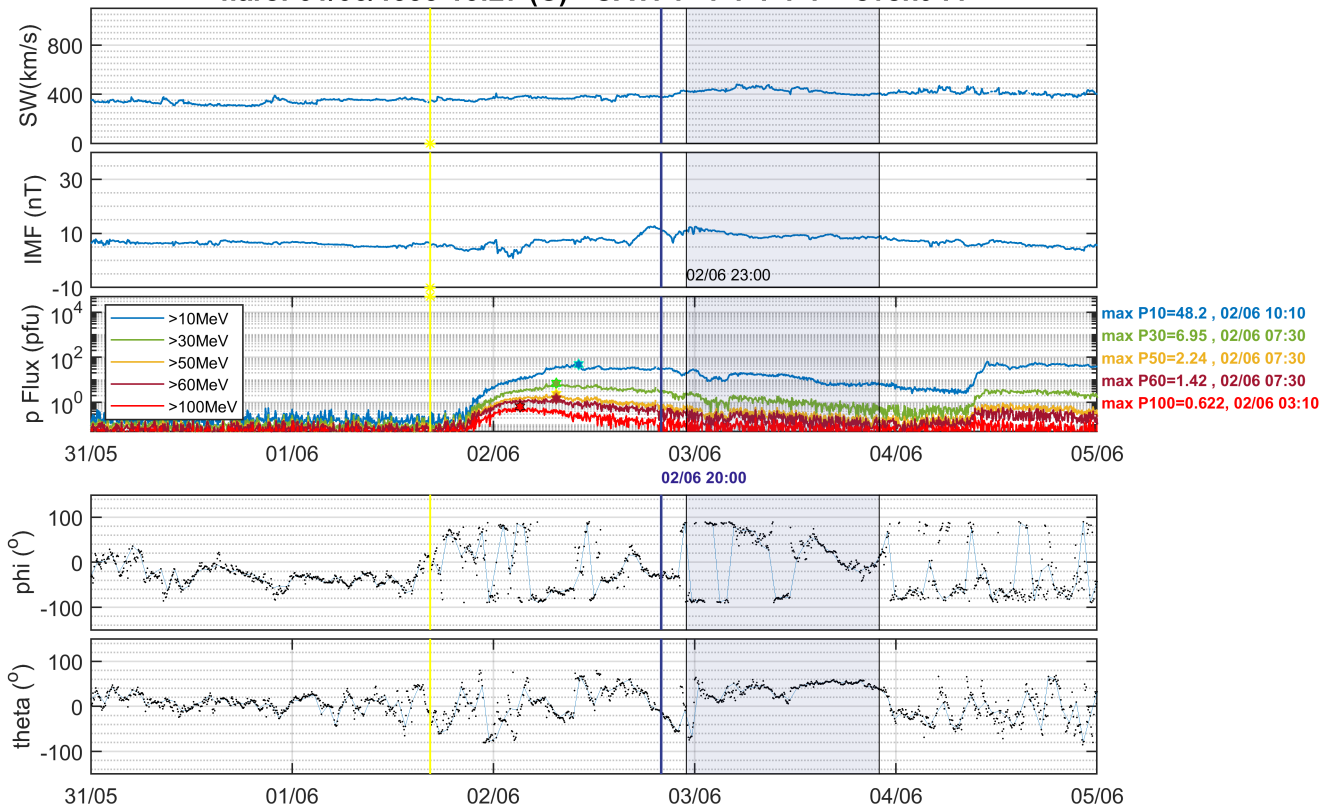
flare: 18/08/2002 21:12 (M) - CME: 18/08/2002 21:54 - CAT: 2--2-2-2-9-9- MC: 1 - event 48

(c) Class 2

flare: 21/04/2002 00:43 (X) - CME: 21/04/2002 01:27 - CAT: 3--3-3-3-3-3- MC: 2 - event 44

(d) Class 3

(e) Class 4

(f) Class 5

Table 2.4: SEP events list

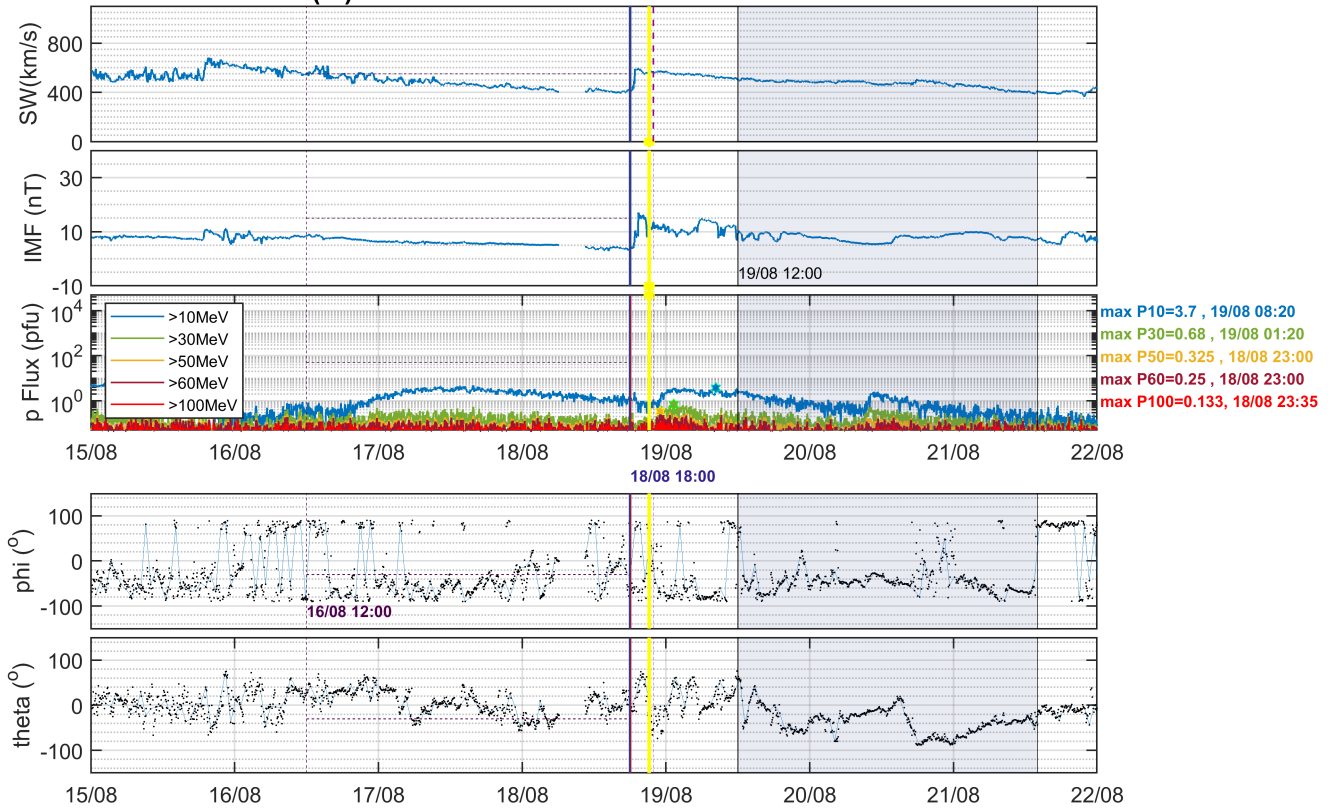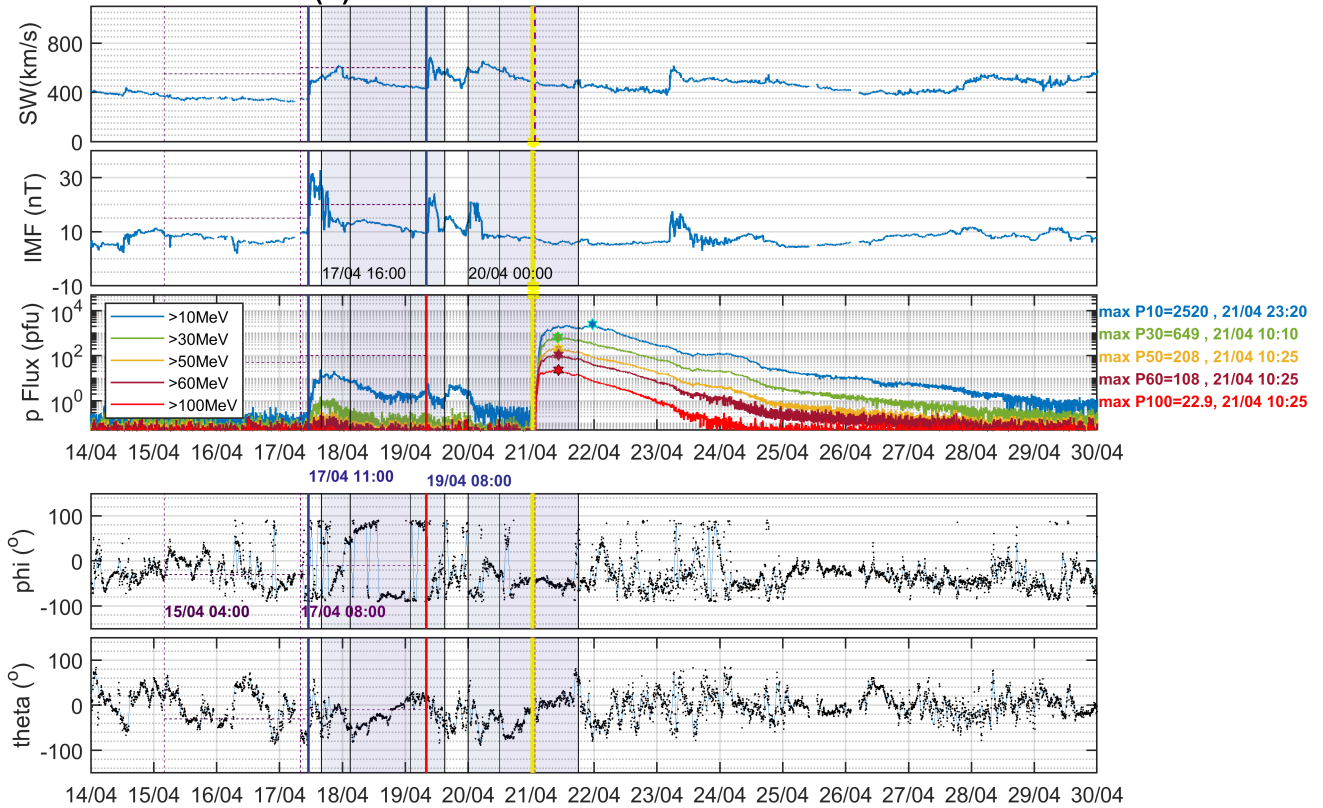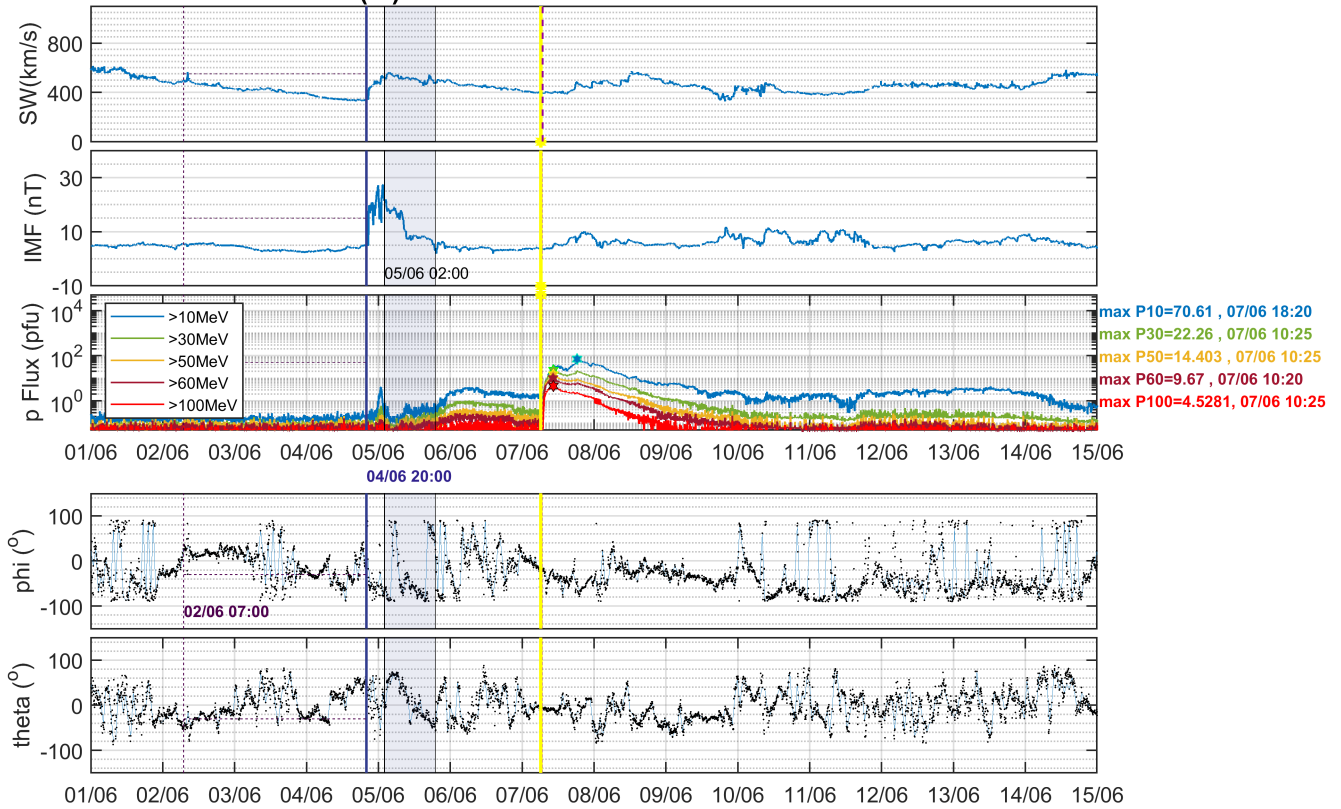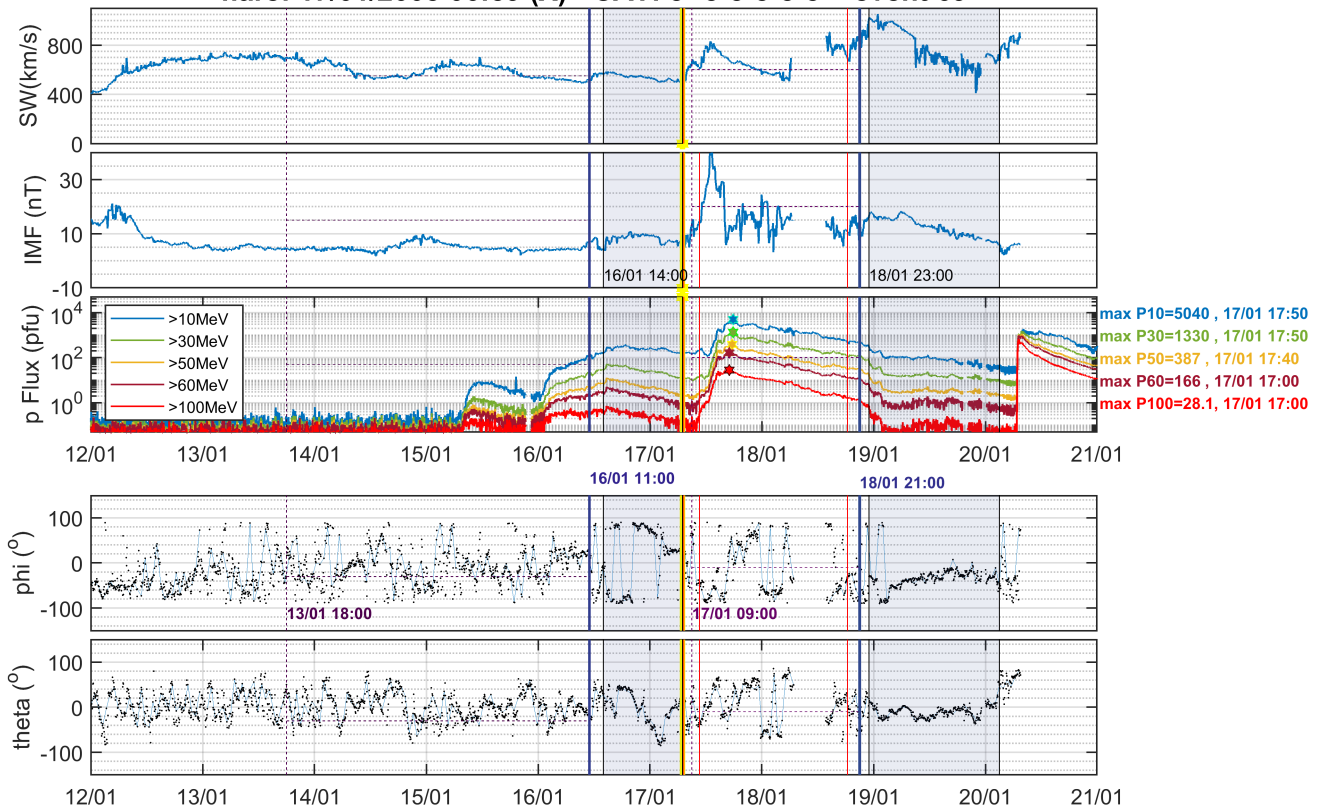| INDEX	FLARE ONSET[1]	SXR FLUX[2]	SXR FLUENCE[3]	LONGITUDE	CME DATE[4]	CME SPEED	CME WIDTH	CLASS[5]	PEAK 10MeV	PEAK 30MeV	PEAK 50MeV	PEAK 60MeV	PEAK 100MeV[4]	PEAK FLUX[6]
1	97-Nov-04/05:52	X2.1	0.0506	33	04/06:10	785	360	0-0-0-0-0	04/13:00	04/09:20	04/09:20	04/09:20	04/09:20	67.1,20.3,9.98,6.93,2.55
2	97-Nov-06/11:49	X9.4	0.337	63	06/12:10	1556	360	2-2-1-1-1	07/03:00	06/21:15	06/18:25	06/18:20	06/17:10	532,189,115,92,46.3
3	98-Apr-20/09:38	M1.4	0.0731	90	20/10:07	1863	243	0-0-0-0-0	21/11:45	21/11:00	21/13:25	21/13:25	21/13:45	1610,384,103,44.7,7.13
4	98-May-02/13:31	X1.1	0.0621	15	02/14:06	938	360	3-3-3-3-3	02/16:55	02/15:20	02/15:20	02/15:20	02/15:20	149,48,24.3,19.4,9.66
5	98-May-06/07:58	X2.7	0.202	65	06/08:29	1099	190	4-4-4-4-4	06/09:45	06/09:05	06/08:55	06/08:50	06/08:40	239,47.5,19.3,12.7,4.89
6	98-May-09/03:04	M7.7	0.104	86	09/03:35	2331	178	4-4-4-4-4	09/10:20	09/16:50	09/16:50	09/16:50	09/13:05	12.3,1.9,0.764,0.5,0.22
7	98-Jun-16/18:03	M1	0.045	103	16/18:27	1484	281	0-0-0-0-0	18/03:35	17/07:45	NaT	NaT	NaT	2.21,0.57,NaN,NaN,NaN
8	98-Sep-30/13:04	M3	NaN	81	NaT	NaN	NaN	0-0-0-0-0	01/00:25	30/19:55	30/19:55	30/19:20	30/19:20	1160,133,30.3,14,2.98
9	98-Nov-05/19:00	M8.4	0.11	18	05/20:44	1118	360	2-1-2-9-9	06/13:05	07/13:15	NaT	NaT	NaT	9.55,0.79,NaN,NaN,NaN
10	99-May-27/11:06	C1	NaN	90	NaT	NaN	NaN	0-0-0-0-0	27/14:10	27/14:05	27/12:15	27/12:15	27/12:15	9.02,1.65,0.553,0.41,0.177
11	99-Jun-01/16:27	C1.3	0.00144	90	NaT	NaN	NaN	1-1-1-1-1	02/10:10	02/07:30	02/07:30	02/07:30	02/03:10	48.2,6.95,2.24,1.42,0.622
12	99-Jun-04/06:52	M3.9	0.023	69	04/07:26	2230	150	4-4-4-4-9	04/10:55	04/10:40	04/12:45	04/12:45	NaT	64,3.7,0.929,0.6,NaN
13	00-Feb-18/09:21	C1.1	0.00107	78	NaT	NaN	NaN	5-5-5-5-5	18/12:15	18/10:40	18/10:15	18/10:15	18/09:55	13,2.95,1.26,0.91,0.374
14	00-Apr-04/15:12	C9.7	0.0325	66	04/16:32	1188	360	0-0-0-0-9	05/09:30	04/20:35	04/20:35	04/20:05	04/20:05	55.8,0.99,0.321,0.23,NaN
15	00-May-15/15:46	C7.8	0.0125	67	NaT	NaN	NaN	3-3-9-9-9	16/01:25	16/02:30	NaT	NaT	NaT	1.86,0.3,NaN,NaN,NaN
16	00-Jun-10/16:40	M5.2	0.0726	38	10/17:08	1108	360	5-5-5-5-5	10/20:45	10/18:15	10/18:10	10/18:10	10/17:55	46,12.8,6.25,4.34,1.62
17	00-Jun-25/07:17	M1.9	0.0431	55	25/07:54	1617	165	2-2-2-9-9	26/01:30	26/01:10	NaT	NaT	NaT	4.57,0.36,NaN,NaN,NaN
18	00-Jul-22/11:17	M3.7	0.0697	56	22/14:30	141	49	3-3-9-9-9	22/14:05	22/13:30	22/13:10	22/12:50	22/12:50	17.6,4.22,1.57,0.99,0.343
19	00-Aug-12/13:48	C3.2	0.0294	46	12/14:54	876	161	3-3-9-9-9	13/06:35	NaT	NaT	NaT	NaT	4.92,NaN,NaN,NaN,NaN
20	00-Oct-16/06:40	M2.5	0.0943	90	16/07:27	1336	360	4-4-4-4-4	16/18:40	16/10:00	16/10:05	16/09:55	16/09:55	15.1,3.58,1.44,0.91,0.302
21	00-Oct-25/08:45	C4	0.065	66	25/08:26	770	360	0-0-0-0-9	26/03:40	25/19:10	25/19:10	25/18:30	NaT	15.4,1.11,0.35,0.25,NaN
22	00-Nov-08/22:42	M7.4	0.292	77	08/23:06	1738	170	3-3-3-3-3	09/15:55	09/06:35	09/03:40	09/03:40	09/03:40	14800,4440,1880,1190,349
23	01-Jan-28/15:40	M1.5	0.0297	59	28/15:54	916	360	4-4-4-4-4	29/06:55	28/21:00	28/21:05	28/20:40	28/20:40	48.9,6.03,1.89,1.08,0.3
24	01-Mar-29/09:57	X1.7	0.222	19	29/10:26	942	360	3-3-3-3-3	30/06:10	29/22:15	29/20:55	29/20:55	29/15:20	35.4,3.93,1.15,0.72,0.213
25	01-Apr-02/21:32	X20	1.48	78	02/22:06	2505	244	3-3-3-3-3	03/07:45	03/07:45	03/07:45	03/07:45	03/07:40	1110,217,53.5,26.2,5.42
26	01-Apr-12/09:39	X2	0.295	43	12/10:31	1184	360	3-3-3-3-3	12/18:00	12/17:50	12/17:50	12/17:50	12/17:25	50.5,13.9,5.75,3.95,1.49
27	01-Apr-15/13:19	X14.4	0.593	85	15/14:06	1199	167	3-3-5-5-5	15/19:20	15/16:25	15/15:40	15/15:40	15/15:25	951,357,275,242,146
28	01-Apr-26/11:26	M7.8	0.0909	31	26/12:30	1006	360	0-0-0-9-9	28/05:00	28/02:15	NaT	NaT	NaT	57.5,0.5,NaN,NaN,NaN
29	01-May-07/11:36	C3.9	0.0135	35	07/12:06	1223	205	2-3-3-2-9	08/07:55	07/21:15	07/18:05	07/18:05	07/18:05	30,1.44,0.48,0.37,NaN
30	01-May-20/06:00	M6.4	0.0113	90	20/06:26	546	179	2-3-2-2-9	20/14:10	20/11:30	20/11:30	20/09:10	20/09:10	9.16,2.85,1.52,1.25,0.67
31	01-Jun-15/15:30	C1	NaN	100	NaT	NaN	NaN	0-0-0-0-0	16/00:05	15/17:35	15/17:30	15/17:30	15/17:15	26.8,4.45,1.7,1.04,0.3
32	01-Aug-09/10:20	C1	NaN	10	NaT	NaN	NaN	0-0-0-9-9	10/11:55	10/08:50	NaT	NaT	NaT	17,0.79,NaN,NaN,NaN
33	01-Aug-21/10:35	C2.7	0.0389	59	21/12:06	623	128	4-9-9-9-9	21/16:05	21/16:05	NaT	NaT	NaT	5.13,NaN,NaN,NaN,NaN
34	01-Oct-01/04:41	M9.1	NaN	91	01/05:30	1405	360	3-3-3-3-3	02/08:10	02/08:05	02/08:45	02/08:35	01/18:05	2360,193,24.5,4.63,0.22
35	01-Oct-19/16:13	X1.6	0.153	29	19/16:50	901	360	0-0-0-0-0	19/22:30	19/19:20	19/18:55	19/18:35	19/20:05	11.7,2.59,1.03,0.68,0.292
36	01-Oct-25/14:42	X1.3	0.229	21	25/15:26	1092	360	5-5-9-9-9	25/18:55	NaT	NaT	NaT	NaT	2.07,NaN,NaN,NaN,NaN
37	01-Nov-04/16:03	X1	0.29	18	04/16:35	1810	360	3-3-3-3-3	06/02:15	06/02:20	06/02:20	06/02:20	06/02:20	31700,6870,2120,1120,253
38	01-Nov-22/20:18	M3.8	0.0506	67	22/20:30	1443	360	5-5-5-5-5	24/05:55	24/05:55	23/12:25	24/05:15	24/02:25	18900,1180,162,48.6,4.65
39	01-Dec-26/04:32	M7.1	0.495	54	26/05:30	1446	212	1-1-1-1-1	26/11:15	26/07:35	26/07:30	26/07:30	26/07:20	780,331,180,130,50.2
40	02-Jan-14/05:29	M4.4	0.437	90	14/05:35	1492	360	0-0-0-0-9	15/20:00	15/11:15	15/11:15	15/11:00	NaT	15.4,1.69,0.53,0.35,NaN
41	02-Mar-18/02:16	M1	0.0452	46	18/02:54	989	360	3-3-2-9-9	19/06:50	19/06:30	19/05:50	19/01:05	NaT	53.1,2.48,0.377,0.25,NaN
42	02-Mar-22/10:12	M1.6	0.0615	19	22/11:06	1750	360	2-2-9-9-9	23/13:20	23/08:20	NaT	NaT	NaT	16.2,0.45,NaN,NaN,NaN
43	02-Apr-17/07:46	M2.6	0.156	34	17/08:26	1240	360	2-2-2-9-9	17/15:40	17/15:35	17/15:35	NaT	NaT	24.1,1.51,0.367,NaN,NaN
44	02-Apr-21/00:43	X1.5	0.748	84	21/01:27	2393	360	3-3-3-3-3	21/23:20	21/10:50	21/10:25	21/10:25	21/10:25	2520,649,208,108,22.9
45	02-May-21/21:29	C2	NaN	56	NaT	NaN	NaN	2-2-2-2-9	23/10:55	23/10:45	23/16:40	23/11:25	NaT	820,10.2,1.15,0.56,NaN
46	02-Jul-07/11:15	M1	0.0881	90	07/11:30	1423	228	0-0-0-0-9	07/19:55	07/23:30	07/19:05	07/19:05	07/19:05	22.6,2.81,0.711,0.46,NaN
47	02-Aug-14/01:47	M2.3	0.0936	54	14/02:30	1309	133	0-0-0-0-9	14/16:20	14/07:30	14/07:30	14/07:30	14/07:30	26.4,0.77,0.364,0.29,NaN
48	02-Aug-18/21:12	M2.2	0.0217	19	18/21:54	682	140	2-2-2-9-9	19/08:20	19/01:20	18/23:00	NaT	NaT	3.7,0.68,0.325,NaN,NaN
49	02-Aug-20/08:22	M3.4	0.0074	38	20/08:54	1099	122	3-3-3-9-9	20/11:20	20/10:10	20/14:00	NaT	NaT	2.53,0.53,0.217,NaN,NaN
50	02-Aug-22/01:47	M5.4	0.0324	62	22/02:06	998	360	4-4-4-4-4	22/09:40	22/05:15	22/05:10	22/05:10	22/05:10	36.4,12.6,5.98,4.3,1.71
51	02-Aug-24/00:49	X3.1	0.453	81	24/01:27	1913	360	4-4-4-4-4	24/08:35	24/03:00	24/02:50	24/02:45	24/02:10	317,123,76.2,60.4,29.3
52	02-Nov-09/13:08	M4.6	0.0477	29	09/13:31	1838	360	0-0-0-0-9	10/05:40	10/05:55	10/05:40	10/05:40	NaT	404,12,1.46,0.73,NaN
53	02-Nov-24/20:14	C6.4	0.0234	37	24/20:30	1077	360	0-0-9-9-9	26/02:50	NaT	NaT	NaT	NaT	1.81,NaN,NaN,NaN,NaN
54	03-May-28/00:17	X3.6	0.295	20	28/00:50	1366	360	3-3-3-3-3	29/16:05	29/16:45	28/16:05	29/16:45	29/16:45	95.7,4.84,0.519,3.64,NaN
55	03-May-31/02:13	M9.3	0.0901	65	31/02:30	1835	360	3-3-3-3-3	31/06:30	31/06:05	31/05:20	31/04:15	31/04:25	17,5.58,2.92,2.02,0.881
56	03-Oct-26/17:21	X1.2	0.97	38	26/17:54	1537	171	4-4-4-4-4	27/02:00	27/01:40	26/19:40	NaT	27/03:05	442,41.6,10.4,5.13,1.14
57	03-Nov-02/17:03	X8.3	0.986	56	02/17:30	2598	360	0-0-0-0-0	03/01:25	02/22:10	02/22:10	02/19:10	02/19:05	1210,460,155,103,49.4
58	03-Nov-04/19:29	X28	2.45	83	04/19:54	2657	360	4-4-9-9-9	05/07:55	05/06:10	05/06:15	05/06:10	05/05:40	145,30.9,15.3,5.11,1.33
59	03-Nov-20/23:42	M5.8	0.0291	17	21/00:26	494	52	0-0-0-0-9	22/02:25	22/02:20	22/02:25	NaT	NaT	12.2,0.82,NaN,NaN,NaN
60	03-Dec-02/10:00	C1	NaN	NaN	NaT	NaN	NaN	0-0-0-0-9	02/18:20	02/16:50	02/15:50	NaT	NaT	23.6,1.72,0.393,NaN,NaN
61	04-Apr-11/03:54	C9.6	0.0141	46	11/04:30	1645	314	0-0-0-0-9	11/18:45	11/12:25	11/14:35	NaT	NaT	35.5,1.74,0.483,0.35,NaN

Table 2.4 continued from previous page

INDEX	FLARE ONSET[1]	SXR FLUX[2]	SXR FLUENCE[3]	LONGITUDE	CME DATE[4]	CME SPEED	CME WIDTH	CLASS[5]	PEAK 10MeV	PEAK 30MeV	PEAK 50MeV	PEAK 60MeV	PEAK 100MeV[4]	PEAK FLUX[6]
62	04-Jul-25/14:19	M1.1	0.0444	33	NaT	NaN	NaN	3-3-3-3-9	26/22:50	26/22:50	26/22:45	26/22:40	NaT	2090,30.5,2.13,0.83,NaN
63	04-Jul-31/05:16	C8.4	0.0432	95	31/05:54	1192	197	3-3-3-9-9-9	01/21:50	01/22:05	NaT	NaT	NaT	7.89,1.21,NaN,NaN,NaN
64	04-Sep-19/16:46	M1.9	0.0402	58	NaT	NaN	NaN	3-3-3-3-3-3	20/01:00	19/21:40	19/21:15	19/21:15	19/21:15	57.3,8.87,2.6,1.49,0.37
65	04-Nov-01/05:55	C1	NaN	90	NaT	NaN	NaN	0-0-0-0-0-0	01/08:05	01/07:50	01/07:10	01/06:55	01/06:45	63.1,17.4,7.5,4.71,1.51
66	04-Nov-07/15:42	X2	0.208	17	07/16:54	1759	360	3-3-3-3-3	08/01:15	07/23:35	07/23:25	07/23:25	07/22:15	495,26,4.73,2.49,0.54
67	04-Nov-09/16:59	M8.9	0.0979	51	09/17:26	2000	360	3-3-3-3-3-3	09/21:30	10/03:55	10/03:55	10/03:30	10/03:30	82.4,21.1,8.99,6.37,2.42
68	04-Nov-10/01:59	X2.5	0.165	49	10/02:26	3387	360	3-3-3-3-3-3	10/16:55	10/10:10	10/10:20	10/10:20	10/03:30	424,49.4,13.5,7.52,2.42
69	05-Jan-17/06:59	X3.8	0.904	25	NaT	NaN	NaN	5-5-5-5-5-5	17/17:50	17/17:50	17/17:40	17/17:00	17/17:00	5040,1330,387,166,28.1
70	05-Jan-20/06:36	X7.1	1.46	61	20/06:54	882	360	4-4-4-4-4-4	20/08:10	20/07:45	20/07:45	20/07:10	20/07:10	1860,1550,1150,968,652
71	05-Jun-16/20:01	M4	0.0656	90	NaT	NaN	NaN	3-3-3-3-3	17/05:00	17/02:45	16/23:15	16/23:15	16/23:15	43.8,17.1,9.71,7.31,2.94
72	05-Jul-13/14:01	M5	0.316	90	13/14:30	1423	360	4-4-4-4-4-4	14/01:40	14/00:35	14/00:35	14/01:20	14/01:30	9.53,1.16,0.321,0.22,0.0885
73	05-Jul-14/10:16	X1.2	0.556	90	14/10:54	2115	360	5-5-5-5-5-5	15/03:45	15/00:25	15/00:25	15/00:50	15/01:55	134,14.2,2.63,1.09,0.205
74	05-Jul-17/11:29	C1	NaN	100	NaT	NaN	NaN	3-3-3-3-9	17/22:40	17/18:00	17/18:25	18/03:40	NaT	22.1,3.82,1.03,0.48,NaN
75	05-Aug-22/00:44	M2.6	0.134	54	22/01:31	1194	360	1-1-1-9-9	22/06:40	22/05:25	22/04:35	23/02:10	NaT	7.28,0.82,0.341,NaN,NaN
76	05-Aug-22/16:46	M5.6	0.23	65	22/17:30	2378	360	1-1-1-1-1	23/10:45	23/02:00	23/02:15	23/02:10	23/02:10	337,27.2,4.8,2.06,0.373
77	06-Dec-13/02:14	X3.4	0.552	23	13/02:54	1774	360	1-1-1-1-1	13/09:25	13/06:25	13/06:10	13/06:00	13/05:25	698,372,239,187,88.7
78	06-Dec-14/21:07	X1.5	0.132	46	14/22:30	1042	360	3-3-3-3-3	15/00:15	15/00:15	14/23:35	15/00:15	15/00:15	215,42.3,13.5,8.07,2.38
79	10-Aug-14/09:38	C4.4	0.0133	56	14/10:12	1205	360	0-0-0-0-9	15/00:15	14/12:35	14/11:55	14/12:35	NaT	14.9,1.69,0.45157,0.46,NaN
80	10-Aug-18/04:45	C4.5	0.0279	88	18/05:48	1471	184	0-0-9-9-9	18/11:50	18/13:50	NaT	NaT	NaT	3.35,0.54,NaN,NaN,NaN
81	11-Mar-07/19:43	M3.7	0.136	48	07/20:00	2125	360	3-3-3-3-9	08/07:35	08/07:25	08/08:55	08/12:30	NaT	40.32,3.97,10498,0.4,NaN
82	11-Jun-07/06:16	M2.5	0.0432	53	07/06:49	1255	360	4-4-4-4-4-4	07/18:20	07/10:25	07/10:25	07/10:20	07/10:25	70.61,22.26,14403,9.67,45281
83	11-Aug-04/03:41	M9.3	0.053	38	04/04:12	1315	360	1-1-1-1-1	04/12:45	04/08:55	04/08:05	04/08:45	04/07:40	44.23,14.31,84293,4.35,17984
84	11-Aug-09/07:48	X6.9	0.186	69	09/08:12	1610	360	4-4-4-4-4-4	09/09:25	09/09:05	09/08:55	09/08:45	09/08:55	21.45,13.95,86474,6.02,26732
85	11-Sep-06/22:12	X2.1	0.0565	18	06/23:05	575	360	1-1-1-1-1	07/07:05	07/04:20	07/05:00	07/04:10	07/04:10	6.74,2.92,16101,0.97,0.41039
86	11-Sep-22/10:29	X1.4	0.614	89	22/10:48	1905	360	5-5-5-5-5-5	24/08:45	23/09:40	23/10:45	23/05:05	23/10:05	8.69,1.27,0.56962,0.36,0.21079
87	11-Oct-22/10:00	M1.3	0.134	87	22/10:24	1005	360	3-3-3-9-9-9	23/15:35	22/23:20	NaT	NaT	NaT	9.23,0.3,NaN,NaN,NaN
88	11-Nov-26/06:09	C1.2	0.0152	47	NaT	NaN	NaN	0-0-0-0-0-0	27/09:30	26/16:35	26/16:25	26/16:15	27/02:25	51.02,2.35,0.50767,0.27,0.1189
89	12-Jan-23/03:38	M8.7	0.204	25	23/04:00	2175	360	4-4-4-4-4-4	24/15:35	23/15:30	23/15:30	23/15:35	23/07:50	5107.2,352.58,76.18,18.83,23859
90	12-Jan-27/17:37	X1.7	0.315	71	27/18:27	2508	360	0-0-0-0-0-0	28/02:20	28/01:50	28/01:00	28/00:35	27/21:40	577.68,121.1,47197,26.7,11.88
91	12-Mar-13/17:12	M7.9	0.326	59	13/17:36	1884	360	4-4-4-4-4-4	13/20:45	13/19:10	13/19:10	13/18:40	13/19:05	284.75,65.73,17867,10.65,18856
92	12-May-17/01:25	M5.1	0.138	76	17/01:48	1582	360	3-3-3-3-3	17/04:30	17/03:45	17/03:00	17/03:10	17/02:30	233.12,109.97,78292,49.52,20445
93	12-Jul-06/23:01	X1.1	0.0418	59	06/23:24	1828	360	5-5-5-5-5-5	07/07:25	07/07:25	07/07:25	07/04:15	07/04:30	20.47,4.87,18279,1.01,0.36866
94	12-Jul-08/16:23	M6.9	0.0442	83	08/16:36	1572	157	3-3-3-3-3	09/01:35	09/01:50	09/03:55	09/01:50	09/01:50	18.16,6.27,29287,1.89,0.70636
95	12-Jul-12/15:37	X1.4	0.709	15	12/16:48	885	360	0-0-0-0-0-0	12/22:25	12/20:30	12/19:05	12/18:45	12/17:35	64.72,3.5,0.85249,0.48,0.25117
96	12-Jul-17/12:03	M1.7	0.247	88	17/13:25	292	95	4-4-4-4-9	18/06:00	18/04:50	18/04:45	18/01:45	NaT	80.56,4.85,1127,0.45,NaN
97	12-Jul-19/04:17	M7.7	0.519	88	19/05:24	1631	360	5-5-5-5-5-5	20/05:10	19/14:20	19/12:20	19/10:15	19/09:25	75.75,13.35,51658,2.66,0.73074
98	12-Sep-27/23:36	C3.7	0.0122	32	28/00:12	947	360	1-1-1-1-1	28/04:45	28/04:45	28/05:25	28/04:10	28/09:20	16.32,2.4,0.79263,0.43,0.15892

[1] Year-Month-Day/Hour:Minute
[2] Maximum SXR flux of the associated flare
[3] Start-to-end SXR fluence of the associated flare
[4] Day/Hour:Minute of the same year and month of flare onset
[5] The first number indicates the event class and the following 5 are the class number at each energy channel (>10MeV, >30MeV, >50MeV, >60MeV, >100MeV correspondingly)
[6] Each value represents the peak intensity at each energy channel (E>10MeV, E>30MeV, E>50MeV, E>60MeV, E>100MeV correspondingly)
- NaN/NaT values indicate the absence of a value/date correspondingly.

-Units of measurement:
Angles (longitude and CME width): degrees (°)
CME speed: km/s
flare SXR flux: W/m^2
flare SXR fluence: J/m^2
proton intensities: protons/cm^2/sec/sr (pfu)

Table 2.5: ICME list

SEP INDEX[1]	TYPE[2]	DISTURBANCE[3]	ICME START[4]	ICME END[4]	ICME SPEED (km/s)[5]	LASCO CME[4,6]	MC[7]	MC START[4,7]	MC END[4,7]
1	DRIVER	97-Nov-06/22:00	07/04:00	09/12:00	400	04/06:00	2	07/15:00	08/15:00
2	INT	97-Nov-06/22:00	07/04:00	09/12:00	400	04/06:00	2	07/15:00	08/15:00
3	NON	NaT	NaT	NaT	NaN	NaT	NaN	NaT	NaT
4	INT	98-May-01/22:00	02/05:00	04/02:00	520	29/17:00	2	02/12:00	03/17:00
4	DRIVER	98-May-04/00:00	04/10:00	07/23:00	550	02/14:00	0	NaT	NaT
5	INT	98-May-01/22:00	02/05:00	04/02:00	520	29/17:00	2	02/12:00	03/17:00
5	INT	98-May-04/00:00	04/10:00	07/23:00	550	02/14:00	0	NaT	NaT
6	INT	98-May-04/00:00	04/10:00	07/23:00	550	02/14:00	0	NaT	NaT
7	INT	98-Jun-13/19:00	14/04:00	15/06:00	340	NaT	1	NaT	NaT
8	NON	NaT	NaT	NaT	NaN	NaT	NaN	NaT	NaT
9	INT	98-Nov-07/08:00	07/22:00	09/01:00	450	04/08:00	1	NaT	NaT
9	DRIVER	98-Nov-08/05:00	09/01:00	11/01:00	450	05/20:00	2	09/01:00	10/01:00
10	NON	NaT	NaT	NaT	NaN	NaT	NaN	NaT	NaT
11	INT	99-Jun-02/20:00	02/23:00	03/22:00	430	NaT	1	NaT	NaT
12	INT	99-Jun-02/20:00	02/23:00	03/22:00	430	NaT	1	NaT	NaT
13	INT	00-Feb-14/07:00	14/12:00	16/08:00	520	12/04:00	0	NaT	NaT
13	INT	00-Feb-20/21:00	21/05:00	22/12:00	380	17/20:00	2	21/10:00	22/12:00
14	DRIVER	00-Apr-06/16:00	07/06:00	08/06:00	560	04/16:00	1	NaT	NaT
15	INT	00-May-13/17:00	13/17:00	14/18:00	500	10/20:00	0	NaT	NaT
15	INT	00-May-15/19:00	15/19:00	16/14:00	430	NaT	0	NaT	NaT
15	INT	00-May-16/23:00	16/23:00	17/07:00	550	13/12:00	1	NaT	NaT
16	INT	00-Jun-08/09:00	08/12:00	10/17:00	610	06/16:00	0	NaT	NaT
16	INT	00-Jun-11/08:00	11/09:00	11/18:00	510	NaT	1	NaT	NaT
16	INT	00-Jun-12/22:00	13/12:00	14/06:00	440	NaT	0	NaT	NaT
17	INT	00-Jun-23/13:00	24/00:00	26/08:00	500	NaT	2	24/03:00	25/20:00
17	INT	00-Jun-26/00:00	26/10:00	27/00:00	520	NaT	0	NaT	NaT
18	INT	00-Jul-19/15:00	20/01:00	21/08:00	530	17/00:00	0	NaT	NaT
18	INT	00-Jul-23/10:00	23/15:00	26/05:00	360	NaT	0	NaT	NaT
18	INT	00-Jul-26/19:00	27/02:00	28/02:00	360	23/05:00	1	NaT	NaT
19	INT	00-Aug-10/05:00	10/19:00	11/21:00	430	06/22:00	2	10/19:00	11/08:00
19	INT	00-Aug-11/18:00	12/05:00	13/22:00	580	09/16:00	2	12/05:00	13/05:00
20	INT	00-Oct-12/22:00	13/16:00	14/17:00	400	10/00:00	2	13/18:00	14/17:00
21	DRIVER	00-Oct-28/10:00	28/21:00	29/22:00	380	25/08:00	2	28/21:00	29/22:00
22	INT	00-Nov-06/09:00	06/17:00	08/03:00	510	03/18:00	2	06/22:00	07/18:00
22	INT	00-Nov-08/12:00	08/13:00	09/15:00	440	NaT	1	NaT	NaT
22	INT	00-Nov-11/00:00	11/08:00	12/00:00	790	NaT	0	NaT	NaT
23	INT	01-Jan-23/10:00	24/09:00	26/07:00	400	20/21:00	1	NaT	NaT
24	INT	01-Mar-27/00:00	27/20:00	28/17:00	610	NaT	2	27/20:00	28/05:00
24	INT	01-Mar-27/17:00	28/17:00	30/18:00	480	25/17:00	0	NaT	NaT
24	DRIVER	01-Mar-31/22:00	01/04:00	03/15:00	600	29/10:00	1	NaT	NaT
25	INT	01-Mar-27/17:00	28/17:00	30/18:00	480	25/17:00	0	NaT	NaT
25	INT	01-Mar-31/01:00	31/05:00	31/22:00	640	28/13:00	1	NaT	NaT
25	INT	01-Mar-31/22:00	01/04:00	03/15:00	600	29/10:00	1	NaT	NaT
25	DRIVER	01-Apr-04/15:00	04/18:00	05/12:00	650	02/22:00	2	04/18:00	05/08:00
26	INT	01-Apr-11/13:00	11/22:00	13/07:00	640	10/05:00	2	12/08:00	12/18:00
26	INT	01-Apr-13/07:00	13/09:00	14/12:00	730	11/13:00	0	NaT	NaT
27	INT	01-Apr-11/13:00	11/22:00	13/07:00	640	10/05:00	2	12/08:00	12/18:00
27	INT	01-Apr-13/07:00	13/09:00	14/12:00	730	11/13:00	0	NaT	NaT
27	INT	01-Apr-15/17:00	15/17:00	16/01:00	500	NaT	0	NaT	NaT
28	DRIVER	01-Apr-28/05:00	28/14:00	01/02:00	550	26/12:00	2	29/02:00	29/13:00
29	INT	01-May-07/08:00	07/19:00	08/07:00	360	NaT	1	NaT	NaT
29	INT	01-May-08/11:00	09/12:00	10/22:00	430	NaT	1	NaT	NaT
30	NON	NaT	NaT	NaT	NaN	NaT	NaN	NaT	NaT
31	NON	NaT	NaT	NaT	NaN	NaT	NaN	NaT	NaT
32	NON	NaT	NaT	NaT	NaN	NaT	NaN	NaT	NaT
33	INT	01-Aug-17/11:00	17/20:00	19/16:00	500	14/16:00	0	NaT	NaT
34	INT	01-Sep-29/09:00	29/11:00	01/00:00	560	27/00:00	1	NaT	NaT
34	INT	01-Sep-30/19:00	01/08:00	02/00:00	490	28/09:00	0	NaT	NaT
34	INT	01-Oct-01/00:00	02/04:00	02/12:00	490	29/12:00	0	NaT	NaT
34	INT	01-Oct-02/12:00	02/14:00	03/16:00	500	NaT	2	03/01:00	03/16:00
35	DRIVER	01-Oct-21/16:00	21/20:00	25/10:00	460	19/17:00	0	NaT	NaT
36	INT	01-Oct-21/16:00	21/20:00	25/10:00	460	19/17:00	0	NaT	NaT
36	INT	01-Oct-26/22:00	27/03:00	28/12:00	420	22/18:00	0	NaT	NaT
36	DRIVER	01-Oct-28/03:00	29/22:00	31/13:00	360	25/15:00	0	NaT	NaT
37	INT	01-Oct-31/13:00	31/20:00	02/12:00	330	NaT	2	31/20:00	02/10:00
37	INT	01-Nov-05/10:00	05/19:00	06/06:00	420	NaT	1	NaT	NaT
37	DRIVER	01-Nov-06/02:00	06/12:00	09/03:00	600	04/16:00	1	NaT	NaT
38	INT	01-Nov-19/18:00	19/22:00	21/13:00	430	17/05:00	1	NaT	NaT
38	INT	01-Nov-24/07:00	24/14:00	25/20:00	720	22/23:00	2	24/14:00	25/14:00
39	INT	01-Dec-28/00:00	28/00:00	29/12:00	360	NaT	0	NaT	NaT
40	NON	NaT	NaT	NaT	NaN	NaT	NaN	NaT	NaT
41	INT	02-Mar-18/13:00	19/05:00	20/16:00	380	15/23:00	2	19/23:00	20/16:00
41	INT	02-Mar-20/13:00	21/14:00	22/06:00	440	NaT	0	NaT	NaT
42	INT	02-Mar-18/13:00	19/05:00	20/16:00	380	15/23:00	2	19/23:00	20/16:00
42	INT	02-Mar-20/13:00	21/14:00	22/06:00	440	NaT	0	NaT	NaT
42	INT	02-Mar-23/11:00	24/12:00	25/20:00	450	20/00:00	2	24/12:00	25/22:00
43	INT	02-Apr-17/11:00	17/16:00	19/15:00	480	15/04:00	2	18/03:00	19/02:00
43	DRIVER	02-Apr-19/08:00	20/00:00	21/18:00	500	17/08:00	2	20/12:00	21/18:00
44	INT	02-Apr-17/11:00	17/16:00	19/15:00	480	15/04:00	2	18/03:00	19/02:00
44	INT	02-Apr-19/08:00	20/00:00	21/18:00	500	17/08:00	2	20/12:00	21/18:00

Table 2.5 continued from previous page

SEP INDEX [1]	TYPE [2]	DISTURBANCE DATE [3]	ICME START [4]	ICME END [4]	ICME SPEED (km/s) [5]	LASCO CME DATE[4,6]	MC [7]	MC START[4,7]	MC END[4,7]
45	INT	02-May-20/03:00	20/10:00	21/22:00	420	16/01:00	1	NaT	NaT
45	INT	02-May-23/11:00	23/20:00	25/18:00	590	22/03:00	2	23/23:00	24/17:00
46	NON	NaT	NaT	NaT	NaN	NaT	NaN	NaT	NaT
47	NON	NaT	NaT	NaT	NaN	NaT	NaN	NaT	NaT
48	INT	02-Aug-18/18:00	19/12:00	21/14:00	460	16/12:00	1	NaT	NaT
49	INT	02-Aug-18/18:00	19/12:00	21/14:00	460	16/12:00	1	NaT	NaT
50	INT	02-Aug-18/18:00	19/12:00	21/14:00	460	16/12:00	1	NaT	NaT
51	INT	02-Aug-18/18:00	19/12:00	21/14:00	460	16/12:00	1	NaT	NaT
52	NON	NaT	NaT	NaT	NaN	NaT	NaN	NaT	NaT
53	NON	NaT	NaT	NaT	NaN	NaT	NaN	NaT	NaT
54	DRIVER	03-May-29/00:00	30/02:00	30/16:00	600	28/01:00	1	NaT	NaT
54	INT	03-May-29/12:00	29/13:00	29/18:00	650	NaT	1	NaT	NaT
54	INT	03-May-30/00:00	30/22:00	01/01:00	680	29/01:00	0	NaT	NaT
55	INT	03-May-29/00:00	30/02:00	30/16:00	600	28/01:00	1	NaT	NaT
55	INT	03-May-29/12:00	29/13:00	29/18:00	650	NaT	1	NaT	NaT
55	INT	03-May-30/00:00	30/22:00	01/01:00	680	29/01:00	0	NaT	NaT
56	INT	03-Oct-21/22:00	22/02:00	24/15:00	520	NaT	1	NaT	NaT
56	INT	03-Oct-24/15:00	24/21:00	25/12:00	560	22/08:00	1	NaT	NaT
56	INT	03-Oct-25/11:00	25/14:00	26/04:00	490	NaT	0	NaT	NaT
56	INT	03-Oct-26/19:00	26/22:00	28/00:00	470	NaT	1	NaT	NaT
56	DRIVER	03-Oct-28/02:00	28/02:00	28/09:00	610	26/18:00	0	NaT	NaT
56	INT	03-Oct-29/06:00	29/11:00	30/03:00	1300	28/11:00	2	29/11:00	30/03:00
57	INT	03-Oct-30/00:00	31/02:00	02/00:00	800	29/21:00	1	NaT	NaT
58	INT	03-Oct-30/00:00	31/02:00	02/00:00	800	29/21:00	1	NaT	NaT
59	INT	03-Nov-20/08:00	20/10:00	21/08:00	580	18/09:00	2	20/10:00	21/02:00
60	NON	NaT	NaT	NaT	NaN	NaT	NaN	NaT	NaT
61	NON	NaT	NaT	NaT	NaN	NaT	NaN	NaT	NaT
62	INT	04-Jul-22/10:00	22/18:00	24/08:00	560	20/13:00	2	22/15:00	22/21:00
62	INT	04-Jul-24/06:00	24/14:00	25/15:00	560	22/07:00	2	24/14:00	25/15:00
62	INT	04-Jul-25/15:00	25/20:00	26/22:00	640	23/16:00	1	NaT	NaT
62	DRIVER	04-Jul-26/22:00	27/02:00	27/22:00	870	25/15:00	2	27/02:00	27/12:00
63	INT	04-Aug-01/01:00	01/09:00	02/04:00	440	NaT	1	NaT	NaT
64	INT	04-Sep-17/21:00	18/12:00	20/00:00	400	14/10:00	1	NaT	NaT
65	NON	NaT	NaT	NaT	NaN	NaT	NaN	NaT	NaT
66	INT	04-Nov-07/18:00	07/22:00	09/10:00	630	04/23:00	2	08/02:00	08/17:00
66	DRIVER	04-Nov-09/00:00	09/20:00	11/23:00	640	07/17:00	2	09/20:00	10/11:00
67	INT	04-Nov-07/18:00	07/22:00	09/10:00	630	04/23:00	2	08/02:00	08/17:00
67	INT	04-Nov-09/00:00	09/20:00	11/23:00	640	07/17:00	2	09/20:00	10/11:00
67	INT	04-Nov-11/17:00	12/08:00	13/23:00	520	10/02:00	1	NaT	NaT
68	INT	04-Nov-07/18:00	07/22:00	09/10:00	630	04/23:00	2	08/02:00	08/17:00
68	INT	04-Nov-09/00:00	09/20:00	11/23:00	640	07/17:00	2	09/20:00	10/11:00
68	DRIVER	04-Nov-11/17:00	12/08:00	13/23:00	520	10/02:00	1	NaT	NaT
69	INT	05-Jan-16/11:00	16/14:00	17/07:00	520	13/18:00	1	NaT	NaT
69	INT	05-Jan-18/21:00	18/23:00	20/03:00	800	17/09:00	0	NaT	NaT
70	INT	05-Jan-16/11:00	16/14:00	17/07:00	520	13/18:00	1	NaT	NaT
70	INT	05-Jan-18/21:00	18/23:00	20/03:00	800	17/09:00	0	NaT	NaT
70	DRIVER	05-Jan-21/17:00	21/19:00	22/17:00	810	20/07:00	0	NaT	NaT
71	INT	05-Jun-14/18:00	15/05:00	16/09:00	480	NaT	2	15/05:00	16/09:00
71	INT	05-Jun-16/08:00	16/17:00	17/19:00	600	NaT	1	NaT	NaT
72	INT	05-Jul-10/03:00	10/10:00	12/04:00	430	07/17:00	1	NaT	NaT
73	INT	05-Jul-10/03:00	10/10:00	12/04:00	430	07/17:00	1	NaT	NaT
73	INT	05-Jul-17/01:00	17/14:00	18/23:00	420	NaT	2	17/14:00	18/04:00
74	INT	05-Jul-17/01:00	17/14:00	18/23:00	420	NaT	2	17/14:00	18/04:00
75	INT	05-Aug-23/20:00	24/00:00	24/11:00	440	NaT	1	NaT	NaT
75	DRIVER	05-Aug-24/06:00	24/14:00	24/23:00	660	22/00:00	1	NaT	NaT
76	INT	05-Aug-23/20:00	24/00:00	24/11:00	440	NaT	1	NaT	NaT
76	INT	05-Aug-24/06:00	24/14:00	24/23:00	660	22/00:00	1	NaT	NaT
77	DRIVER	06-Dec-14/14:00	14/22:00	15/13:00	740	13/03:00	2	14/22:00	15/20:00
77	INT	06-Dec-15/20:00	15/20:00	16/19:00	620	NaT	0	NaT	NaT
78	INT	06-Dec-14/14:00	14/22:00	15/13:00	740	13/03:00	2	14/22:00	15/20:00
78	INT	06-Dec-15/20:00	15/20:00	16/19:00	620	NaT	0	NaT	NaT
78	DRIVER	06-Dec-16/18:00	17/00:00	17/17:00	580	14/22:00	0	NaT	NaT
79	NON	NaT	NaT	NaT	NaN	NaT	NaN	NaT	NaT
80	NON	NaT	NaT	NaT	NaN	NaT	NaN	NaT	NaT
81	INT	11-Mar-06/03:00	06/09:00	08/06:00	430	03/05:00	0	NaT	NaT
82	INT	11-Jun-04/20:00	05/02:00	05/19:00	510	02/07:00	2	NaT	NaT
83	INT	11-Aug-04/22:00	05/05:00	05/14:00	430	02/06:00	1	NaT	NaT
83	DRIVER	11-Aug-05/18:00	06/22:00	07/22:00	540	04/04:00	1	NaT	NaT
84	INT	11-Aug-05/18:00	06/22:00	07/22:00	540	04/04:00	1	NaT	NaT
85	INT	11-Sep-08/10:00	08/10:00	09/12:00	320	NaT	1	NaT	NaT
85	DRIVER	11-Sep-09/12:00	10/03:00	10/15:00	470	06/23:00	2	NaT	NaT
86	INT	11-Sep-22/03:00	22/15:00	23/03:00	390	NaT	1	NaT	NaT
86	INT	11-Sep-26/12:00	26/20:00	28/15:00	580	24/12:00	0	NaT	NaT
87	INT	11-Oct-22/21:00	22/21:00	23/16:00	290	NaT	1	NaT	NaT
87	INT	11-Oct-24/18:00	24/22:00	25/16:00	460	22/00:00	2	24/22:00	25/16:00
88	DRIVER	11-Nov-28/22:00	29/00:00	29/08:00	450	26/07:00	2	29/00:00	29/08:00
89	INT	12-Jan-21/05:00	21/06:00	22/08:00	320	18/12:00	2	NaT	NaT
89	INT	12-Jan-22/06:00	22/23:00	23/07:00	450	19/14:00	2	NaT	NaT
90	NON	NaT	NaT	NaT	NaN	NaT	NaN	NaT	NaT
91	INT	12-Mar-08/11:00	09/03:00	11/07:00	550	07/00:00	1	NaT	NaT
91	DRIVER	12-Mar-15/13:00	15/17:00	16/10:00	680	13/17:00	1	NaT	NaT

Table 2.5 continued from previous page

SEP INDEX [1]	TYPE [2]	DISTURBANCE DATE [3]	ICME START [4]	ICME END [4]	ICME SPEED (km/s) [5]	LASCO CME DATE[4,6]	MC [7]	MC START[4,7]	MC END[4,7]
92	INT	12-May-16/16:00	16/16:00	17/22:00	370	12/00:00	2	NaT	NaT
93	INT	12-Jul-04/19:00	05/00:00	06/08:00	470	02/08:00	1	NaT	NaT
93	INT	12-Jul-08/08:00	09/00:00	09/14:00	410	04/17:00	2	NaT	NaT
94	INT	12-Jul-04/19:00	05/00:00	06/08:00	470	02/08:00	1	NaT	NaT
94	INT	12-Jul-08/08:00	09/00:00	09/14:00	410	04/17:00	2	NaT	NaT
95	DRIVER	12-Jul-14/18:00	15/06:00	17/05:00	490	12/16:00	2	NaT	NaT
96	INT	12-Jul-14/18:00	15/06:00	17/05:00	490	12/16:00	2	NaT	NaT
97	INT	12-Jul-14/18:00	15/06:00	17/05:00	490	12/16:00	2	NaT	NaT
97	INT	12-Jul-21/16:00	22/11:00	23/16:00	460	NaT	0	NaT	NaT
98	INT	12-Sep-30/11:00	30/14:00	30/20:00	310	NaT	0	NaT	NaT
98	DRIVER	12-Sep-30/23:00	01/00:00	02/00:00	370	28/00:00	2	NaT	NaT

[1] Index of the associated SEP event

[2] *INT*: not associated with driver CME, *DRIVER*: counterpart of the driver CME, *NON*: no ICME detected within a 3-days interval

[3] *Year-Month-Day/Hour:Minute*

[4] *Day/Hour:Minute* of the same year and month of disturbance date

[5] average ICME speed

[6] Probable coronal mass ejection (CME) associated with the ICME, observed by LASCO

[7] MC index, start and end date

- NaN/NaT values indicate the absence of a value/date correspondingly.

3   DATA ANALYSIS

In this section, we explain the process in which the SEP and ICME databases are analysed in a statistical manner. Firstly, the distributions of the solar parameters and correlations amongst them are investigated in subsection 3.1. Following, the statistical relationship between the maximum proton intensity and several factors regarding the IMF configuration and the solar conditions, are investigated in subsection 3.2. Lastly, the spectral analysis of the SEP events is performed in subsection 3.3. The main goal of the analysis presented hereafter is to estimate in what degree the IP conditions affect the SEP intensity profiles.

3.1   Solar Activity

The parameters of the associated solar activity are the dominant factors that determine the main SEP characteristics. The distributions of three main solar characteristics (flare size, solar longitude of the associated flare, speed of the driver CME) for each class of events are presented in subsubsection 3.1.1. It is confirmed that, the CME speed correlates with both the peak SXR flux and SXR fluence of the associated flare, indicating a synergy between various mechanisms that trigger SEPs (subsubsection 3.1.2, for more see subsection 1.2, paragraph 1.3.1.4).

3.1.1   Distribution of Solar Parameters

The following figures show the distributions: of the associated flare size (C, M or X, figure 3.1), the speed of the driver CME (V_{CME}, figure 3.2) and the longitude of the associated flare (figure 3.3) for each class of events.

It can be observed that, most class 0 events (12/25, $\sim$50%) are associated with C class flares. Only 4 class 3 events ($\sim$13%) and 1 class 4 ($\sim$6%) event are associated with C flares. M and X flares are equally common for class 3 events and M flares are the most common for class 4, class 2 and class 1. Approximately half of class 5 events are associated with X flares (figure 3.1). It is also evident that MC events are mostly associated with X flares, while Pos/NoMC events with M flares.

Moreover, the average V_{CME} for class 0 events is lower in comparison to class 3 and 4 events, however the difference is not significant. Nevertheless, the standard deviation for class 0 events is smaller, meaning that class 3 and 4 spread to both lower and higher V_{CME} values (figure 3.2). MC and Pos/MC events have also similar V_{CME} values, however the MC distribution has a larger deviation. Generally, the distributions of both solar parameters add up to the fact that, at times if intense solar activity, i.e. the presence of ICMEs, all other parameters are more likely to be more energetic as well.

Lastly, figure 3.3 shows the longitudinal distribution of the events for each class. It is apparent that class 0 events originate mostly at western longitudes, with a clear peak in the interval [90°,100°), indicating that are more likely to follow the nominal Parker spiral. On the other hand, SEP events associated with ICMEs are scattered across all longitudes, suggesting that ICMEs can alter the path of particles. Moreover, the distributions of MC and Pos/NoMC events have almost equal means and standard deviations.

It should be noted, that deviations from the western-longitude picture exist for class 0, as well. This is not unexpected, because ICMEs are not the only factor affecting the transport of SEPs, as the driver CME also alters the path line followed by the particles. Furthermore, the speed of the solar wind alters the spirals and other structures, such as CIRs, could play a role (see paragraph 1.1.3.3 and subsubsection 1.3.3).
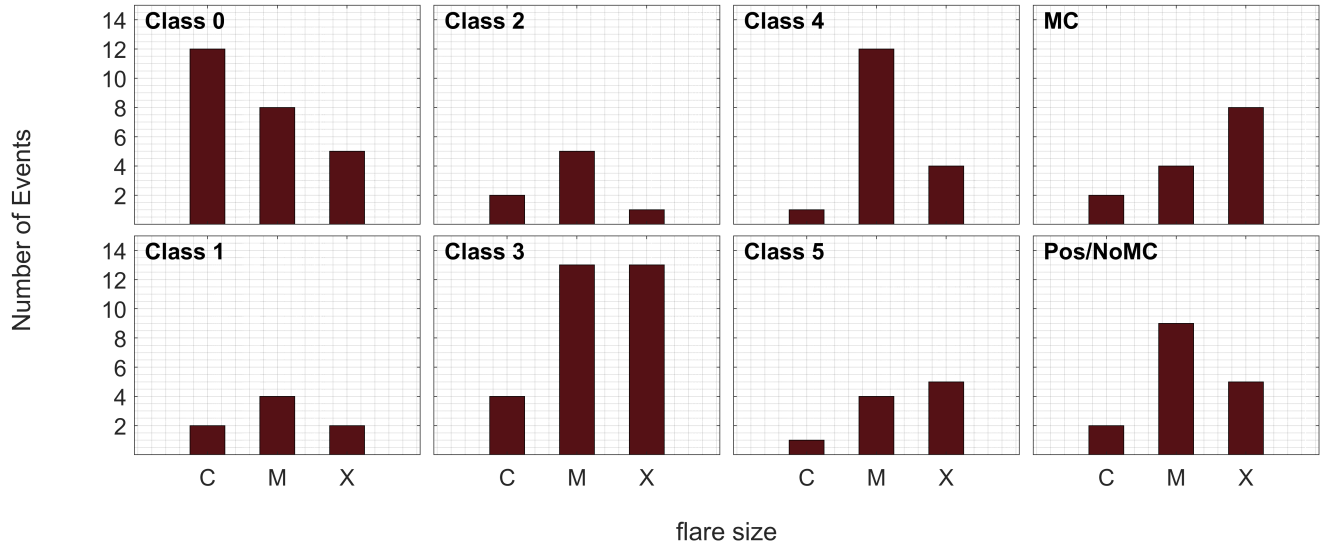
Figure 3.1: Flare size per class
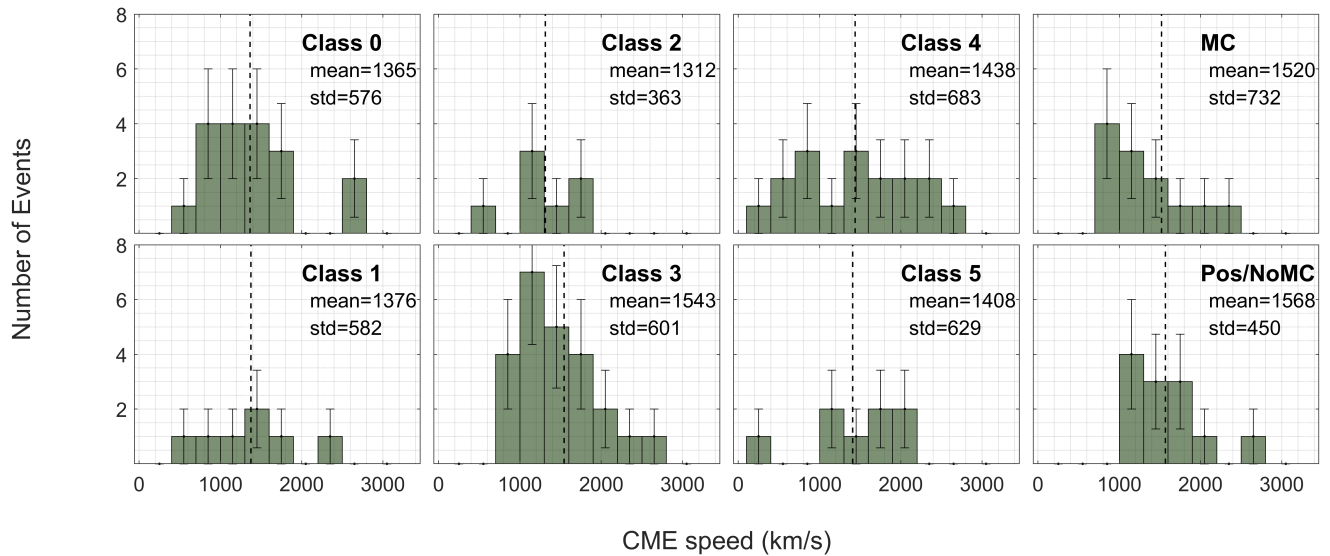
Figure 3.2: V_{CME} distribution per class

45
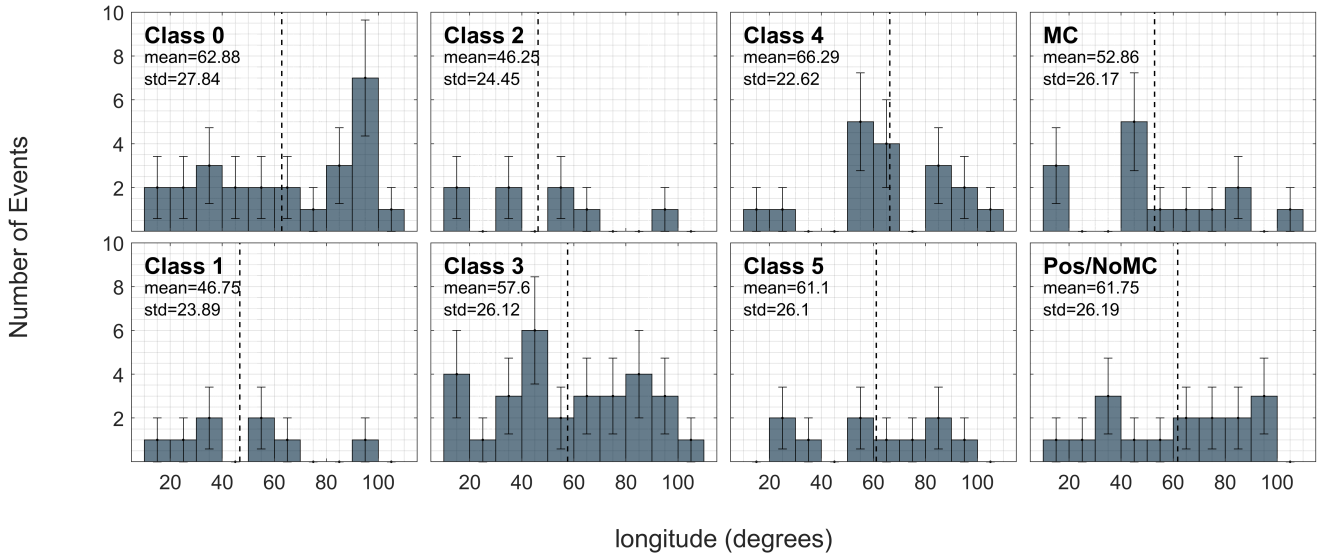
Figure 3.3: Longitudinal distribution per class

3.1.2   Correlation between the Solar Parameters

Here, we investigate the empirical relationships between the solar parameters. More specifically, these relationships concern the correlation of the driver CME speed (V_{CME}) with both the SXR peak flux (I_{SXR}) and SXR start-to-end fluence (J_{SXR}) of the flare. The number of events with both V_{CME} and I_{SXR} measurements are 82 and with both V_{CME} and J_{SXR} measurements are 81.

The model used is simple linear regression, assuming that:

$$\hat{I}_{SXR} = \hat{\beta}_I \cdot V_{CME} + \hat{\beta}_{0,I} + \epsilon_I \tag{3.1.1}$$

$$\hat{J}_{SXR} = \hat{\beta}_J \cdot V_{CME} + \hat{\beta}_{0,J} + \epsilon_J \tag{3.1.2}$$

$\hat{\beta}_I$ and $\hat{\beta}_{0,I}$, $\hat{\beta}_J$ and $\hat{\beta}_{0,J}$ are the estimated correlation coefficients of regression model for the V_{CME}-I_{SXR} and V_{CME}-J_{SXR} relations, correspondingly. The coefficients are calculated via the *least-squares* (LS) method. The term $\epsilon_{I/J}$ is the error term, $\hat{\beta}$ the slope of the LS fit line and $\hat{\beta}_0$ the intercept of the line with the yy' axis. The coefficient $\hat{\beta}_0$ doesn't have a physical meaning, as it corresponds to a CME with zero velocity. The model also provides the regression coefficient r.

The parameters $\hat{\beta}$, $\hat{\beta}_0$ and r of the linear equations 3.1.1 and 3.1.2 are calculated for the entire dataset and for each of the classes 0,3 and 4. Classes 1,2 and 5 are not taken into account, due to their low statistical sample. The parameters are calculated via the bootstrap method with 1000 repetitions (See A of the Appendix). Table 3.1 contains the regression coefficients $r \pm error$ for each linear model, where the $error = z^{(a)} \cdot \sigma$. For 90% confidence interval (CI), $z^{(a)}$=1.6449 [64].

The Student's t-test (Appendix B.1) is also applied to the whole dataset, in order to affirm whether the correlation between the measures is significant. The test can be used, since all three quantities stem from normal distributions. As seen in table 3.2, the correlations are significant at a 99% level of confidence. However, correlation values at table 3.1 exhibit large errors. Mathematically, errors stem
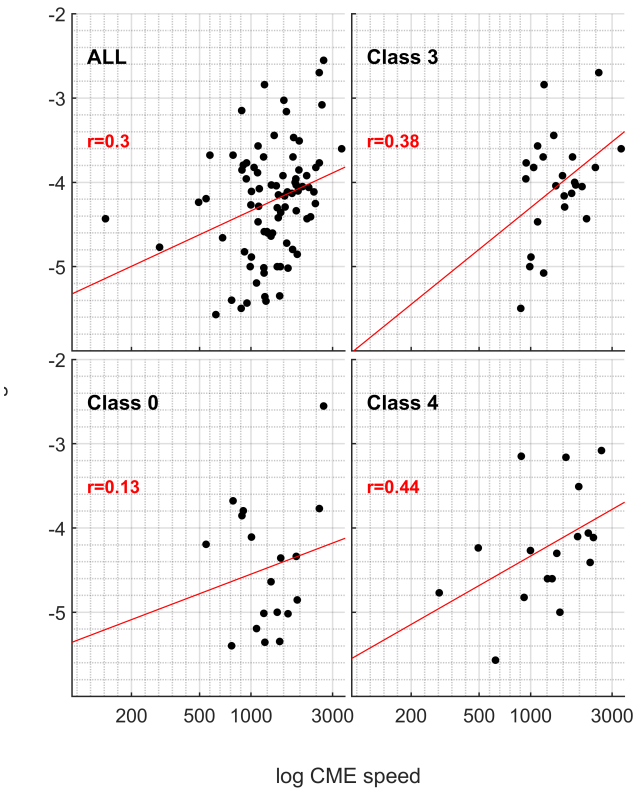
Figure 3.4: SXR peak Flux - CME speed

Figure 3.5: SXR fluence - CME speed

Sample	$\mathbf{I}_{SXR}$-$\mathbf{V}_{CME}$		$\mathbf{J}_{SXR}$-$\mathbf{V}_{CME}$	
	N	**r**	**N**	**r**
Class 0	18	0.13 ± 0.50	18	0.36 ± 0.43
Class 3	25	0.38 ± 0.28	24	0.43 ± 0.24
Class 4	17	0.44 ± 0.30	17	0.24 ± 0.42
All	82	0.30 ± 0.14	81	0.37 ± 0.15

Table 3.1: Regression Coefficients given by the bootstrap method. The errors are calculated for 90% CI

	$\mathbf{I}_{SXR}$-$\mathbf{V}_{CME}$	
Class	**p-value**	**Rej H$_0$**
All events	0.0059	Yes
	$\mathbf{J}_{SXR}$-$\mathbf{V}_{CME}$	
Class	**p value**	**Rej H$_0$**
All events	0.0012	Yes

Table 3.2: T-test results for 99% CI

form the intrinsic uncertainty of the problem, since the coefficient r is nothing but an estimate of the true value of the unknown relation. Moreover, errors arise from the method itself, as well as due to the small size of the dataset and the even smaller size of each class subset. Physically, uncertainties also stem from the fact that the CME speed is not the actual speed of the CME. In reality, the given CME speed is the projected one onto the plane of sky, meaning that the observed values are smaller than the actual ones. This phenomenon is known as the *projection effect* [16]. However, due to the small size of the sample, there will be no further analysis.

3.2   Proton Intensity

This section addresses the effect of various factors on the SEP proton intensities: the effect of the interplanetary magnetic field (IMF) configuration (subsubsection 3.2.1), the variation of the peak proton intensity with the number of ICMEs detected in the IP space, regardless of the underlying classification (paragraph 3.2.1.1) and the effect of the specific geometry between the ICME and the observer, at the time that the peak of the proton intensity (paragraph 3.2.1.2). Lastly, subsubsection 3.2.2 proposes a statistical relationship in the form of an upper limit among two solar parameters, i.e. the CME speed and the peak SXR flux of the associated flare, and the peak proton intensity, in a similar way to Lario et. al[60].

3.2.1   The Effect of the IMF Configuration

3.2.1.1   Number of ICMEs

The total number of ICMEs (N_{ICME}) observed within a 3 days interval before and/or after each SEP event is calculated for each event, regardless of the specific geometry and classification. The events are grouped in 3 categories: N_{ICME}=0,1,2 or 3. Two events that are associated with more than 3 ICMEs, are included in the N_{ICME}=3 group. For each group of events, the logarithm of the peak proton intensity (I_{pr}) is displayed ain the form of whisker-plots/boxplots in figure 3.6. The y-axis is the $\log_{10}(I_{pr})$ and the x-axis the discrete values of N_{ICME}. The horizontal lines inside each box correspond to the $\log_{10}(I_{pr})$ value for each group and the exact value is printed above the line.

It is apparent that the proton intensity tends to reach higher values, when multiple ICMEs are present in the interplanetary space, regardless of their position at the time of the peak. This conclusion can be attributed to the more intense solar conditions, that are statistically associated to both more intense IP conditions and SEP events of higher intensities.

The relation between N_{ICME} and the parameters of the solar sources, is further investigated in figure 3.8, which shows the whisker-plots of the maximum SXR flux of the parent flare (left panel figure 3.7) and the boxplots of the speed of the primary CME (V_{CME}) (right panel figure 3.8) for each N_{ICME}. It is apparent that, events that are associated with stronger flares and faster CMEs are more likely to occur at times that multiple ICMEs are present in the interplanetary space. This is expected, as the conditions at the Sun are those that
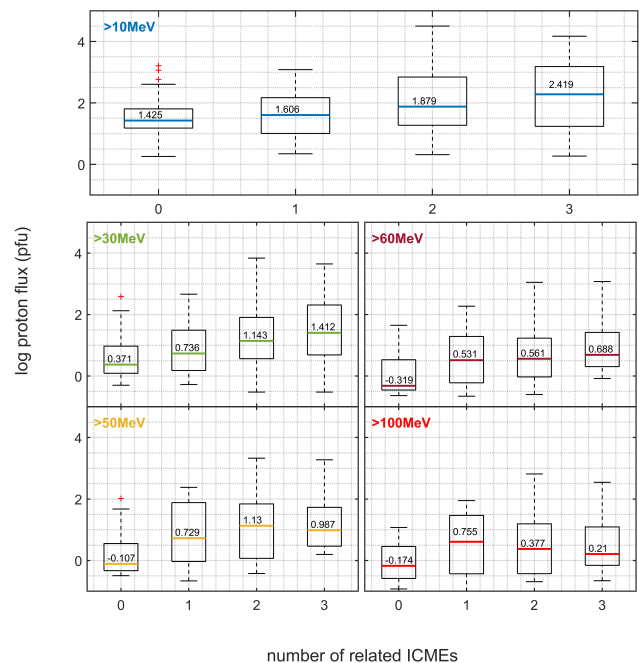
Figure 3.6: The peak proton intensity I_{pr} w.r.t. to the total number of associated ICMEs for all events, regardless of the classification

determine those in the IP space.
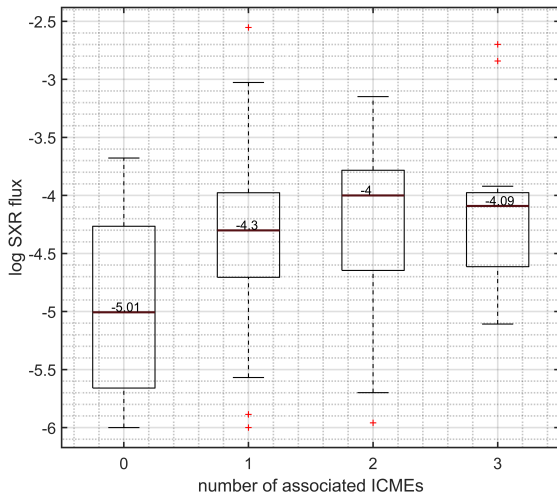
Figure 3.7: The peak SXR flux w.r.t. the number of associated ICMEs associated with each event
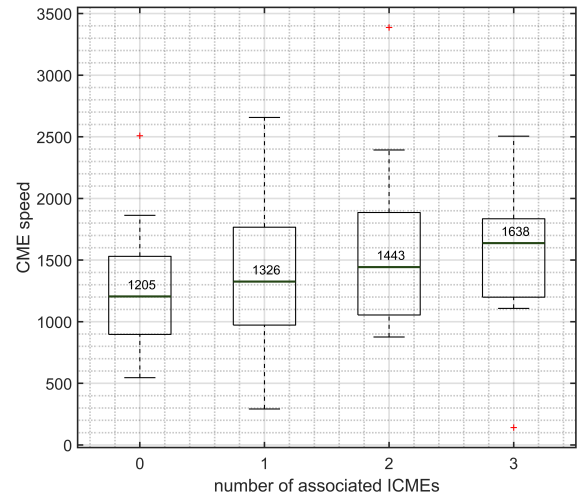
Figure 3.8: The speed of the driver CME w.r.t. the number of associated ICMEs associated with each event

3.2.1.2   The peak proton intensity per class of events

Figure 3.9 displays the whisker-plots of the peak proton intensity for each event class and MC-Pos/NoMC subcategories. The horizontal lines correspond to the logarithm of the median value of peak proton intensity (I_{pr}) at each energy channel and class/subcategory. The exact value is printed above each line. It is apparent that class 0 events exhibit lower proton intensities than the other classes. Class 2 events are associated with the lowest proton intensities at all energy channels and do not exhibit flux enhancement in the E>100MeV channel. Classes 3 and 4 are the most energetic (3.9a). Furthermore, MC and Pos/MC subcategories reach similar median peak proton fluxes(figure 3.12).

The distribution of $\log_{10}(I_{pr})$ at each energy channel is shown in figures 3.11 and 3.12 (from left to right: E>10 MeV, E>30MeV, E>50MeV, E>60MeV and E>100MeV). Figure 3.10 (panels A, B, C, D and E) shows the distribution for all events, regardless of the classification. Figure 3.11 shows the distributions of each class (for top to bottom: class 0, 1, 2, 3, 4 and 5, panels 1-30). Class 3 subcategories MC and Pos/NoMC are shown in figure 3.12 (panels 31-40). The vertical black dashed line corresponds to the mean $\log_{10}(I_{pr})$. At the top right of each panel, the mean $\log_{10}(I_{pr})$ and standard deviation are printed. The mean value of the distributions A-E (figure 3.10), is smaller for higher energies, however their standard deviations are almost equal. The class 0 distributions (panels 1-5) reach lower intensities and exhibit smaller deviations than class 1,3,4 and 5 distributions (panels 16-20 and 21-35). Class 2 events are not enough to draw a firm conclusion. Moreover, the distributions of the class 3 subcategories (figure 3.12) exhibit similar mean I_{pr} values, however the Pos/NoMC distributions can reach higher peak intensities, as their distribution has approximately a two times higher deviation than the MC distributions.

The one-sample Kolmogorov-Smirnov (K-S) test is applied to each distribution A-E, showing that all stem from normal distributions at a significance level higher than 99%.
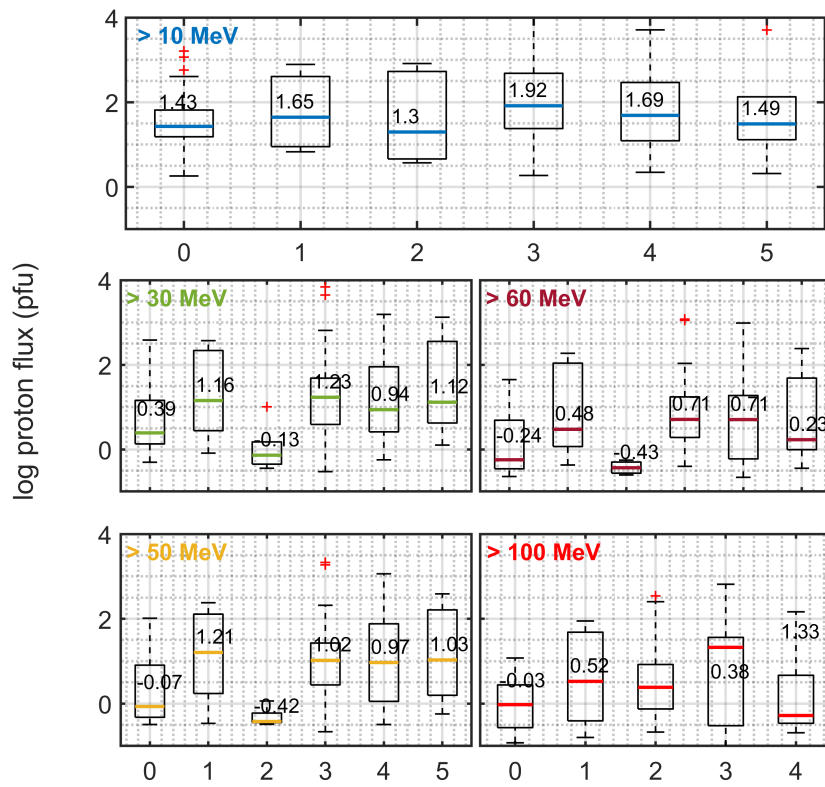
(a) Primary Classification
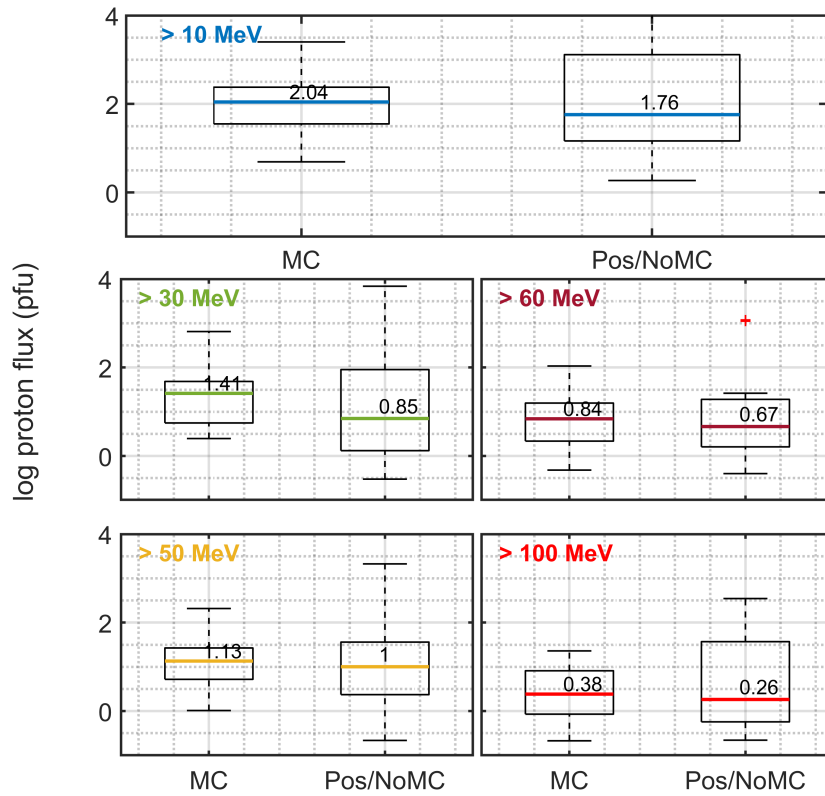
(b) Class 3 subcategories

Figure 3.9: Boxplots of the peak proton intensity per class, at each energy channel

Figure 3.10: Distribution of the peak $\log_{10}(I_{pr})$ for all events
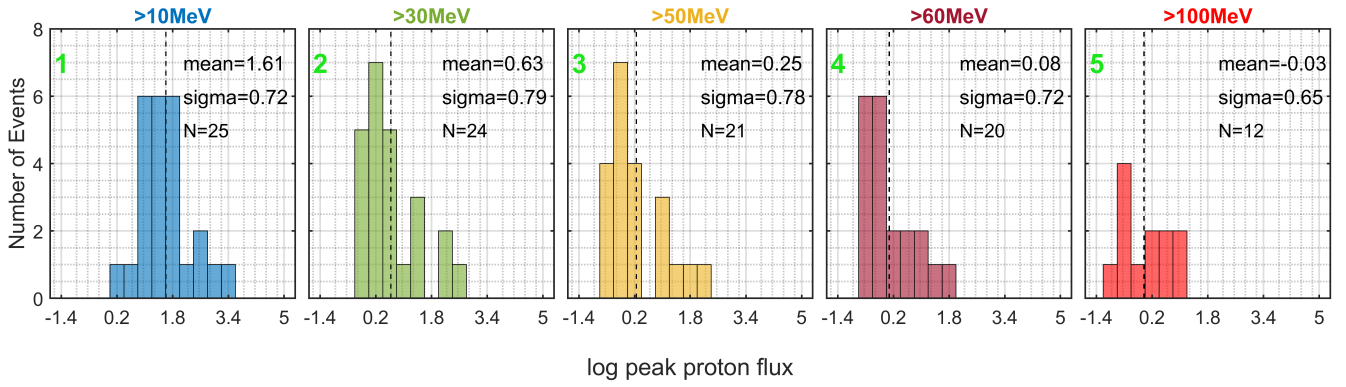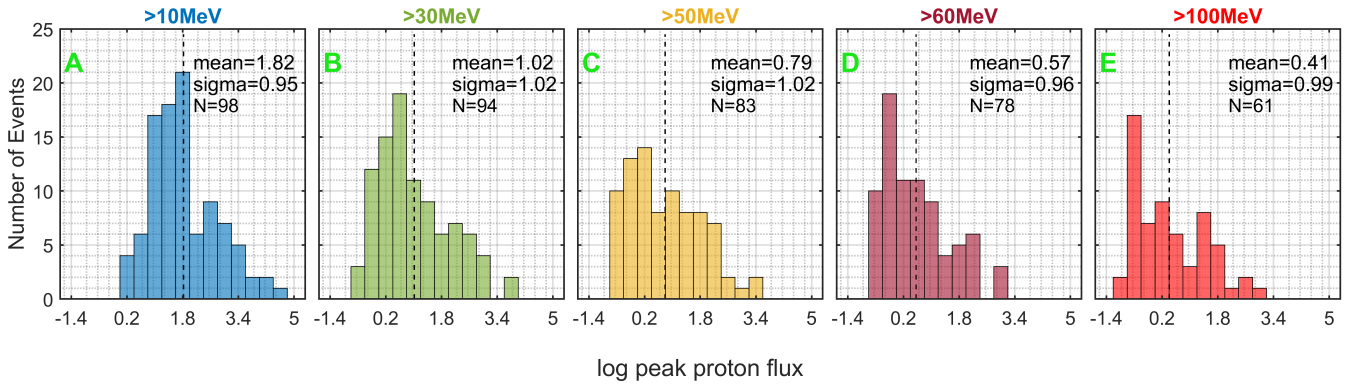
(a) Class 0
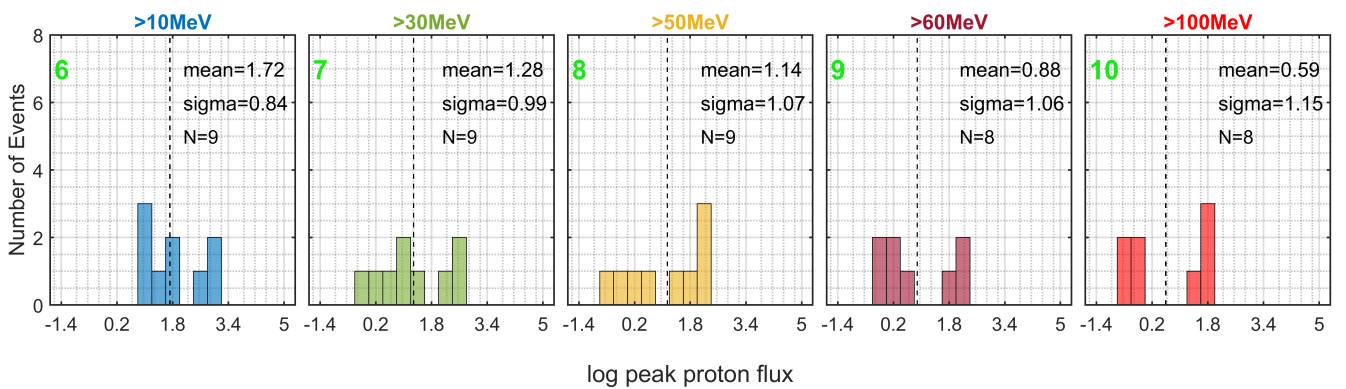
(b) Class 1

Figure 3.11: Distribution of the peak $\log_{10}(I_{pr})$ for each class (continue to the next two pages)
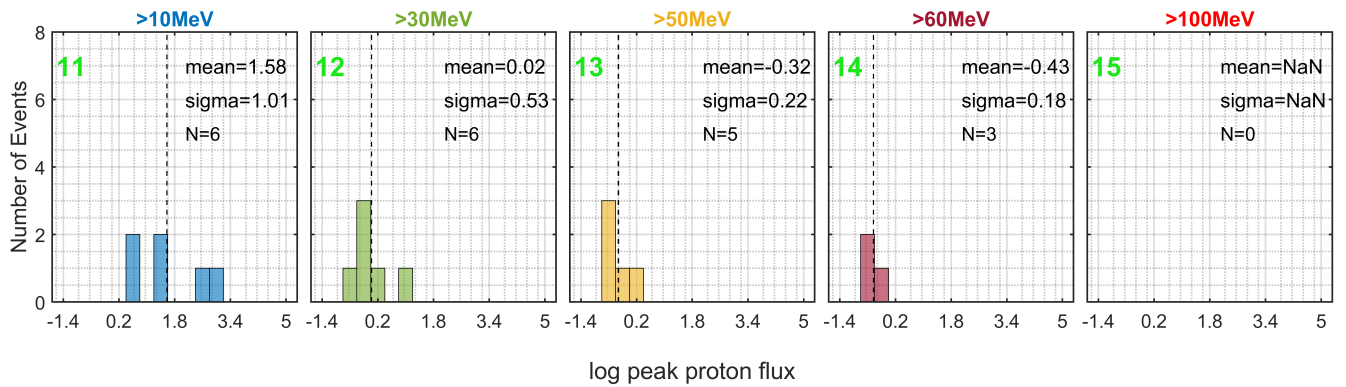
(c) Class 2
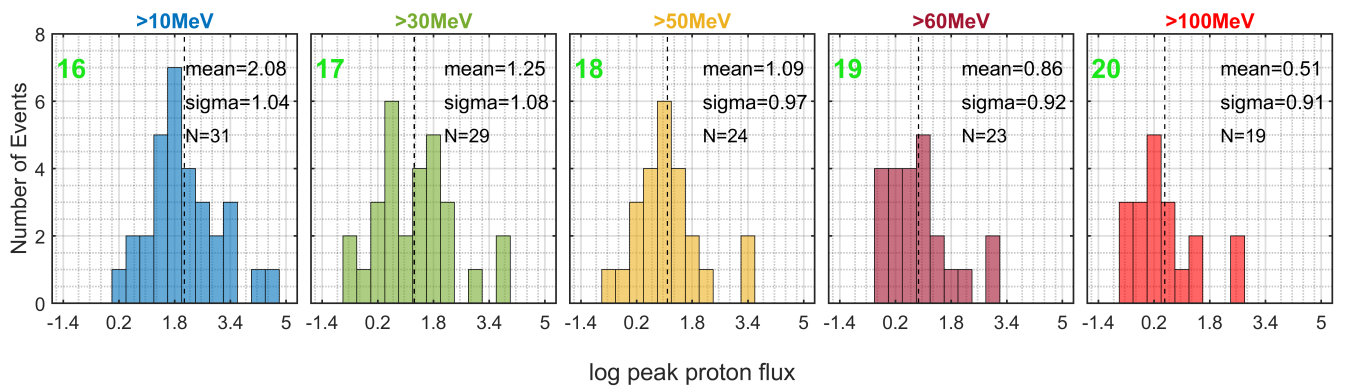
(d) Class 3
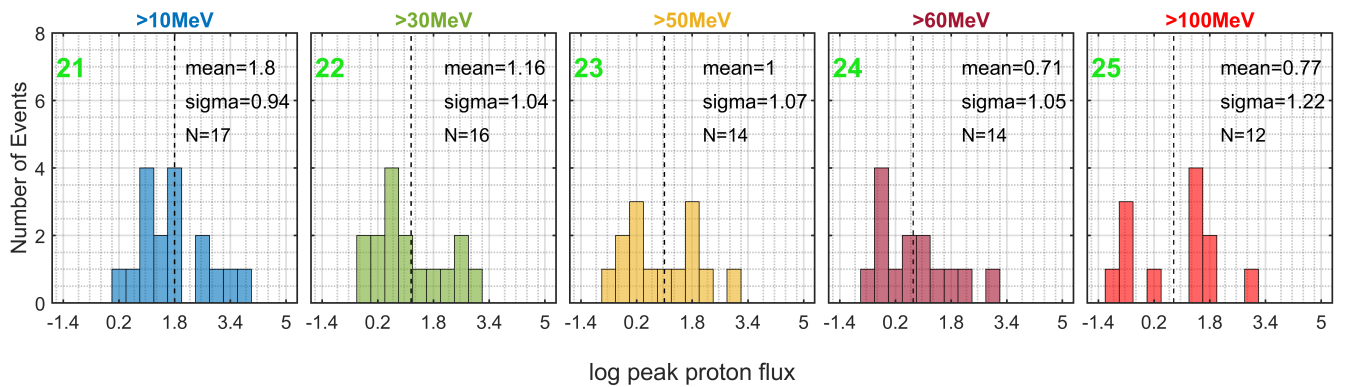
(e) Class 4

Figure 3.11: Distribution of the peak $\log_{10}(I_{pr})$ for each class (continues to the next page)
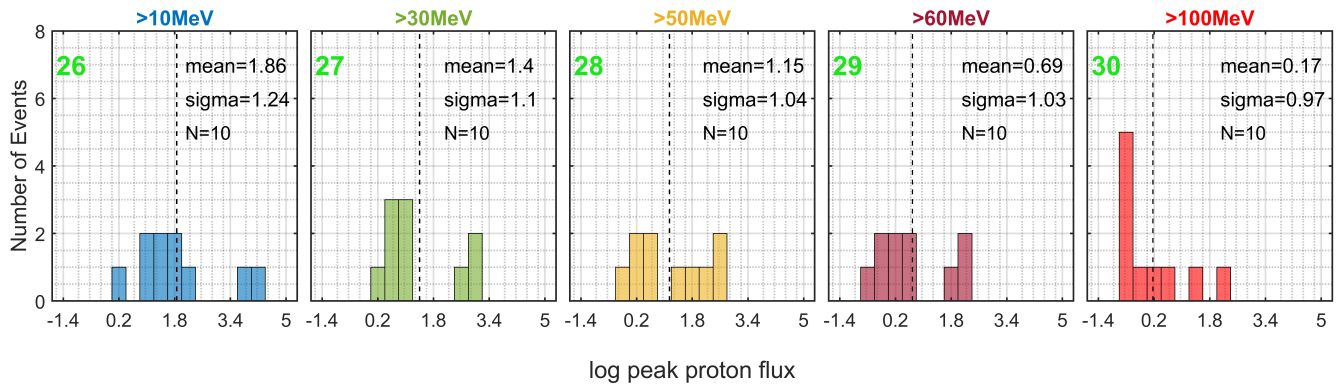
(f) Class 5

Figure 3.11: Distribution of the peak $\log_{10}(I_{pr})$ for each class (continued from the previous two pages)
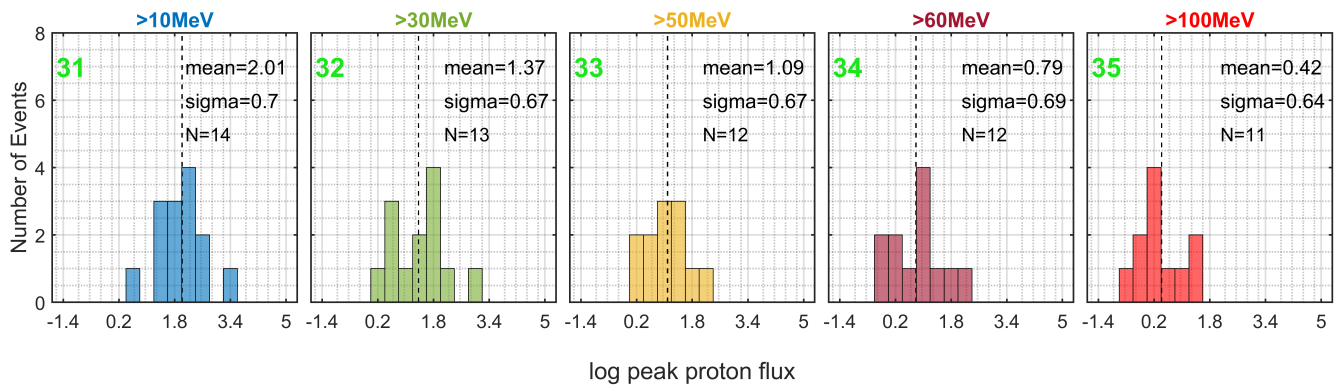
(a) MC
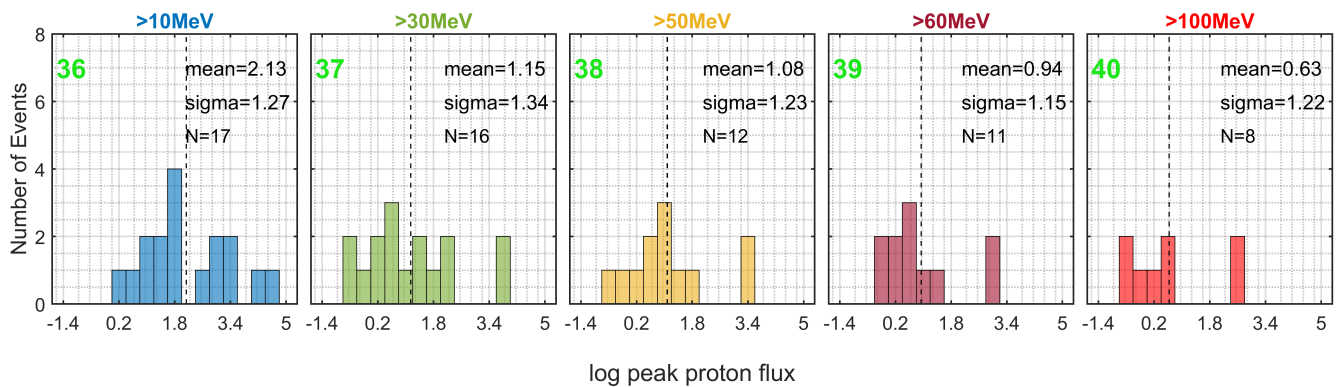
(b) Pos/NoMC

Figure 3.12: Distribution of the peak $\log_{10}(I_{pr})$ for all MC (top row) and Pos/no MC events (bottom row)

3.2.1.3   A closer look at Class 4 events

The maximum proton intensity wrt to the number of ICMEs is investigated for the class 4 events. The results are shown in figure 3.13. The two events associated with two preceding ICMEs, reach higher I_{pr} values, than the events associated with one preceding ICME. The two events are shown in figure 3.15. The enhanced proton intensity of event 70 can be attributed to the previous event (event 69, visible on figure 3.15a as a red arrow), associated with an X class flare. Event 89 (figure 3.15b) is also preceded by an SEP event, however less energetic and associated with an M class flare (this event does not belong to the SEP database (table 2.4) due to the longitudinal restriction). As already discussed in paragraph 3.2.1.1, SEP events of higher intensities and driven by more intense solar conditions are more likely to be associated with multiple ICMEs as well.

Lastly, the maximum proton intensity is plotted against the speed of the associated ICME in figure 3.14. The two events associated with two preceding ICMEs are excluded. It can be observed that, events with higher proton intensities, especially for higher energies, tend to be associated with faster preceding ICMEs, indicating faster ICMEs are generally associated with more energetic phenomena at the Sun. Moreover, shocks ahead of faster ICMEs can produce higher levels of turbulence, affecting the intensities of SEPs. Particles pre-accelerated by the fast shock of the preceding ICME can also lead to enhanced particle intensities[56]. Of course, there is a significant level of scattering of the data points, especially at higher energies, adding to the fact that there are other factors also significant.
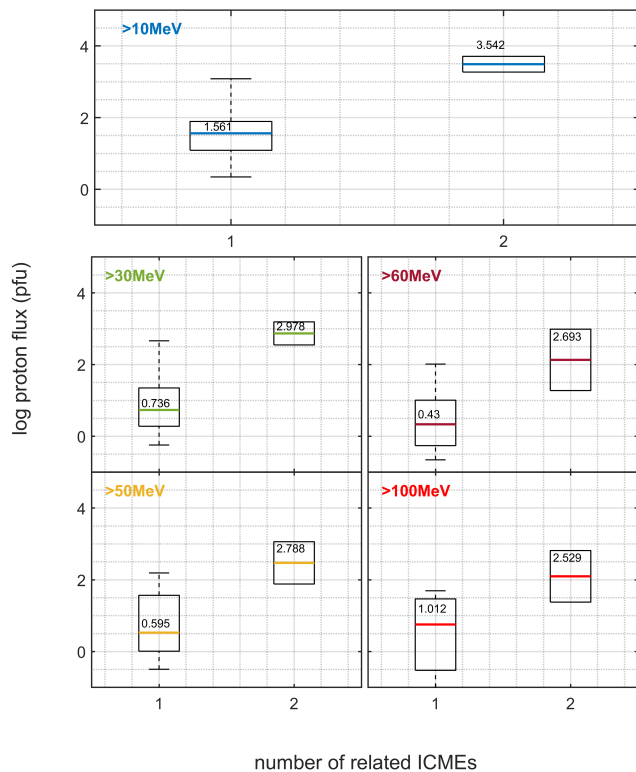
Figure 3.13: The peak proton intensity I_{pr} w.r.t. to the total number of associated ICMEs for the events of class 4
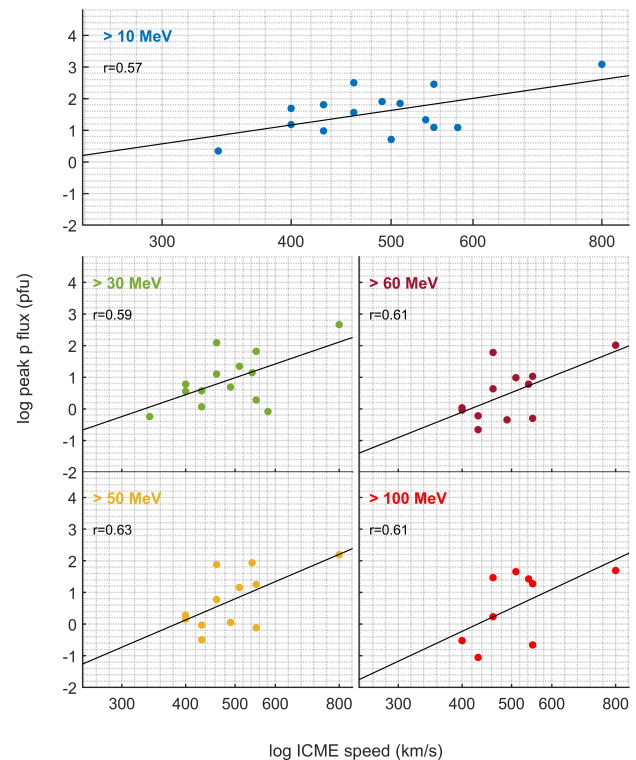
Figure 3.14: The peak proton intensity I_{pr} against the speed of the preceding ICME for the events of class 4
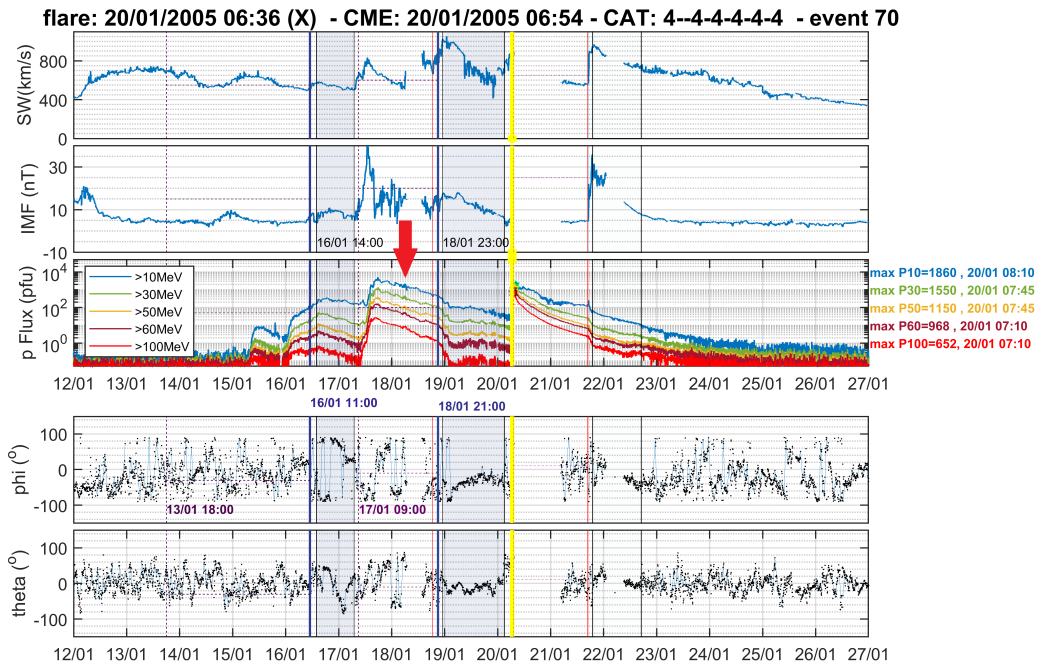
(a) event 70
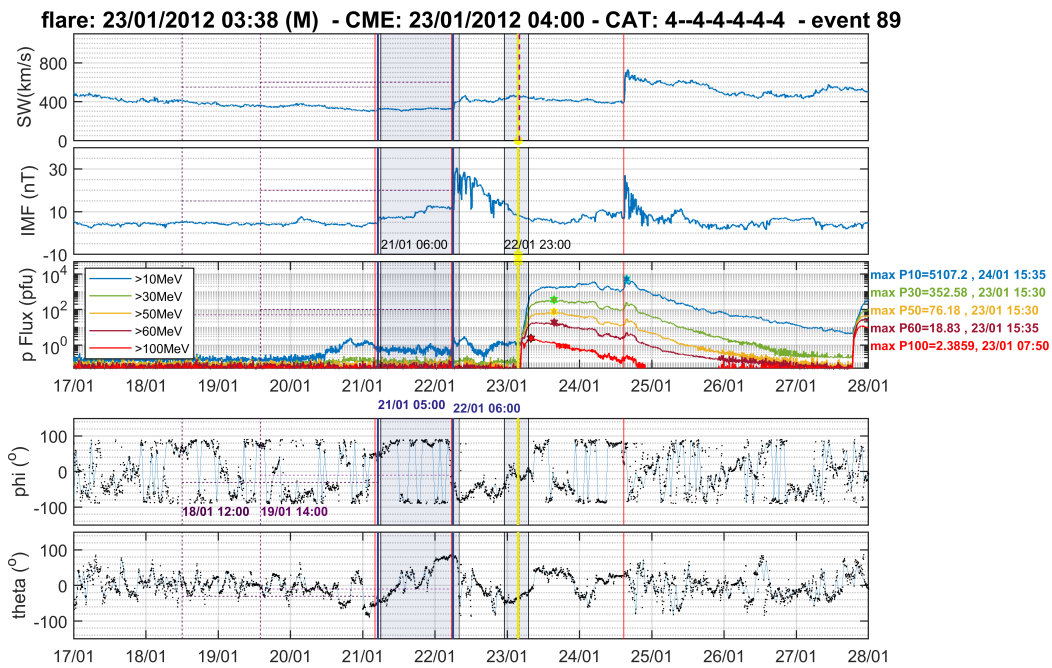
(b) event 89

Figure 3.15: The two events that are associated with 2 preceding ICMEs

3.2.2   Proton Intensity and Parameters of the Solar Activity

It is widely accepted that SEPs tend to be more energetic during periods of intense solar activity, as seen in figure 3.16. Figure 3.16a shows the peak proton intensity at each energy channel for each flare size and figure 3.16b the peak proton intensity at each energy channel against the CME type, based on the SCORE scale, proposed by Evans et al. [65]: S stands for *slow* CMEs with V_{CME}<500km/s, C for *common* CMEs with 500km/s$\leq V_{CME}$<1000km/s, O for *occasional* CMEs with with 1000km/s$\leq V_{CME}$<2000km/s and R for *rare* CMEs with $V_{CME} \geq$2000km/s. The horizontal line inside each box corresponds to the median $\log_{10}(I_{pr})$ value for each group and the exact value is printed above the line. It is evident that, large flares and fast CMEs are most likely to drive intense SEP events, at all energies.
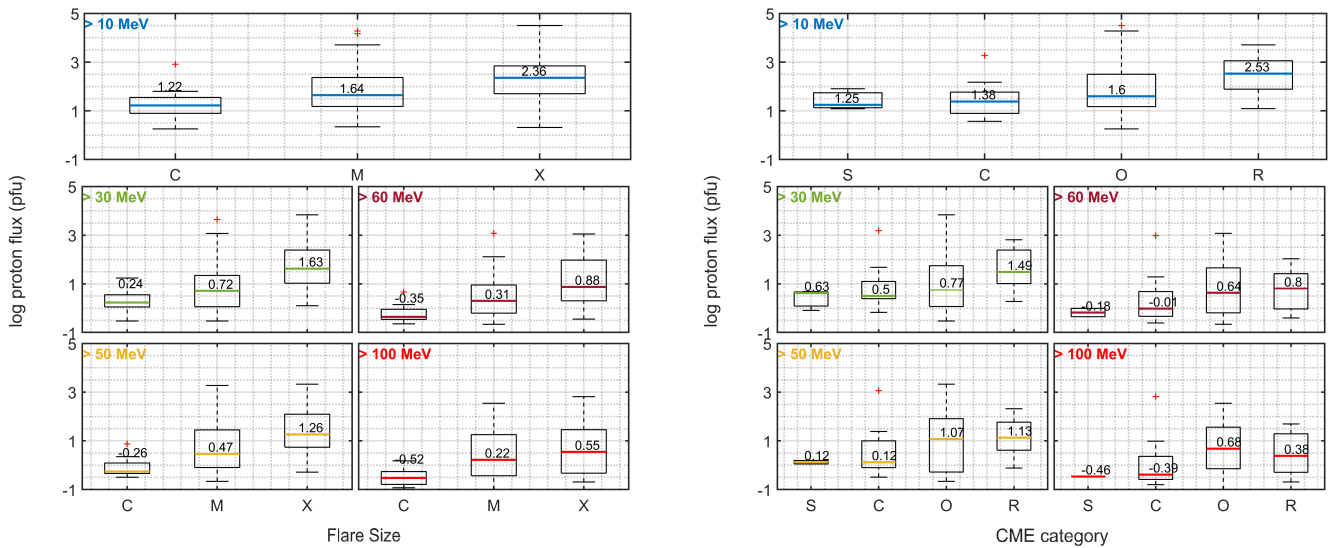
(a) Boxplots of the peak proton intensity against the size of the associated flare

(b) Boxplots of the peak proton intensity against the speed of the associated CME

Figure 3.16: SEP peak proton intensity wrt to the main solar parameters

The following paragraphs present the construction of *triangular distributions* between the peak proton intensity (I_p) and both the speed of the driver CME (V_{CME}) and the peak SXR flux of the associated flare (I_{SXR}). The approach is adopted by Lario et al. [60] and is more suitable compared to a linear correlation, as the significant level of scattering among the parameters (up to 3-4 orders of magnitude paragraph 1.3.1.4) makes a linear prediction almost impossible. On the other hand, the triangular distributions define an *upper limit* of the peak proton intensity of a SEP event, for a given CME speed/SXR flux.

3.2.2.1   Peak Proton Intensity - CME Speed

The upper limit is calculated as the linear regression of the outer points of the $\log_{10}(\nu)$-$\log_{10}(I_p)$ scatter plot (figure 3.17) so that, for a given ν:

$$log_{10}(I_p) \leq \alpha \cdot log_{10}(\nu) + const \tag{3.2.1}$$

and for the line y=$f(\nu)$

$$y \sim \nu^{\alpha} \tag{3.2.2}$$

Figure 3.17 is the $\log_{10}(\nu)$-$\log_{10}(I_p)$ scatter plots of all events regardless of the classification for each energy channel. Each panel corresponds to an energy channel, from top to bottom: E>10MeV, E>30MeV, E>50MeV, E>60MeV, E>100MeV. The value α is printed on each panel. It is apparent that, as the energy interval of protons is shortened, α decreases.

Figure 3.18 shows the $\log_{10}(\nu)$-$\log_{10}(I_p)$ scatter plot and upper limit line, as well, however each flare size is plotted individually. C-flare events are labeled as '$\triangle$', M-flare events as '$\square$' and X-flare events as '$*$'. C-flare events are far below the line, as events associated with C flares statistically are less energetic and driven by slower CMEs. Events associated M and X flares follow the upper limit trend.

The triangular distributions are calculated for each energy channel and class 3 subcategories MC-Pos/NoMC, as well. The upper limit for each class (expect for classes 2 and 5) and class 3 subcategories MC and Pos/NoMC is calculated as described above (Equation 3.2.1), so that for the line y'=$f(\nu)$:

$$y' \sim \nu^{\beta} \tag{3.2.3}$$

The first four rows of figure 3.19 show the $\log_{10}(\nu)$-$\log_{10}(I_p)$ scatter plot for each energy channel and class. From left to right: E>10MeV, E>30MeV, E>50MeV, E>60MeV, E>100MeV, and from top to bottom: class 0, 1, 3 and 4 (classes 2 and 5 are not shown), MC, Pos/NoMC. The coefficients α (black) and β (blue) are printed on each

Energy Channel E>	10MeV	30MeV	50MeV	60MeV	100MeV
α	7.16	6.66	6.29	5.93	4.97
Class 0-β	4.23	3.90	3.34	2.82	1.79
Class 1-β	4.43	4.56	4.61	4.87	4.91
Class 3-β	8.01	8.09	7.71	7.26	6.28
Class 4-β	5.50	4.60	4.62	5.40	5.55
MC-β	3.02	2.96	2.54	2.12	1.94
Pos/NoMC-β	12.88	17.15	18.38	20.23	27.82

Table 3.3: Coefficients α and β of the upper-limit lines

panel. For class 0 $\beta<\alpha$, indicating that for a given CME speed, events not associated with ICMEs, are expected to reach lower peak proton intensities that average. On the other hand, for class 3 β is the largest amongst all classes, meaning that events occurring in the vicinity of an ICME, reach the highest intensities for a given CME speed. The second highest β values are those of class 4. Class 1 events have small β value, close to class 0. Moreover, β values of Pos/NoMC events are significantly larger compared to the values of MC events, meaning that events occurring within an ICME with a magnetic cloud configuration reach lower intensities.

Note that, class 0 and 3 β values follow the decreasing tendency of α, while class 1 β values are increasing. Class 4 β values do not have a decreasing or increasing tendency. Moreover, the upper limit line of MC events is flattened as the energy interval is shortened ($\beta \downarrow$), while Pos/NoMC events exhibit the opposite behavior. The lack of a decreasing tendency in some cases can be attributed to the low statistical samples and the errors stemming from the subjectivity of the method.
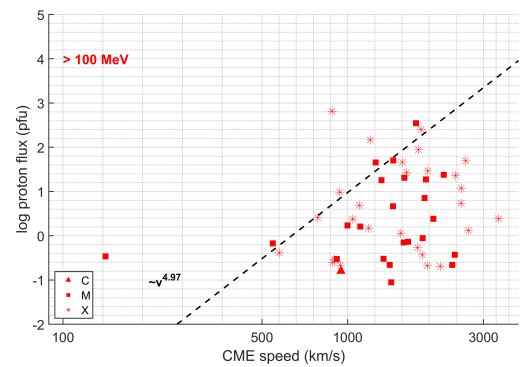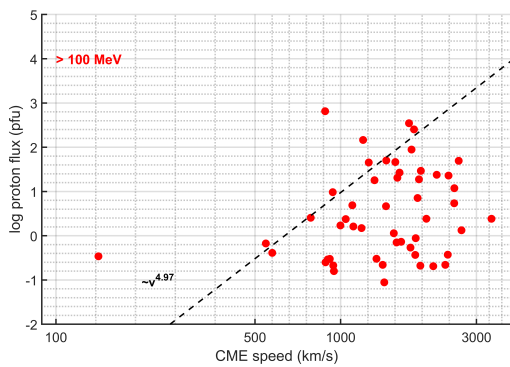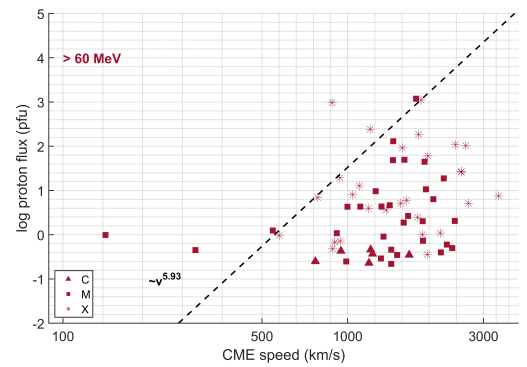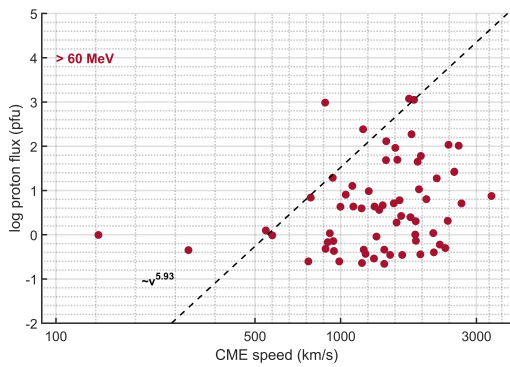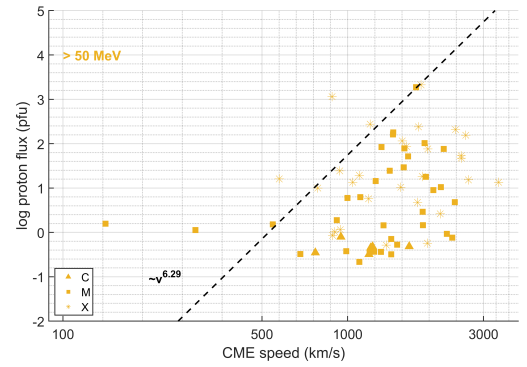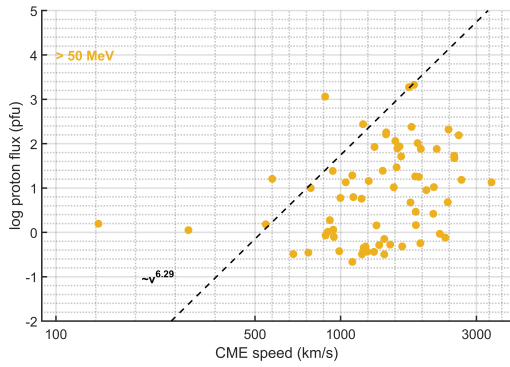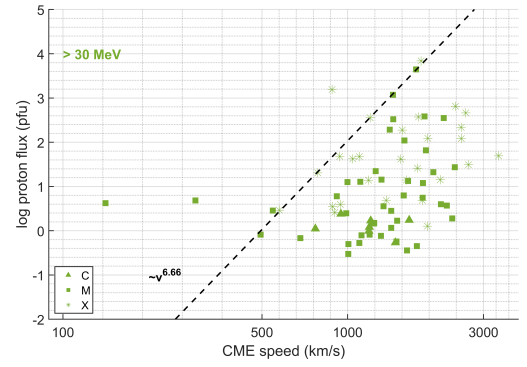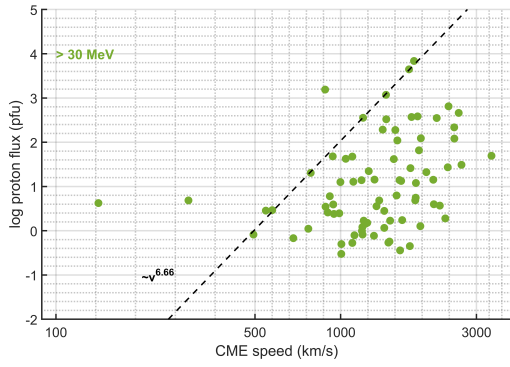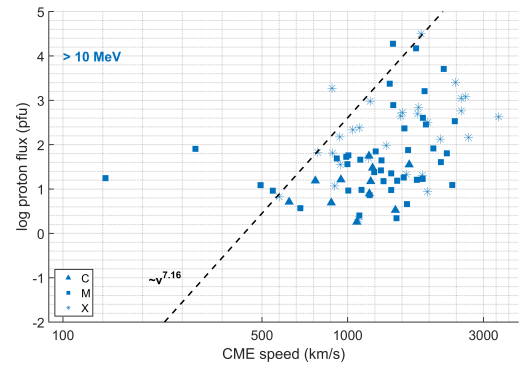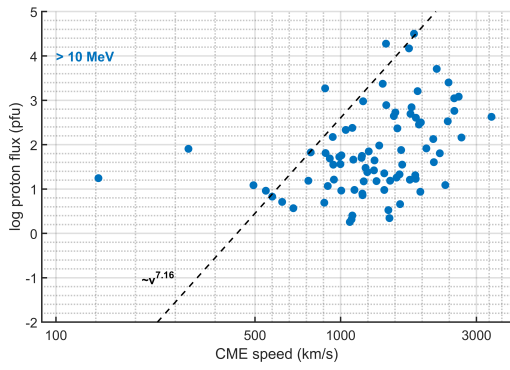
Figure 3.17: Upper limit I_p-ν for all events

Figure 3.18: Upper limit I_p-ν for all events per flare size
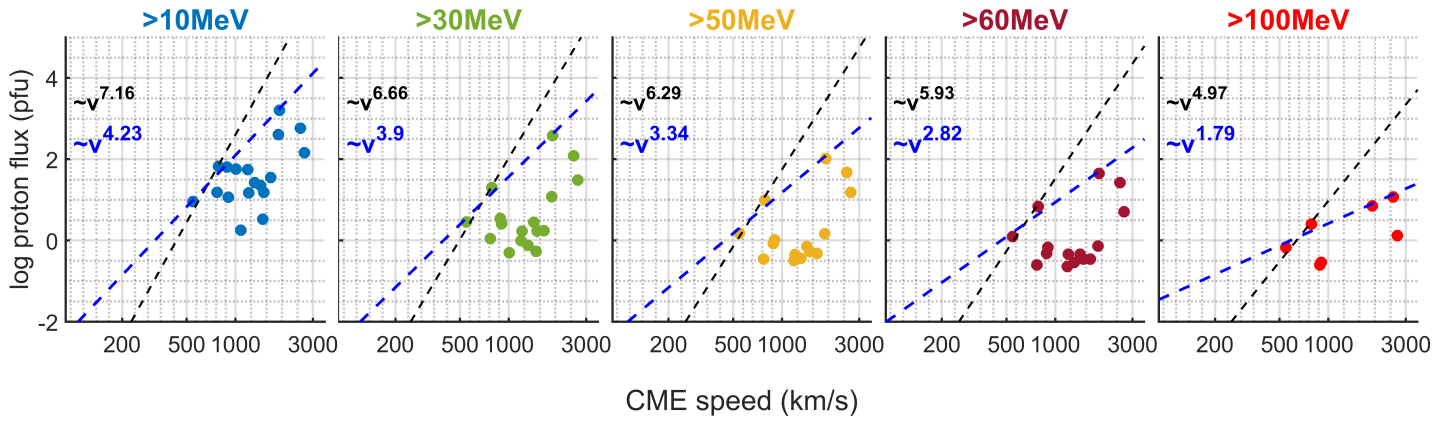
(a) Class 0
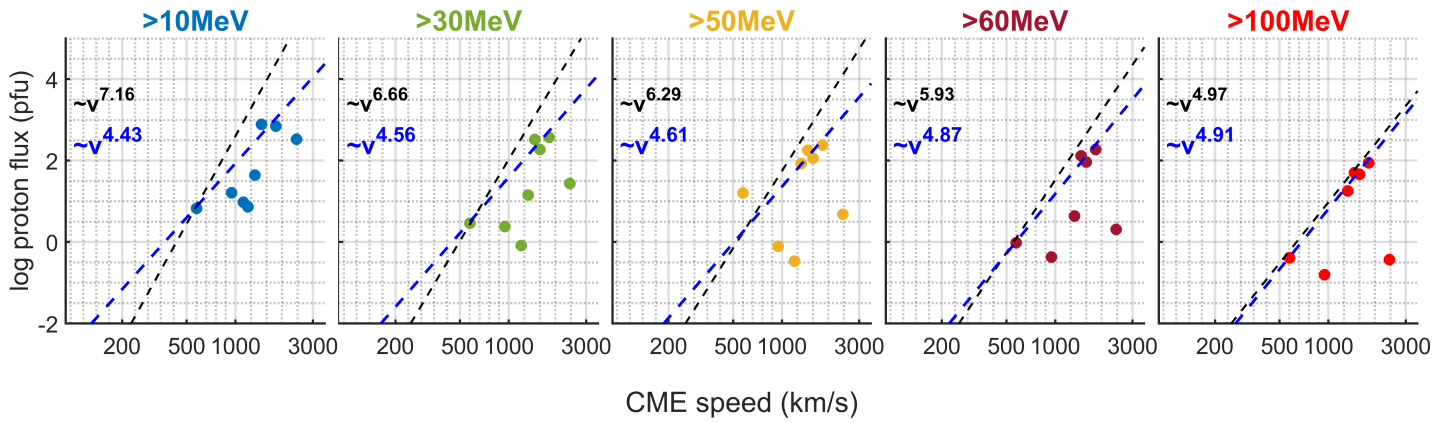
(b) Class 1
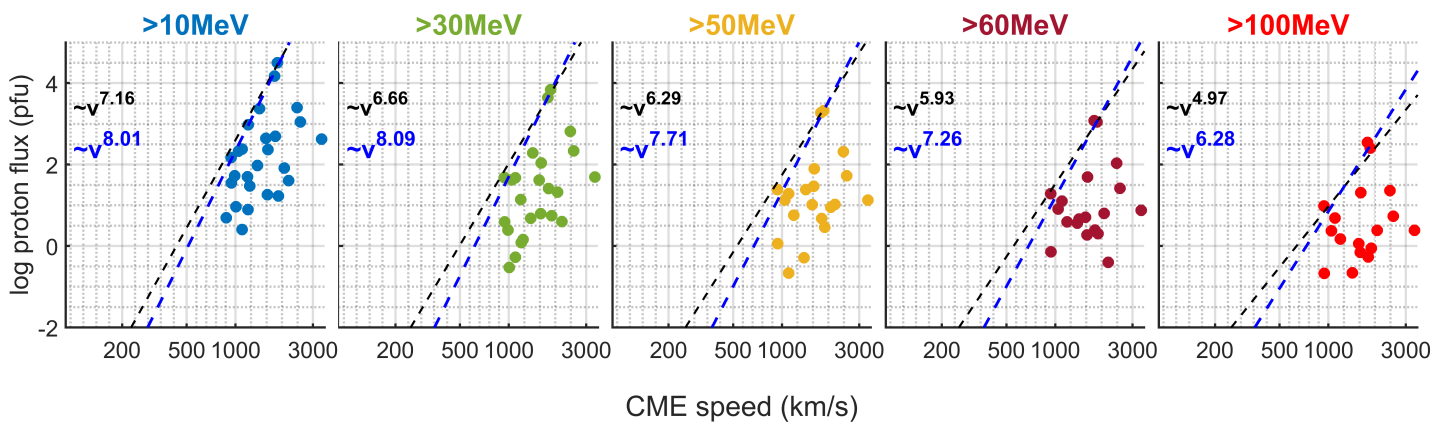
(c) Class 3

Figure 3.19: Upper limit I$_p$-ν for each class
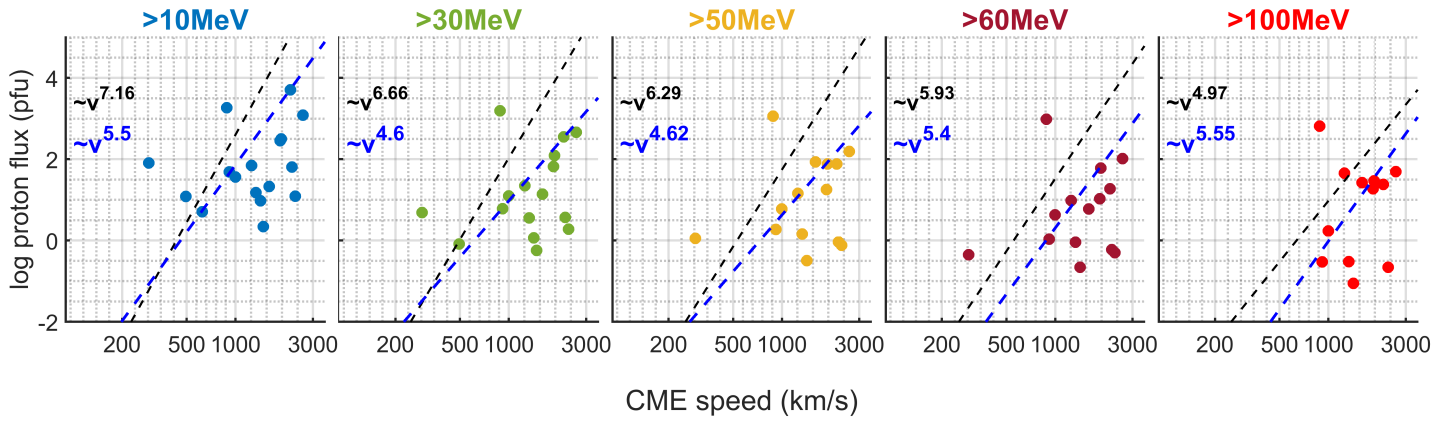
(d) Class 4
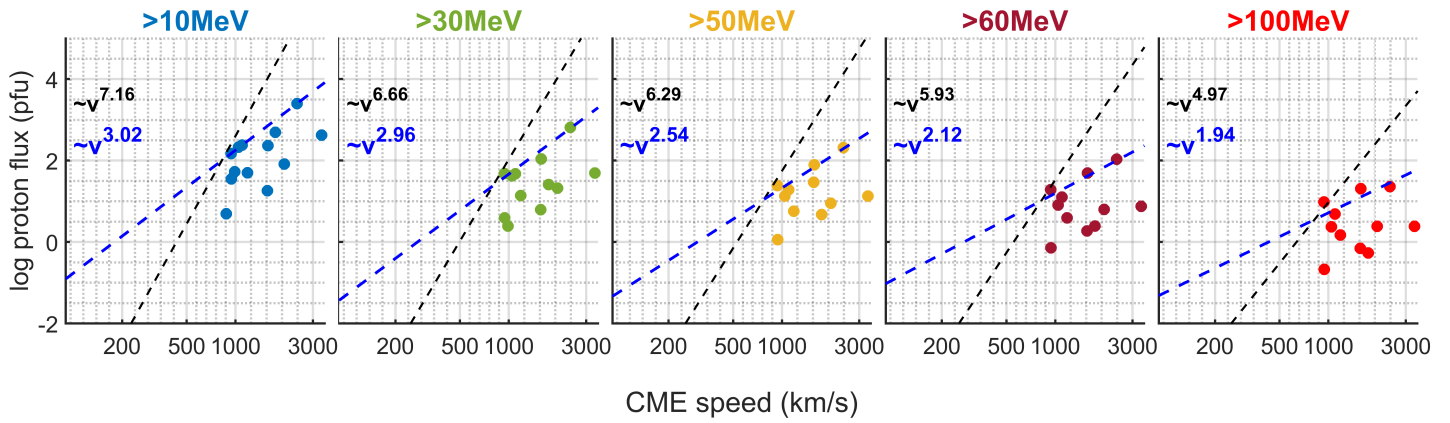
(e) MC
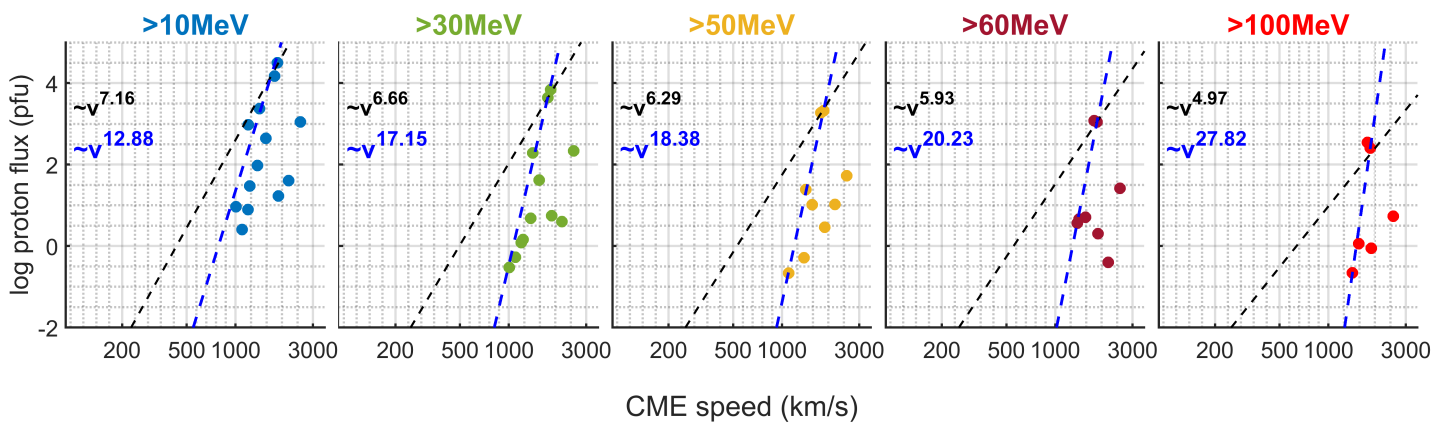
(f) Pos/NoMC

Figure 3.19: Upper limit I_p-ν for each class continued from the previous page

3.2.2.2   Peak Proton Intensity - Flare Size

Figure 3.20 displays the scatter plots of the SXR intensity of the flare I against the peak proton intensity I_p, regardless of classification for each energy channel. Each panel corresponds to an energy channel, from top to bottom: E>10MeV, E>30MeV, E>50MeV, E>60MeV, E>100MeV.
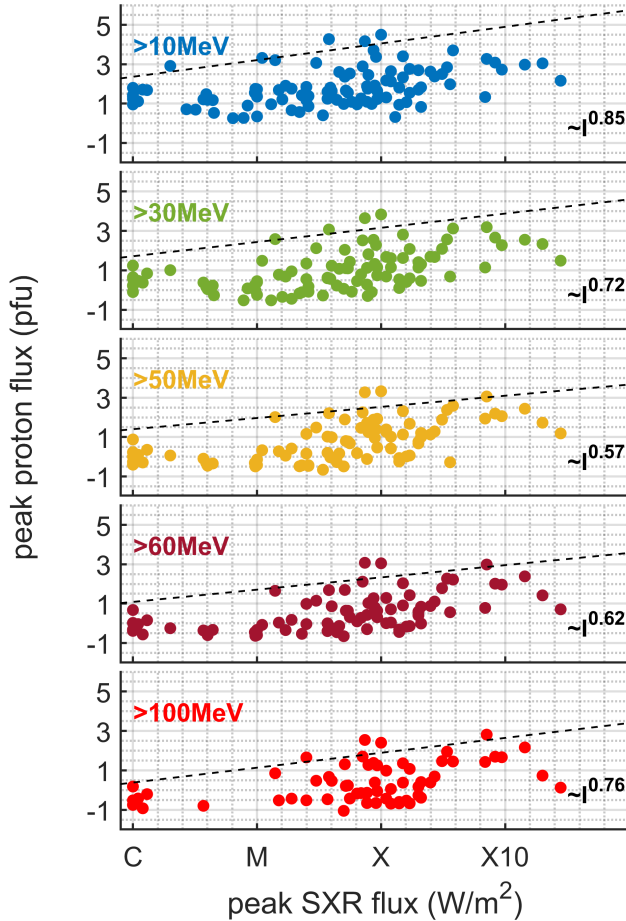
Figure 3.20: I_p-I upper limit for all events

An upper limit is calculated, similarly to the process described in the above paragraph (paragraph 3.2.2.1). The line is calculated as the linear regression of the outer points of the $log_{10}(I_p)$-$log_{10}(I)$ scatter plot, so that:

$$log_{10}(I) \leq c \times log_{10}(I_p) + const \quad (3.2.4)$$

and the upper limit line is:

$$y \sim I^c \quad (3.2.5)$$

However, no significant difference between the energy channels is observed, as the c values are almost the same. The above process is repeated for each class (expect for class 2 and class 5, due to their low sample,) for the >10MeV energy channel, so that the upper limit line is:

$$y' \sim I^{c_1} \quad (> 10MeV) \quad (3.2.6)$$

.

We observe that, for a given flare, class 3 and class 4 events reach higher proton intensities, compared to class 0. MC events reach lower intensities, compared to Pos/NoMC events, for a given flare. Class 0 and class 1 have almost similar values, that are the lowest.

Energy Channe E>	c coefficient	c_1 coefficient (> 10 MeV)	
		Class 0	0.59
10 MeV	0.85	**Class 1**	0.52
30 MeV	0.72	**Class 3**	1.47
50 MeV	0.57	**Class 4**	1.98
60 MeV	0.62	**MC**	0.88
100 MeV	0.76	**Pos/No MC**	1.91

Table 3.4: Coefficients c and c1 of the upper limit lines
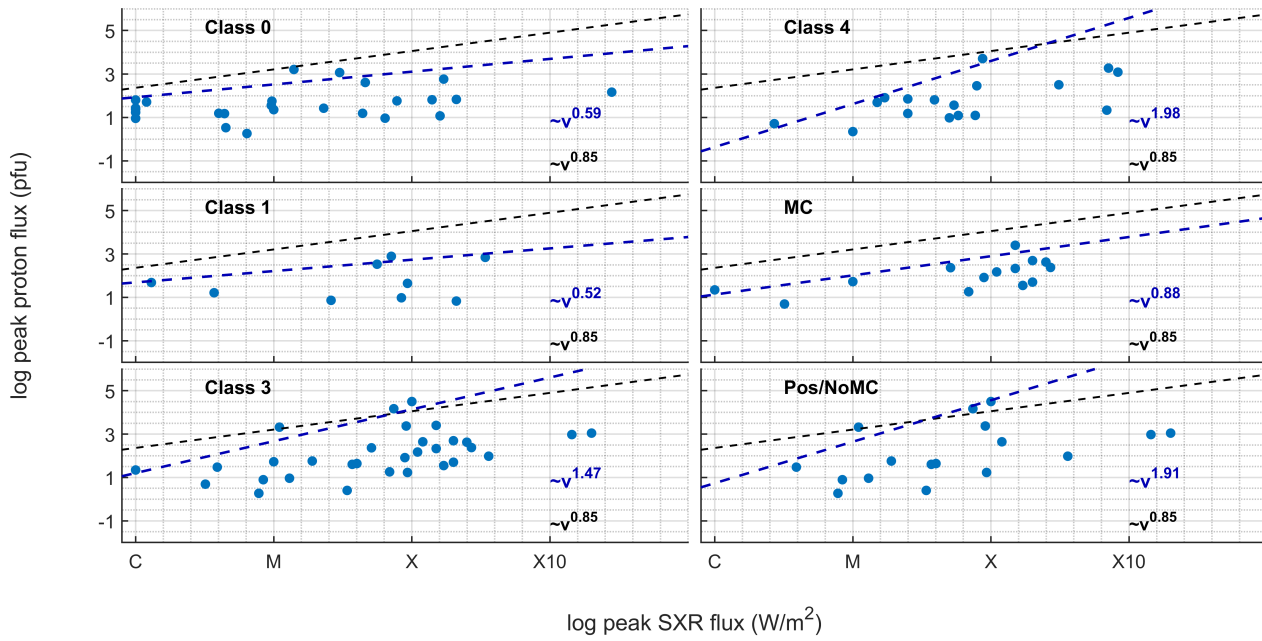
Figure 3.21: I_p-I upper limit for each class (E>10 MeV protons)

3.3   Spectral Analysis

In the limited energy range used in this study, the integral spectrum can be represented in a power law form [49]:

$$I_p = I_{p,0} \cdot E^{-\gamma} \tag{3.3.1}$$

where I_p is the proton intensity, E the corresponding energy, γ the spectral index and $I_{p,0}$ a constant. Equation 3.3.1 is fitted to the E-I_p scatter plot of each event (figure 3.22). The number of points used depends on the number of energy channels that exhibit flux enhancement. Events that only exhibit flux enhancement in the >10MeV energy channel (4 events) are excluded.

The distribution of the 94 γ values is shown in figure 3.23 and the distributions per class and the MC-Pos/NoMC subcategories in figure 3.24a. The most frequent value of the distribution of all events, as well as of class 0 and class 3 events, is 1.5. However, class 3 events exhibit a much clearer peak around this value and spread to smaller and larger values. Most class 4 events are located in the left part of the distribution, which corresponds to the hard part of the spectrum.

Most MC and Pos/No MC events have γ=1.5 and γ=1.7 correspondingly (figure 3.24b). MC events extend to smaller values while Pos/NoMC events extend to higher values up to 3.9.

Figure 3.25 shows the relationship between the peak SXR flux of the flare (I_{SXR}) and the γ coefficient. The scatter plot I_{SXR}-γ is displayed in figure 3.25a and the corresponding boxplots are shown figure 3.25b. It is apparent that stronger flares are associated with smaller γ values, as they are mostly associated with more intense SEP events.
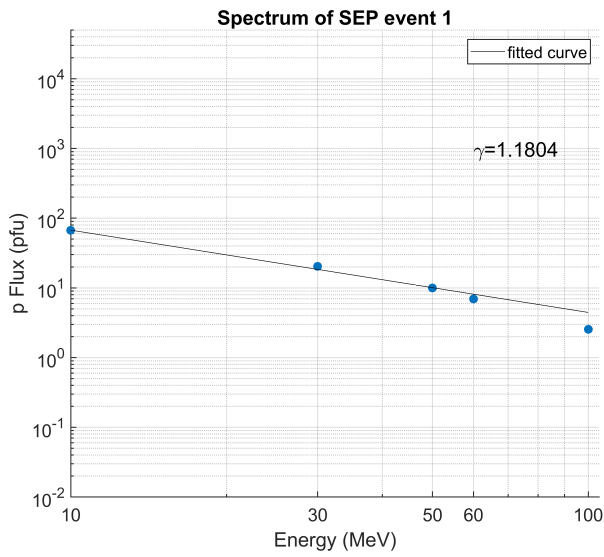
Figure 3.22: Example of the energy-peak proton intensity scatter plot. The fitted line is Equation 3.3.1
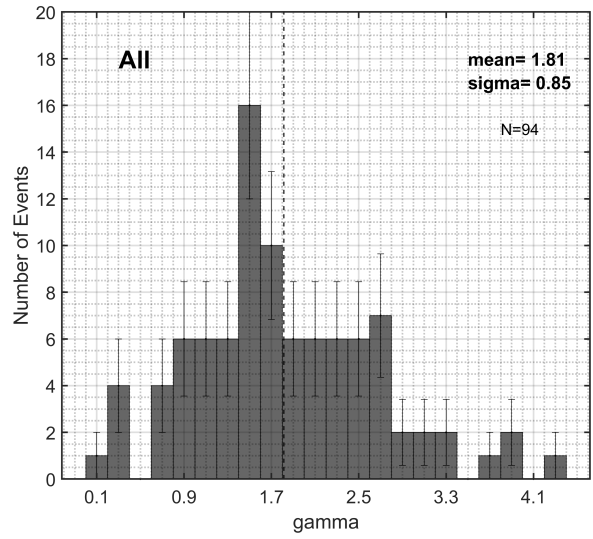
Figure 3.23: The spectral distribution of all events

(a) each class
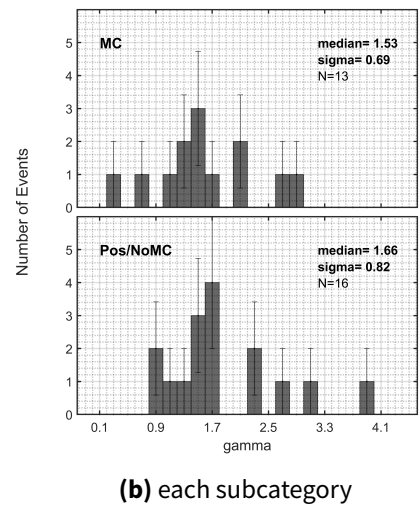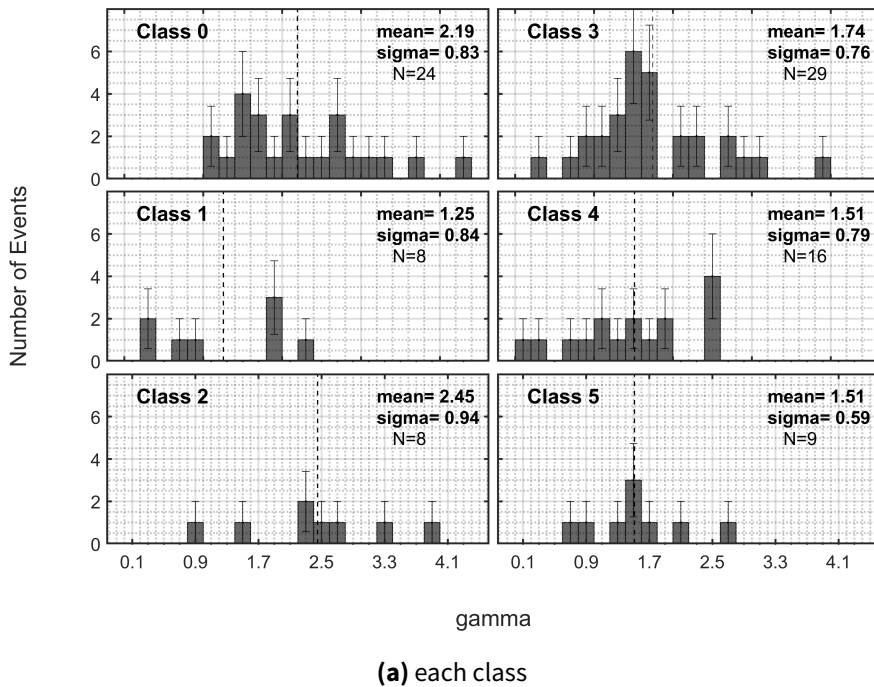
(b) each subcategory

Figure 3.24: Distribution of the γ index for each event class and subcategory
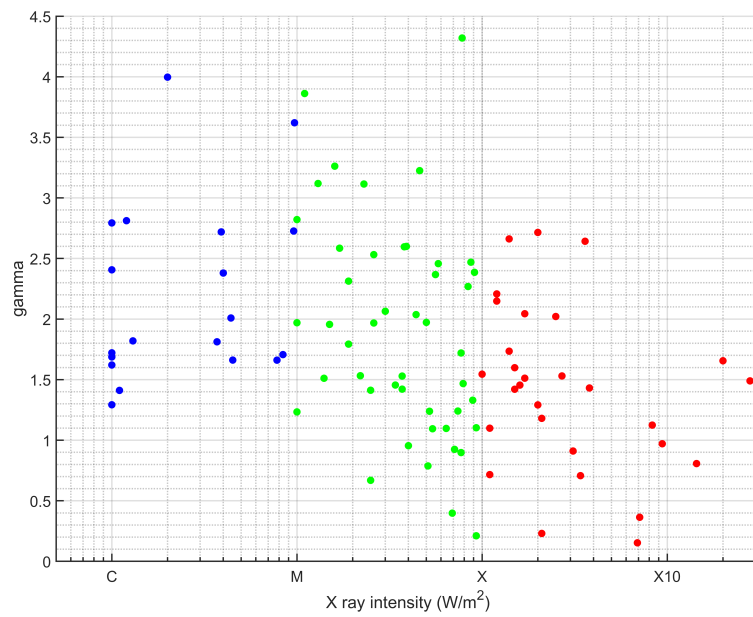
(a) γ index - peak SXR flare flux
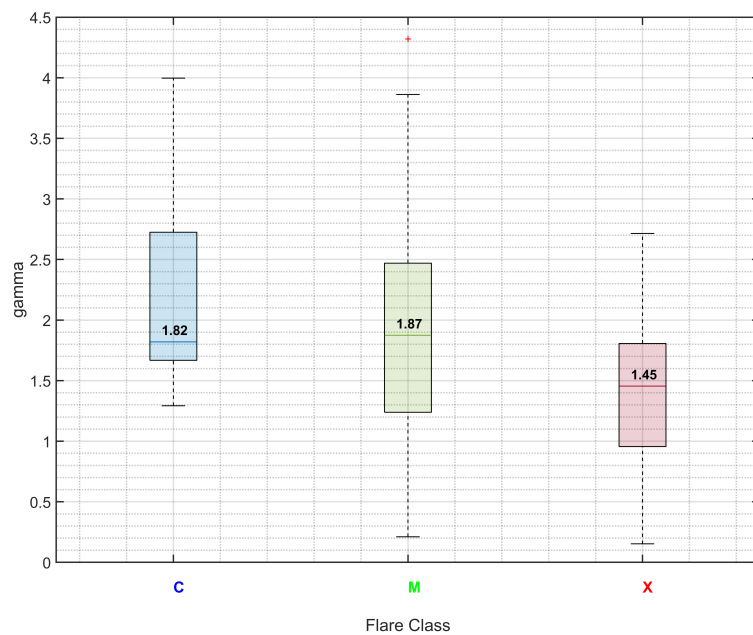
(b) γ index - peak SXR flare flux boxplots

Figure 3.25: Relation between the γ index of the proton energy spectrum and the maximum SXR flux of the associated flare

4   DISCUSSION

This section summarizes the main results stemming from the above statistical analysis.

4.1   The distribution of classes

In summary, the classification reveals that most events ($\sim$31%) are observed when Earth is immersed within an ICME (class 3), in agreement with several similar studies [16],[66]. Events occurring within the standard solar wind (class 0) are the second most common (26%), while 17% occur shortly after an ICME has passed Earth (class 4). Events occurring before a following ICME passes Earth (class 1) and events observed in the sheath region of an ICME (class 2) events are equally the least common (8% each). Generally, $\sim$74% of all events are more likely to be associated with ICMEs, regardless of the specific geometry (figure 2.3).

Not all events exhibit flux enhancement in all or in most energy channels. More specifically, 4% of the 98 events exhibit flux enhancements only in the E>10MeV energy channel and 15 % in the E>10MeV and E>30MeV energy channels. 20% of all events do not exhibit flux enhancement in the E>60MeV and E>100 MeV energy channels, while 38% in all channels except E>100MeV.

Furthermore, not all classes follow the above percentage distribution per energy channel. Most of class 3 and 4 events exhibit flux increases in all energy channels, revealing that they are statistically more energetic. Class 5 events have flux enhancements in all energy channels, indicating that they are the most energetic, as they are mostly associated with X flares (table 1.1) and multiple ICMEs are generally associated with the most energetic solar phenomena (see paragraph 3.2.1.1). On the other hand, most class 0 events do not exhibit flux enhancement above 100MeV. It is noteworthy that class 2 events do not exhibit flux enhancement protons above 100MeV at all.

The secondary classification of class 3 events is performed, in order to investigate whether the different magnetic topology of the ICME could affect the SEP profiles. Generally, MC events are slightly less common (47%) than Pos/NoMC (53%). However, their distribution changes for narrower energy intervals: the percentage of Pos/NoMC events is smaller than the corresponding one of MC events for energies >60MeV and >100MeV (figure 2.3). This can be attributed to the fact that, MC events are mostly associated with X flares, while Pos/NoMC events with M flares (figure 3.1).

The distributions of the flare size (figure 3.1) for each class reveal that most Class 0 events are associated with flares of class C. Most class 1,2 and 4 events are associated with M flares and class 5 events with X flares. Class 3 events are equally associated with both M and X flares.

The distributions of the CME speed (figure 3.2) per class do not show a significant difference between them, as the mean CME speed values ($\bar{V}_{CME}$) among the classes are not significantly different. However, $\bar{V}_{CME}$ is slightly lower for class 0 events than class 3 and 4 events and class 3 and 4 can spread to both lower and higher V$_{CME}$ values, as they have larger standard deviations.

Finally, figure 3.3 shows the longitudinal distribution of the events for each class. It is apparent that class 0 events originate mostly at western longitudes, with a clear peak in the interval [90°,100°),

indicating that are more likely to follow the nominal Parker spiral. On the other hand, SEP events associated with ICMEs are scattered across all longitudes, suggesting that ICMEs can alter the path of particles. It should be noted, however, that deviations from the western-longitude picture exist for class 0 as well. This is not unexpected, because ICMEs are not the only factor affecting the transport of SEPs, as the driver CME can also cause the transport of particles across the field lines. Furthermore, the speed of the solar wind alters the spirals and other structures, such as CIRs, could play a role (see paragraph 1.1.3.3 and subsubsection 1.3.3).

4.2   Correlations of Solar Parameters

Despite a certain degree of scatter, there is a correlation between the logarithm of the primary CME speed (V_{CME}) and the logarithms of the SXR flux (I_{SXR}) and fluence (J_{SXR}) of the associated flare (subsubsection 3.1.2). The regression coefficient is 0.30 for $\log_{10}(V_{CME})$-$\log_{10}(I_{SXR})$ and 0.37 for $\log_{10}(V_{CME})$-$\log_{10}(J_{SXR})$, for all events. The correlation is stronger for the $\log_{10}(V_{CME})$-$\log_{10}(J_{SXR})$ relationship. Both the correlations are important at a 99% CI (table 3.2).

Physically, it is expected that the interplanetary conditions should not affect the conditions at the solar corona. Despite this, the difference between the classes is significant and the errors are bigger than the error corresponding to the correlation of all events (table 3.1), possibly due to the low statistical samples. As already discussed, the errors stem primarily from the *projection effect*: V_{CME} is not the *actual* speed of the CME, but its projection onto the plane of sky. Moreover, the calculation itself as well as other types of errors, such as instrument reading, could possibly affect the results.

A similar study is performed by Miteva et al. [16], who found a slightly larger correlation coefficient for the $\log_{10}(V_{CME})$-$\log_{10}(I_{SXR})$ relationship (r=0.39 for all events). They also limited the sample data to events with faster CMEs (>600 km/s) and flares at western longitudes and brought the correlation coefficients of the classes closer to each other. This process was not repeated here, due to low statistics.

4.3   Proton Intensity

The statistical analysis of the proton intensities of the 98 SEP events is approached in several ways. The main purpose is to estimate how and in what degree the different solar and IP conditions affect the particle intensities observed at 1AU. The methods of statistical analysis applied are:

* Distributions of the peak proton intensity for all events (figure 3.10), for all classes (figure 3.11) and both MC-Pos/NoMC subcategories (figure 3.12), per each energy channel.
* Whisker-plots of the peak proton intensity against the solar parameters (figure 3.16), for all classes and both MC-Pos/NoMC subcategories (figure 3.9- subsubsection 3.2.2).
* Whisker-plots of the peak proton intensity and solar parameters against the number of associated ICMEs within a 3-days interval (figure 3.6, figure 3.7, figure 3.8- paragraph 3.2.1.1).
* The statistical relationship between the peak proton intensity of class 4 events with the number of preceding ICMEs (figure 3.13) and the speed of the preceding ICME(paragraph 3.2.1.3)
* Triangular distributions of the peak proton intensity (I_p) against the speed of the driver CME (V_{CME})

and the peak SXR flux of the associated flare (I_{SXR}) that provide an upper limit, based on Lario et al.[60]. The upper-limit lines are constructed empirically via linear regression of the upper points of the log-log scatter plots. This process is repeated for all events regardless of classification, per class and MC-Pos/NoMC subcategories. (paragraph 3.2.2.1,paragraph 3.2.2.2)

The following three paragraphs summarize the main results drawn from all the above methods, answering how and in what degree the SEP intensities are affect by: (a) the various solar and IP parameters, without considering the specific classification (subsubsection 4.3.1), (b) the specific geometry between the associated ICME(s) and the observer (subsubsection 4.3.2), and lastly (c) the ICME magnetic structure (subsubsection 4.3.3).

4.3.1   Proton intensity regardless of the classification

The distributions of the peak proton intensity per energy channel, for all events regardless of the classification (figure 3.10), stem from normal distributions. They also have similar standard deviations ($\sim$1) and their means move to lower values as the energy interval shortens. Physically, protons reach lower intensities at narrower energy intervals, as expected.

The whisker plots of the aforementioned parameters reveal that the median peak proton intensity increases with the flare size and the CME speed (figure 3.16). Moreover, *the triangular distributions for all events* (figures 3.17, 3.20) *show that:*

- ○ Slow CMEs are not associated with large proton intensities, as the upper left space of the plots are empty. On the other hand, fast CMEs produce high energetic particles, thus the panels are more populated on the right. However, fast CMEs are also associated with lower intensities, as well, as the space on the bottom right of the panels is also populated (figure 3.17).
- ○ There isn't a significant increasing tendency of the peak proton intensity against CMEs faster than 2000km/s, as the corresponding values are far below the upper limit line (figure 3.17).
- ○ It is evident that the upper limit is less steep at narrower energy intervals, as we use integral proton intensities figure 3.17).
- ○ For a given CME, C flares are expected to produce lower proton intensities than M and X flares (figure 3.18).
- ○ For a given I_{SXR} value, the upper limits at different energy channels have approximately the same behavior (there is not a significant difference of the α values between the energy channels - figure 3.20).
- ○ The peak proton intensity shows a stronger variation with the speed of the driver CME, than with the peak SXR flux of the associated flare: The exponential index of V_{CME}-I_p (figure 3.17) is larger than the corresponding of I_{SXR}-I_p (figure 3.20).
- ○ Lario et al. [60] used differentiated energy channels and pfu/MeV flux units and found that the upper limit is steeper for higher energies. The difference between our results can be attributed to the different data format.
- ○ Finally, we conclude that SEPs are more energetic during periods that multiple ICMEs are found in the interplanetary space (figure 3.6): there is statistical relationship between the peak proton

intensity and the number of ICMEs (N_{ICME}) within a 3-days interval. Note that, the proton intensity for E>100MeV decreases for N_{ICME}>1. Moreover, the parameters of the associated solar activity also increase with the N_{ICME}: both the speed of the driver CME and the peak SXR flux are statistically higher with an increasing N_{ICME} number (figure 3.8 and figure 3.7 correspondingly). These results can be attributed to the fact that, at times of intense solar activity, all phenomena tend to be more extreme.

4.3.2   Proton intensity per class

The main conclusions concerning the proton intensity profiles of each class are:

▷ The most intense events are those classified in classes 3 and 4 (figure 3.9a). Specifically, class 3 events are statistically associated with the largest proton intensities. The second most extreme events are class 4, except E>100MeV, in which they reach the highest median($\log_{10} I_p$). Generally, the enhanced proton intensities can be explained as follows: First of all, particle mirroring between the ICME and the primary CME and the strong turbulence due to the passage of the preceding ICME can reflect particles back to the observer, leading to elevated intensities[60]. Second, particles pre-accelerated by the shock of the preceding ICME can serve as the seed population for the following shock of the primary CME[59]. Moreover, the confinement and reflection of particles between the looped field lines of an ICME rooted at the Sun, can lead to enhanced intensities within the ICME[67].

▷ Two class 4 events that were preceded by two ICMEs reach even higher intensities, up to 2 orders of magnitude (figure 3.13). Moreover, Class 4 events statistically reach higher intensities, when the preceding ICME is faster (figure 3.14). Both of these factors are statistically associated with more extreme solar conditions, that usually drive more intense SEP events. Moreover, both lead to more intense IP conditions, affecting the propagation and intensities of particles. Shocks ahead of faster ICMEs can also produce higher levels of turbulence and particles pre-accelerated by the fast shock of the preceding ICME can also lead to enhanced particle intensities[56]. Of course, there is a significant level of scattering, especially at higher energies, adding to the fact that there are also other significant factors.

▷ Furthermore, the construction of the triangular distributions per class (figure 3.19-table 3.3) shows that for a given CME speed, events occurring within the standard solar wind (class 0) are statistically associated with the lowest proton intensities, compared to classes 1,3 and 4. Note that, class 2 and 5 are excluded from this analysis. Class 3 events are associated with the largest exponential indices, suggesting that for a given CME speed they reach higher intensities compared to all other classes, followed by class 4 events.

▷ Almost the same is observed for the the peak proton intensity against the peak SXR flux of the associated flare (figures 3.21, 3.20). For a given flare, class 4 events tend to reach higher peak proton intensities, followed by class 3 events. Class 0 and class 1 have almost similar values.

▷ The peak proton intensity decreases for narrower energy intervals for a given CME speed, for class 0 and for 3 events (β decreases). It is worth noting that, classes 1 and 4 do not show this

decreasing tendency, rather have almost similar indices for all energy channels, neither increasing nor decreasing.

▷ The median (figure 3.9a) and mean (figure 3.11) intensities of Class 1 events are rather high. The standard deviation from the mean is significant, indicating that this IP configuration can have different effects, depending on the relative position of the observer. However, we observe that for a given CME speed, the proton intensity is lower than average. The attenuated intensities can be due to the fact that, the ICME structure between the Sun and the observer can act as a barrier to the particles.

▷ An ICME located between the Sun and the observer does not necessarily affect the particles [60]. Their interaction actually depends on various parameters, such as the relative longitudinal distance between the active region and the ICME origin at the Sun, their relative time gap, as well as the difference in width and speed between the ICME and the primary CME that drives the SEP event. Several studies, for example [29], [59],[56],[60], set various temporal and spatial criteria in order to estimate whether the ICME definitely interacts with the particles. On the other hand, there is certainty that, particles of class 4 events are affected in some degree by the passage of the ICME, due to its expansion and width extent at the time it is beyond Earth. For events in class 3, the particles reach the observer *with* the ICME, thus for a fact are affected by it.

▷ Class 2 events reach the lowest proton intensities at all energy channels (figure 3.11). Notably, there are no class 2 events that exhibit flux enhancement in the E>100MeV energy channel (figure 2.3). These results agree with Lario et al. [60], who also found lower intensities for their class 2 events. This can be attributed to the fact that, both the ICME ahead of the particle stream [58],[61] and the sheath region can act as barriers[68].

▷ Class 0 events reach statistically lower intensities as well, as they are generally associated with the least intense solar flares and slower CMEs.

▷ Class 5 events are intrinsically the most complex ones. The effect of one preceding and one following ICME (or more) can have multiple effects. They do exhibit large intensities, as the number of ICMEs is statistically associated with higher intensities, as explained above (see also figure 3.6). However, this behavior is not observed at all energy channels, as the intensity significantly decreases at the >60MeV and >100MeV channels. The enhanced particle intensities can be also explained as follows: the magnetic connectivity between the following and the preceding ICME can trap particles and reflect them back to the observer. However, the following ICME can also play a role in attenuating the particles. Moreover, the overall mechanism of the interaction between the ICMEs can have multiple effects.

4.3.3   The effect of magnetic clouds on proton intensities

The distinction of class 3 events reveals that:

▷ Theirs distributions of the peak proton intensities have similar means (figure 3.12). However Pos/NoMC events has a larger deviation from he mean, indicating that these events statistically can reach higher and lower proton intensities. The high level of scatter adds to the fact that, the Pos/NoMC category is not homogeneous: The configuration of an ICME without an MC structure can be more complex (see paragraph 1.2.4.3) and have multiple effect.

▷ The different behavior between the upper limits and distributions of the two subcategories suggest that for a given CME, class 3 events occurring within ICMEs without an MC structures are more likely to reach higher proton intensities than those occurring within ICMEs with MC structures. This result can be attributed to the converging magnetic structure of the MC, as it can act as a barrier for the particles and only a small fraction of particles can propagate through it, leading to relatively lower intensities within the cloud[61].

4.4   Spectral Profiles

The conclusions drawn from the spectral analysis of the SEP events are:

◇ The most frequent value of the spectral index for all events is 1.5, regardless of the classification (figure 3.23).

◇ Class 0 events also peak at 1.5 and are generally associated with softer spectra, as they are generally associated with lower energies (figure 3.24a).

◇ Both class 3 and 4 events have mostly harder spectra, as the are associated with higher energy particles and intensities. There isn't a different behavior between MC and Pos/NoMC subcategories (figure 3.24b).

◇ Class 2 events are mostly at the soft spectra region while class 5 to the hard (figure 3.24a). However, the small sample size does not allow firm conclusions.

◇ More intense flares are associated with harder spectra (figure 3.25), indicating that extreme solar conditions drive particles of even higher energies. However, there is a large degree of scatter, due to the fact that the spectra are *not* calculated at the Sun. Particles are subject to several processes that affect their intensities and energies, as discussed above (scattering, interaction with transient structures etc) and inevitably alter their spectral profiles.

◇ It is important to emphasize that, the difference amongst the spectral indices of the classes confirm the significant effect of ICMEs on particle intensities.

5   CONCLUSION

A database of 98 western SEP events, each one associated with a solar flare and/or a CME, is compiled, based on the *Advanced Solar Particle Event Casting System* database (ASPECS), which was developed on the methodology as outlined in [63].

The SEP events are classified according to the location of one or more ICMEs at the time of the peak proton intensity, based on in situ measurements and adopted by Lario et al. [60]. Note that most of the events are classified to the same categories in this study and by [60].

Class 0 events are those events that are not associated with ICMEs within a 3-day interval before or after the maximum proton intensity and we assume that particles propagate within the standard solar wind. *Class 1* events occur before an ICME passes Earth and *class 2* occur in the sheath region of an ICME. *Class 3* events are observed when Earth is immersed within an ICME and *class 4* are preceded by one or more ICMEs. *Class 5* events occur between a following and a preceding ICME. ICMEs that are counterparts of the CME that drives the event (driver CME), are excluded from the classification scheme. Note that most events are classified to the same categories in this study as by Lario et al. [60]. A similar study was performed by Miteva et al.[16], who considered SEP events associated with M and X flares and classified them into two distinct classes: standard solar wind or interplanetary coronal mass ejections (ICMEs). The first class coincides with class 0 and the latter with class 3.

A secondary classification to class 3 events is also performed: events that occur within ICMEs that have a definite MC structure, are labeled as *MC*. Class 3 events within ICMEs that have some MC characteristics or non at all, are labeled as *Pos/NoMC*.

The absence of presence of ICMEs in the IP space, as well as of the MC characteristics, are acquired from the ICME list compiled by Richardson and Cane (R-C) (http://www.srl.caltech.edu/ACE/ASC/DATA/level3/icmetable2.html#(l)).

- We find that $\sim 74\%$ of all SEPs are generally associated with one or more ICMEs, regardless of the specific topology. The most common amongst the classes are those events that occur within an ICME (class 3, $\sim 31\%$), followed by the events occurring within the standard solar wind (class 0, $\sim 26\%$) and the ones preceded by one or more ICMEs (class 4, $\sim 17\%$). These results are in agreement with several similar studies [16],[66].

- Generally, the most extreme SEP events are most likely to originate at intense flares and fast CMEs. The speed of the driver CME and SXR magnitude of the associated flare are correlated to each other, meaning that fast CMEs are statistically related to intense flares and vice versa.

- Furthermore, intense SEP events tend to occur during periods that multiple ICMEs are present in the IP space, regardless of their relative position to the observer.

- We define upper limits of the peak proton intensity for given solar conditions, in order to assess the effect of ICMEs. Generally, particles can not easily propagate through ICMEs, thus the location of the latter in the IP space dominates the intensities of SEPs. The classification reveals that, SEP

events that occur in vicinity of an ICME (class 3) statistically reach the highest intensities. Events that occur when one or more ICMEs are beyond Earth at the time of the peak proton intensity, are the second most intense (class 4). For both of the above classes, the enhanced intensities can be attributed to the fact that, both the magnetic topology between the preceding ICME and the primary CME, as well as the turbulence due to the passage of the preceding ICME, can reflect particles back towards the observer. Moreover, particles confined within the ICME and reflected between the looped field lines rooted at the Sun, can lead to enhanced intensities within the ICME.

- We also observe that there is a positive correlation between the peak proton intensity and the speed of a preceding ICME located beyond Earth (class 4), despite a certain degree of scattering of the data points. Moreover, two class 4 events that occur when *two* ICMEs are beyond Earth, reach higher proton intensities by two orders of magnitude at all energy channels. This can be attributed to the fact that, both the speed and the number of preceding ICMEs are associated with more extreme solar conditions, but also introduce more intense IP conditions, affecting the transport and intensities of particles.

- On the other hand, an ICME located between the Sun and the observer leads to lower intensities, as the ICME potentially acts as an intervening structure for the particles, altering their propagation. Actually, the lowest intensities amongst all classes are observed for events that occur within the sheath region of an ICME. Those events are also the least energetic, as they do not exhibit flux enhancements of particles for energies above 100MeV.

- The present of multiple ICMEs located beyond and after the observer (class 5) can have various effects, depending on several parameters, for example the relative position and time gap among the active region and the ICMEs, the interaction among the ICMEs and primary CME. Generally, further study of the interaction between the primary CME and the ICME(s) in any position relative to the observer could contribute to our understanding of the particle intensity profiles and acceleration, especially for those cases where the CMEs spatially overlap (see paragraph 1.2.4.4).

- A noteworthy result is that, for given solar conditions, events that occur within ICMEs without MC structures are more likely to reach higher proton intensities, compared to those within ICMEs with MC structures, although the mean proton intensities of the two subcategories are almost equal. This result can be explained as follows: the converging magnetic structure of the MC can act as a barrier ahead of the particles, leading to relatively lower intensities within the cloud[61]. Note that, ICMEs without MC structures can have more complex configurations. A further examination of the effect of MCs in other IMF configurations would benefit the study of the SEP profiles.

- Lastly, the spectral profiles of the SEP events are not uniform, indicating that the IP conditions affect the intensity and transport of particles. Events associated with ICMEs generally have harder spectra values. The similar peak values of the spectral distributions suggest however that there isn't a different acceleration mechanism amongst the classes.

A major limitation of this study, and other similar studies as well, is that observations are limited primarily to in-situ measurements, which in turn usually suffer from multiple types or errors: spikes, measurement errors, gaps etc[69]. Consequently, the exact IP conditions within which the particles propagate cannot be fully known. Notably, the absence of ICMEs does not necessarily mean that particles propagate within the standard solar wind, as other types of IP shocks, for example CIRs, can affect them. Moreover, the vast variety of factors and physical processes that affect the propagation of particles from the Sun to the observer in contrast to the small sample at hand limit this study to a statistical approach. The longitudinal restrictions set in order to ensure magnetic connectivity between the active region and the observer, as well as the division of events to classes, limit the sample size studied. The understanding of these limitations is crucial for a better physical interpretation of the results.

6 APPENDIX

A Bootstrap

The *bootstrap* method is a procedure used for determining the uncertainty of an estimated parameter[70]. A specific function (i.e. mean, regression etc) is applied n-times at N repeated samples drawn at random out of the N-size dataset. The n-size bootstrap array approximates a normal distribution and the function value is taken as the mean value of the array. The confidence interval is specified as $\pm error$ for each linear model, where the $error = z^{(a)} \cdot \sigma$, where σ the standard deviation of the bootstrap array and $z^{(a)}$ is the 100 - α percentile point of a standard normal variate [64]. Provided that the original data sample is independent, the distribution of these recalculated parameters maps the uncertainty in the estimate from the original sample [70].

B Hypothesis Testing

Classical hypothesis testing is based on the following steps:

1. Set up two possible and opposite scenarios: The *null hypothesis H_0*, which should be ultimately rejected and the *alternative hypothesis H_1*.
2. A *significance level α* is specified a priori.
3. H_0 is rejected if p-value<α. The p-value is called the probability that H_0 is rejected, while H_0 is valid (also called error type I). If p-value>a, then H_0 can't be rejected.

B.1 Student T-test

Student's T-test is a statistical method, which tests whether a correlation of a N-size sample is significant ([71]). The hypotheses are:

- H_0: the correlation is not significant for a given significance level α, meaning that the correlation coefficient r=0
- H_1: the correlation is not significant for a given significance level α, meaning that the correlation coefficient r$\neq$0.

The test statistic is:

$$t^* = \frac{r\sqrt{N-2}}{\sqrt{1-r^2}}$$

The hypothesis H_0 is rejected when p-value<α. The P-value is determined by referring to a t-distribution with N-2 degrees of freedom.

B.2 Kolmogorov-Smirnov Test

The Kolmogorov–Smirnov test is a non-parametric goodness-of-fit test , used to determine whether a distribution differs from a hypothesized distribution (one-sample) or whether two distributions are significantly different (two-sample) [72]. An important advantage of the K-S test against other goodness-of-fit tests, for example the chi-square, is that it is independent of the binning and also non-parametric, thus powerful even for small samples [73].

The one sample, two-sided test statistic is the maximum absolute difference $\mathcal{D}$ between the empirical cumulative distribution function (cdf) and the hypothesized cdf: $\mathcal{D} = |\hat{\mathcal{F}} - \mathcal{G}|$, where $\mathcal{F}$ is the empirical cdf and $\mathcal{G}$ is the the cdf of the hypothesized distribution [13].

Two two-sample test evaluates the difference between the cdfs $\mathcal{F}_{1,2}$ of two sample data vectors. The two-sided K-S test, used here, calculates the absolute difference: $\mathcal{D} = |\mathcal{F}_1 - \mathcal{F}_2|$ between the two cdfs and compares it with a critical value [73].

For both the one-/two-sample tests, the null hypothesis H_0 is rejected at a level of significance α, if D exceeds a critical value specified by statistical tables [73].

C   Whisker plots/Boxplots

A box-plot or whiskers plot is a method for graphically depicting groups of numerical data. The central mark indicates the median, and the bottom and top edges of the box indicate the 25th and 75th percentiles, respectively. The whiskers extend to the most extreme data points not considered outliers, and the outliers are plotted individually using the '+' symbol in red. An outlier is a value 1.5 times their interquartile range [14].

---

[13]https://www.mathworks.com/help/stats/kstest.html
[14]https://www.mathworks.com/help/stats/boxplot.html

LIST OF ABBREVIATIONS

ACE Advanced Composition Explorer

AR activer region

ASPECS Advanced Solar Particle Event Casting System

AU Astronomical Unit

BFS Big Flare Syndrome

CI Confidence Interval

CIR Cororating Interaction Regions

CME Coronal Mass Ejection

CNO Carbon-Dioxide-Oxygen

FIP First Ionization Potential

GCR Galactic Cosmic Rays

GLE Ground Level Event

ICME Interplanetary Coronal Mass Ejection

IMF Interplanetary Magnetic Field

LASCO Large Angle and Spectrometric Coronagraph

MC Magetic Cloud

MHD Magneto-Hydrodynamic

p-p proton-proton

pfu particle flux unit

Pos/NoMC Possible or No Magnetic Cloud

s/c spacecraft

SEP Solar Energetic Particles

SOHO Solar & Heliospheric Observatory

SPR Solar Proton Release

SXR Soft X-Ray

UT Universal Time

LIST OF FIGURES

LIST OF TABLES

REFERENCES

[1]   Donald V Reames. *Solar energetic particles*. Springer, 2017.

[2]   R. A. Mewaldt et al. "Radiation risks from large solar energetic particle events". In: *AIP Conference Proceedings* 932.1 (2007), pp. 277–282. DOI: 10.1063/1.2778975. eprint: https://aip.scitation.org/doi/pdf/10.1063/1.2778975. URL: https://aip.scitation.org/doi/abs/10.1063/1.2778975.

[3]   Leonty Miroshnichenko. "Spectrum of Solar Cosmic Rays Near the Earth". In: *Solar Cosmic Rays: Fundamentals and Applications*. Cham: Springer International Publishing, 2015, pp. 299–332. ISBN: 978-3-319-09429-8. DOI: 10.1007/978-3-319-09429-8_9. URL: https://doi.org/10.1007/978-3-319-09429-8_9.

[4]   Eric Priest. *Magnetohydrodynamics of the Sun*. Cambridge University Press, 2014.

[5]   SW Kahler. "The role of the big flare syndrome in correlations of solar energetic proton fluxes and associated microwave burst parameters". In: *Journal of Geophysical Research: Space Physics* 87.A5 (1982), pp. 3439–3448.

[6]   H Koskinen and R Vainio. "Lectures on Solar Physics: From the core to the heliopause". In: *Universidade de Helsinki–Finlândia* (2009).

[7]   Arvind Bhatnagar and William Charles Livingston. *Fundamentals of solar astronomy*. Vol. 6. World Scientific, 2005.

[8]   Peter V Foukal. *Solar astrophysics*. John Wiley & Sons, 2008.

[9]   Adam J Finley et al. "Solar Angular Momentum Loss Over the Past Several Millennia". In: *The Astrophysical Journal* 883.1 (2019), p. 67.

[10] LA Fisk and MA Lee. "Shock acceleration of energetic particles in corotating interaction regions in the solar wind". In: *The Astrophysical Journal* 237 (1980), pp. 620–626.

[11] Ian G Richardson. "Energetic particles and corotating interaction regions in the solar wind". In: *Space Science Reviews* 111.3-4 (2004), pp. 267–376.

[12] Joe Giacalone, J Randy Jokipii, and J Kóta. "Particle acceleration in solar wind compression regions". In: *The Astrophysical Journal* 573.2 (2002), p. 845.

[13] HW Babcock. "The Topology of the Sun's Magnetic Field and the 22-YEAR Cycle." In: *The Astrophysical Journal* 133 (1961), p. 572.

[14] Martin Asplund et al. "The chemical composition of the Sun". In: *Annual Review of Astronomy and Astrophysics* 47 (2009), pp. 481–522.

[15] Donald V Reames. "Abundances, ionization states, temperatures, and FIP in solar energetic particles". In: *Space Science Reviews* 214.3 (2018), p. 61.

[16] R Miteva et al. "Solar energetic particle events in the 23rd solar cycle: interplanetary magnetic field configuration and statistical relationship with flares and CMEs". In: *Solar Physics* 282.2 (2013), pp. 579–613.

[17] RD Cunha-Silva, FCR Fernandes, and CL Selhorst. "Solar type II radio bursts associated with CME expansions as shown by EUV waves". In: *Astronomy & Astrophysics* 578 (2015), A38.

[18] Noé Lugaz et al. "The interaction of successive coronal mass ejections: a review". In: *Solar Physics* 292.4 (2017), p. 64.

[19] RF Wimmer-Schweingruber et al. "Understanding interplanetary coronal mass ejection signatures". In: *Coronal Mass Ejections*. Springer, 2006, pp. 177–216.

[20] Timothty Howard. *Coronal mass ejections: An introduction*. Vol. 376. Springer Science & Business Media, 2011.

[21] BC Low. "Coronal mass ejections, magnetic flux ropes, and solar magnetism". In: *Journal of Geophysical Research: Space Physics* 106.A11 (2001), pp. 25141–25163.

[22] Ian G Richardson and Hilary V Cane. "Near-Earth interplanetary coronal mass ejections during solar cycle 23 (1996–2009): Catalog and summary of properties". In: *Solar Physics* 264.1 (2010), pp. 189–237.

[23] Thomas H Zurbuchen and Ian G Richardson. "In-situ solar wind and magnetic field signatures of interplanetary coronal mass ejections". In: *Coronal mass ejections*. Springer, 2006, pp. 31–43.

[24] HA Elliott et al. "An improved expected temperature formula for identifying interplanetary coronal mass ejections". In: *Journal of Geophysical Research: Space Physics* 110.A4 (2005).

[25] RJ Forsyth et al. "ICMEs in the inner heliosphere: Origin, evolution and propagation effects". In: *Space science reviews* 123.1-3 (2006), pp. 383–416.

[26] L Burlaga et al. "Magnetic loop behind an interplanetary shock: Voyager, Helios, and IMP 8 observations". In: *Journal of Geophysical Research: Space Physics* 86.A8 (1981), pp. 6673–6684.

[27] AJ Prise et al. "Analysis of a coronal mass ejection and corotating interaction region as they travel from the Sun passing Venus, Earth, Mars, and Saturn". In: *Journal of Geophysical Research: Space Physics* 120.3 (2015), pp. 1566–1588.

[28] Ying D Liu et al. "Interactions between coronal mass ejections viewed in coordinated imaging and in situ observations". In: *The Astrophysical Journal Letters* 746.2 (2012), p. L15.

[29] SW Kahler and A Vourlidas. "Do interacting coronal mass ejections play a role in solar energetic particle events?" In: *The Astrophysical Journal* 784.1 (2014), p. 47.

[30] N Gopalswamy et al. "Radio signatures of coronal mass ejection interaction: Coronal mass ejection cannibalism?" In: *The Astrophysical Journal Letters* 548.1 (2001), p. L91.

[31] RA Mewaldt et al. "Energy spectra, composition, and other properties of ground-level events during solar cycle 23". In: *Space Science Reviews* 171.1-4 (2012), pp. 97–120.

[32] B Klecker et al. "Energetic particle observations". In: *Space science reviews* 123.1-3 (2006), pp. 217–250.

[33] Karl-Ludwig Klein and Silvia Dalla. "Acceleration and propagation of solar energetic particles". In: *Space Science Reviews* 212.3-4 (2017), pp. 1107–1136.

[34] HV Cane and D Lario. "An introduction to CMEs and energetic particles". In: *Space science reviews* 123.1-3 (2006), pp. 45–56.

[35] Loukas Vlahos et al. "Sources of solar energetic particles". In: *Philosophical Transactions of the Royal Society A* 377.2148 (2019), p. 20180095.

[36] Hong Xie et al. "Energy dependence of SEP electron and proton onset times". In: *Journal of Geophysical Research: Space Physics* 121.7 (2016), pp. 6168–6183.

[37] M Temerin and I Roth. "The production of He-3 and heavy ion enrichment in He-3-rich flares by electromagnetic hydrogen cyclotron waves". In: *The Astrophysical Journal* 391 (1992), pp. L105–L108.

[38] Nat Gopalswamy. "Factors affecting the intensity of solar energetic particle events". In: *AIP Conference Proceedings*. Vol. 1436. 1. American Institute of Physics. 2012, pp. 247–252.

[39] G Trottet et al. "Statistical evidence for contributions of flares and coronal mass ejections to major solar energetic particle events". In: *Solar Physics* 290.3 (2015), pp. 819–839.

[40] R Gómez-Herrero et al. "Circumsolar energetic particle distribution on 2011 November 3". In: *The Astrophysical Journal* 799.1 (2015), p. 55.

[41] ME Wiedenbeck et al. "Observations of solar energetic particles from 3He-rich events over a wide range of heliographic longitude". In: *The Astrophysical Journal* 762.1 (2012), p. 54.

[42] Jan Kuijpers. "Particle acceleration". In: *Plasma Astrophysics*. Springer, 1996, pp. 101–162.

[43] John G. Kirk. "Particle Acceleration". In: *Plasma Astrophysics*. Ed. by A. O. Benz and T. J.-L. Courvoisier. Berlin, Heidelberg: Springer Berlin Heidelberg, 1994, pp. 225–314. ISBN: 978-3-540-31627-5. DOI: 10.1007/3-540-31627-2_3. URL: https://doi.org/10.1007/3-540-31627-2_3.

[44] Malcolm S. Longair. "The acceleration of high energy particles". In: *High Energy Astrophysics*. 3rd ed. Cambridge University Press, 2011, pp. 561–582. DOI: 10.1017/CBO9780511778346.019.

[45] Enrico Fermi. "On the origin of the cosmic radiation". In: *Physical review* 75.8 (1949), p. 1169.

[46] Pasquale Blasi. "The origin of galactic cosmic rays". In: *The Astronomy and Astrophysics Review* 21 (2013), pp. 1–73.

[47] Malcolm S. Longair. "Aspects of plasma physics and magnetohydrodynamics". In: *High Energy Astrophysics*. 3rd ed. Cambridge University Press, 2011, pp. 298–330. DOI: 10.1017/CBO9780511778346.013.

[48] A Warmuth, G Mann, and H Aurass. "Modelling shock drift acceleration of electrons at the reconnection outflow termination shock in solar flares-Observational constraints and parametric study". In: *Astronomy & Astrophysics* 494.2 (2009), pp. 677–691.

[49] Leontii Ivanovich Miroshnichenko. "Solar cosmic rays: 75 years of research". In: *Physics-Uspekhi* 61.4 (2018), p. 323.

[50] Donals C Ellison and Reuven Ramaty. "Shock acceleration of electrons and ions in solar flares". In: *The Astrophysical Journal* 298 (1985), pp. 400–408.

[51]   A. Bruno et al. "Solar Energetic Particle Events Observed by the PAMELA Mission". In: *The Astrophysical Journal* 862.2 (July 2018), p. 97. DOI: 10.3847/1538-4357/aacc26. URL: https://doi.org/10.3847%2F1538-4357%2Faacc26.

[52]   D Band et al. "BATSE observations of gamma-ray burst spectra. I-Spectral diversity". In: *The Astrophysical Journal* 413 (1993), pp. 281–292.

[53]   Alessandro Bruno et al. "Spectral analysis of the september 2017 solar energetic particle events". In: *Space Weather* 17.3 (2019), pp. 419–437.

[54]   R. Ramaty. "Energetic particles in solar flares". In: *AIP Conference Proceedings* 56.1 (1979), pp. 135–154. DOI: 10.1063/1.32074. eprint: https://aip.scitation.org/doi/pdf/10.1063/1.32074. URL: https://aip.scitation.org/doi/abs/10.1063/1.32074.

[55]   L. Vlahos et al. "Particle Acceleration". In: *Energetic Phenomena on the Sun*. Ed. by M. R. Kundu, B. Woodgate, and E. J. Schmahl. Dordrecht: Springer Netherlands, 1989, pp. 127–224. ISBN: 978-94-009-2331-7. DOI: 10.1007/978-94-009-2331-7_2. URL: https://doi.org/10.1007/978-94-009-2331-7_2.

[56]   N Gopalswamy et al. "Intensity variation of large solar energetic particle events associated with coronal mass ejections". In: *Journal of Geophysical Research: Space Physics* 109.A12 (2004).

[57]   Stephen Kahler, Joan Burkepile, and Donald Reames. "Coronal/interplanetary factors contributing to the intensities of E> 20 MeV gradual solar energetic particle events". In: *International Cosmic Ray Conference*. Vol. 6. 1999, p. 248.

[58]   D Lario, RB Decker, and A Aran. "Solar energetic particle intensities above the streaming limit". In: *AIP Conference Proceedings*. Vol. 1039. 1. American Institute of Physics. 2008, pp. 156–161.

[59]   G Li et al. "A twin-CME scenario for ground level enhancement events". In: *Space Science Reviews* 171.1-4 (2012), pp. 141–160.

[60]   D Lario and A Karelitz. "Influence of interplanetary coronal mass ejections on the peak intensity of solar energetic particle events". In: *Journal of Geophysical Research: Space Physics* 119.6 (2014), pp. 4185–4209.

[61]   May-Britt Kallenrode. "Magnetic clouds and interplanetary particle transport: a numerical model". In: *Journal of atmospheric and solar-terrestrial physics* 64.18 (2002), pp. 1973–1978.

[62]   M Vandas et al. "Magnetic traps in the interplanetary medium associated with magnetic clouds". In: *Journal of Geophysical Research: Space Physics* 101.A10 (1996), pp. 21589–21596.

[63]   Athanasios Papaioannou et al. "Solar flares, coronal mass ejections and solar energetic particle event characteristics". In: *Journal of Space Weather and Space Climate* 6 (2016), A42.

[64]   Bradley Efron. "Better bootstrap confidence intervals". In: *Journal of the American statistical Association* 82.397 (1987), pp. 171–185.

[65]   Rebekah M Evans et al. "The SCORE scale: A coronal mass ejection typification system based on speed". In: *Space Weather* 11.6 (2013), pp. 333–334.

[66] S Masson et al. "The interplanetary magnetic structure that guides solar relativistic particles". In: *Astronomy & Astrophysics* 538 (2012), A32.

[67] IG Richardson, G Wibberenz, and HV Cane. "The relationship between recurring cosmic ray depressions and corotating solar wind streams at$\leq$ 1 AU: IMP 8 and Helios 1 and 2 anticoincidence guard rate observations". In: *Journal of Geophysical Research: Space Physics* 101.A6 (1996), pp. 13483–13496.

[68] S-S Wu and G Qin. "Magnetic Cloud and Sheath in the Ground-Level Enhancement Event of 2000 July 14. I. Effects on the Solar Energetic Particles". In: *arXiv preprint arXiv:2008.06427* (2020).

[69] R Miteva, SW Samwel, and MV Costa-Duarte. "Solar energetic particle catalogs: assumptions, uncertainties and validity of reports". In: *Journal of Atmospheric and Solar-Terrestrial Physics* 180 (2018), pp. 26–34.

[70] J. V. Wall and C. R. Jenkins. "Data modelling; parameter estimation". In: *Practical Statistics for Astronomers*. Cambridge Observing Handbooks for Research Astronomers. Cambridge University Press, 2003, pp. 105–141. DOI: 10.1017/CBO9780511536618.008.

[71] J. V. Wall and C. R. Jenkins. "Correlation and association". In: *Practical Statistics for Astronomers*. Cambridge Observing Handbooks for Research Astronomers. Cambridge University Press, 2003, pp. 54–75. DOI: 10.1017/CBO9780511536618.006.

[72] "Kolmogorov–Smirnov Test". In: *The Concise Encyclopedia of Statistics*. New York, NY: Springer New York, 2008, pp. 283–287. ISBN: 978-0-387-32833-1. DOI: 10.1007/978-0-387-32833-1_214. URL: https://doi.org/10.1007/978-0-387-32833-1_214.

[73] J. V. Wall and C. R. Jenkins. "Hypothesis testing". In: *Practical Statistics for Astronomers*. Cambridge Observing Handbooks for Research Astronomers. Cambridge University Press, 2003, pp. 76–104. DOI: 10.1017/CBO9780511536618.007.